UNIVERSITY OF CALIFORNIA
Santa Barbara

Coarse-Grained Molecular Dynamics Simulations of Peptide Aggregation on Surfaces

A dissertation submitted in partial satisfaction
of the requirements for the degree
Doctor of Philosophy
in
Physics

by

Herbert Alexander Morriss-Andrews

Committee in charge:

Professor Joan-Emma Shea, Chair

Professor Everett Lipman

Professor Philip Pincus

September 2014

The Dissertation of Herbert Alexander Morriss-Andrews is approved.

Professor Everett Lipman

Professor Philip Pincus

Professor Joan-Emma Shea, Committee Chair

July 2014

Coarse-Grained Molecular Dynamics Simulations

of Peptide Aggregation on Surfaces

Herbert Alexander Morriss-Andrews

Acknowledgments

Foremost, I would like to thank my advisor, Joan-Emma Shea, whose guidance was essential to the development of this work at every step of the way. I would also like to thank Frank Brown for his considerable help in the success of the membrane project in Chapter 6, particularly in the ironing out of many details and subtleties. Finally, the assistence of Max Watson, Andrew Jewett, and Giovanni Bellesia in getting started with the various projects of this work is greatly appreciated. I acknowledge funding from an NSERC postdoctoral fellowship (PGS-D), the Los Alamos National Laboratory, and the University of California Santa Barbara. Computational resources for simulations were provided by the UC Thresher computer pilot project, the Extreme Science and Engineering Discovery Environment (XSEDE), and the University of California Santa Barbara Center for Scientific Computing.

Curriculum Vitae

Herbert Alexander Morriss-Andrews

Education

Ph.D. in Physics, University of California at Santa Barbara, 2014 (expected)

M.Sc. in Physics, University of British Columbia, Vancouver, Canada, 2009

B.Sc. in Mathematical Physics, Queen's University, Kingston, Canada, 2007

Field of Study

Computational biophysics, biomolecular simulation, and protein aggregation with Joan-Emma Shea

Selected Publications

Morriss-Andrews, A. and Shea, J.-E. "Simulations of Protein Aggregation: Insights from Atomistic and Coarse-Grained Models", J. Phys. Chem. Lett. **5** (11), pp 1899–1908 (2014)

Morriss-Andrews, A., Brown, F.L.H. and Shea, J.-E. "A Coarse-Grained Model for Peptide Aggregation on a Membrane Surface", J. Phys. Chem. B. In press (2014)

Watson, M.C., **Morriss-Andrews, A.** and Brown, F.L.H. "Thermal fluctuations in shape, thickness, and molecular orientation in lipid bilayers. II. Finite surface tensions", BioChem. Phys. **139**, 084706 (2013)

Morriss-Andrews, A., Bellesia, G. and Shea, J.-E. "β-sheet propensity controls the kinetic pathways and morphologies of seeded peptide aggregation", J. Chem. Phys. **137**, 145104 (2012)

Morriss-Andrews, A. and Shea, J.-E. "Kinetic pathways to peptide aggregation on surfaces: the effects of β-sheet propensity and surface attraction", J. Chem. Phys. **136**, 065103 (2012)

Morriss-Andrews, A., Bellesia, G. and Shea, J.-E. "Effects of surface interactions on peptide aggregate morphology", J. Chem. Phys. **135**, 085102 (2011)

Morriss-Andrews, A., Rottler, J. and Plotkin, S.S. "A systematically coarse-grained model for DNA, and its predictions for persistence length, stacking, twist, and chirality", J. Chem. Phys. **132**, 035105 (2010)

Abstract

Coarse-Grained Molecular Dynamics Simulations

of Peptide Aggregation on Surfaces

by

Herbert Alexander Morriss-Andrews

Protein aggregation involves self-assembly of normally soluble proteins or peptides into supramolecular structures. This process is particularly important due to its involvement in several amyloid diseases, such as Parkinson's, Alzheimer's, and Type II diabetes. Several fibrillization mechanisms have been proposed, including a condensation-ordering mechanism where ordered fibril structures emerge from disordered oligomers and a dock-lock mechanism where a growing fibril induces attached polypeptides to organize individually into fibril-compatible conformations.

We present a series of computational studies using a coarse-grained peptide aggregate model that exhibits a rich diversity of structures: amorphous/disordered aggregates, beta-barrels, multi-layered fibrils, and aggregates of mixed type. Our model has a tunable backbone stiffness that governs the propensity to form fibrils in bulk solution. In this work, we investigate how this β-sheet propensity couples with the properties of a surface template to influence the mechanism of aggregation. Here, we focus on peptide aggregation in the presence of three templates: a solid surface, the surface of a pre-existing aggregate seed, and a lipid bilayer.

Aggregation on solid hydrophilic or hydrophobic surfaces frequently occurs in many experimental setups. We find that the solid surface strongly biases toward the formation of fibrillar aggregates. Peptide-peptide interactions and surface attraction couple cooperatively on a solid surface to influence the bind-

ing/aggregation transition. Aggregation and binding occur almost simultaneously since the surface's crystal symmetry enforces a preferred direction of bound fibril growth, thus accelerating the process.

Seeding peptides with compatible aggregates removes the nucleation barrier for aggregation. We find that the aggregation mechanism is strongly dependent on the β-sheet propensity of both the seed and bulk peptides. Additionally, bulk peptides that exhibit polymorphism can have multiple pathways to aggregation depending on which class of aggregate they initially form. We find that a fibrillar seed can induce amorphous-prone peptides into fibrillar structures via a condensation-ordering mechanism, thus sequestering potentially cytotoxic oligomers into a more inert form.

We simulate aggregation on lipid bilayers in an effort to approximate the complexity of the cellular milieu. While aggregation in vivo would occur in the presence of membrane surfaces, few simulation studies have been conducted on this combined system due to its computational complexity. We have determined that a membrane surface, like a crystal surface, biases toward fibrillar aggregates. However, membrane undulations disturb multi-layered fibrils into non-planar β-sheet structures, such as β-barrels. The presence of fibrils on the membrane also affects its fluid properties, creating a hexagonally packed lipid ordering underneath the fibrils, locally increasing its bending modulus and aligning lipid tilt to the orientation of the peptides. Thus peptide aggregation and membrane fluidity affect each other's structure and dynamics.

The key general features of a surface that control its modulation of peptide aggregation are its structural order and fluidity. An ordered, rigid template biases more strongly toward fibrillar structures and restricts the set of aggregation pathways and morphologies. The dynamic nature of a fluid surface biases less toward

fibrils and enhances the range of aggregation dynamics.

Contents

1 Introduction **1**

1.1 Coarse-Graining 1

1.2 Proteins 4

1.3 Our Peptide Model 9

1.4 Atomistic Simulations of Monomers, Small Oligomers, and Mature Fibrils 12

1.4.1 Coarse-Grained Models of Protein Aggregation 17

1.4.2 Aggregation in the Cellular Milieu 23

1.5 Concluding Thoughts 25

2 Methods **27**

2.1 Peptide Model 27

2.1.1 Model Geometry 27

2.1.2 Potentials 28

2.1.3 Nonbonded Interactions 30

2.1.4 Peptide-Surface Interactions 30

2.2 Lipid Model 33

2.3 Langevin Dynamics Implicit Solvent Model 35

2.4 Replica Exchange Molecular Dynamics 37

3 Thermodynamics of Peptide Aggregation on a Solid Surface 40

3.1 Methods . . . 43

3.1.1 Order Parameters . . . 44

3.2 Results . . . 47

3.2.1 Peptides adopt different aggregate structures in the bulk than on surfaces . . . 47

3.2.2 Binding transition sharpened by surface attraction and chiral stiffness . . . 50

3.2.3 Isolating Interactions Highlights Aggregation/Binding Cooperativity . . . 55

3.3 Summary and Discussion . . . 60

4 Kinetics of Peptide Aggregation on a Solid Surface 63

4.1 Methods . . . 64

4.1.1 Order Parameters . . . 64

4.1.2 Simulations . . . 65

4.2 Results . . . 67

4.2.1 Formation of a Single Layer . . . 67

4.2.2 Other Aggregate Structures . . . 77

4.2.3 Order Parameter Equilibration Rates Indicate Cooperativity 79

4.2.4 Diffusion . . . 82

4.3 Summary and Discussion . . . 83

5 Seeded Peptide Aggregation 87

5.1 Methods . . . 90

5.1.1 Simulations . . . 90

5.1.2 Order Parameters . . . 90

5.2 Results 91
5.2.1 Case 1: Homogeneous Seeding and Aggregation: Fibril Seed ($K_\chi = 2$ kcal/mol) and Free Peptides of High β-Sheet Propensity ($K_\chi = 2$ kcal/mol) 92
5.2.2 Case 2: Heterogeneous Seeding and Aggregation: Fibril Seed ($K_\chi = 2$ kcal/mol) with Flexible Peptides ($K_\chi = 1$ kcal/mol) 93
5.2.3 Case 3: Heterogeneous Seeding and Aggregation: Fibril Seed ($K_\chi = 2$ kcal/mol and Free Peptides with Intermediate β-Sheet Propensity ($K_\chi = 1.5$ kcal/mol) 94
5.2.4 Case 4: Heterogeneous Seeding and Aggregation: Amorphous Seed ($K_\chi = 1$ kcal/mol) with Rigid Peptides ($K_\chi = 2$ kcal/mol) 95
5.2.5 Mixing Order Parameter Differentiates Aggregation Mechanism 96
5.3 Summary and Discussion 100
5.4 Pathway Diagrams 105

6 Kinetics of Peptide Aggregation on a Membrane 114
6.1 Methods 118
6.1.1 Simulations 118
6.1.2 Order Parameters for Peptides and Membrane 119
6.2 Results 123
6.3 Aggregation on a Fluid Membrane Induces Different Structures than on a Solid Surfacee 123

6.4 Cooperativity of Peptide Binding and Aggregation Seen on Solid Surface Absent in the Presence of a Membrane 130
6.5 Peptide Aggregates Damp Thermal Membrane Fluctuations and Slightly Increase Membrane Bending Rigidity 133
6.6 Summary and Discussion 140

7 Conclusions **144**

A Hydrophobic Collapse of a Homopolymer **148**
A.1 Methods 149
A.1.1 Polymer Model 149
A.1.2 Explicit CG Water Model 150
A.1.3 Implicit Desolvation Potential 150
A.1.4 Implicit Lennard-Jones Potential 151
A.1.5 Simulations 152
A.2 Results 152
A.2.1 Neutral Polymers 153
A.2.2 Methane Polymers 154
A.3 Summary and Discussion 159

List of Figures

1.1 Hierarchy of coarse-grained models 2

1.2 Time scales of biomolecular processes 3

1.3 Protein aggregation diseases 5

1.4 Cross-β spine aggregates 7

1.5 Overview of atomistic and coarse-grained modeling of protein aggregation 8

1.6 Steric zipper aggregate in our peptide model 9

1.7 Phase diagram of bulk aggregate morphology 10

1.8 Differences in sequences of IAPP peptides between human and rat variants 12

1.9 The interaction of hIAPP with membranes 24

2.1 28

2.2 Peptide and surface model 31

2.3 34

3.1 Bulk aggregates 41

3.2 Equilibrium aggregate morphologies 42

3.3 Images of morphology designations 46

3.4 Rare aggregate structures on the surface 49

3.5 Peptide binding transition to surface 51
3.6 Binding transition temperatures 54
3.7 Unified binding transition temperatures 55
3.8 Free energy across binding transition 56
3.9 Binding transition of noninteracting peptides 57
3.10 Binding transition of Boltzmann-distributed particles on a Lennard-Jones surface 58

4.1 Structure distribution at transition temperature 67
4.2 Structure distribution below transition temperature 68
4.3 Formation of a single-layered fibril on a solid surface 69
4.4 Kinetic pathway distribution below the transition temperature . . 70
4.5 Peptide insertion into surface-bound fibril 72
4.6 Images of aggregation on a fibril-seeded solid surface 73
4.7 Mixing between bulk and seed peptides on a surface 74
4.8 Depictions of fibrillar assembly/disassembly on a solid surface . . 75
4.9 Frequencies of assembly/disassembly pathways 76
4.10 Pathway frequencies of fibrillar assembly/disassembly on a solid surface 78
4.11 Binding and aggregation kinetics on a solid surface 80
4.12 Translational diffusion of a fibril on a solid surface 81
4.13 Rotational locking of a fibril on a solid surface 82

5.1 Seeded aggregation 88
5.2 Lag phase 89
5.3 Aggregation kinetics 97
5.4 Aggregation kinetics on β-barrel seed 98

5.5 Number of aggregates vs. time 103
5.6 Pathway diagram: fibrillar seed, $K_{\chi,bulk} = 2$ kcal/mol 105
5.7 Pathway diagram: fibrillar seed, $K_{\chi,bulk} = 1$ kcal/mol 106
5.8 Pathway diagram: fibrillar seed, $K_{\chi,bulk} = 1.5$ kcal/mol 107
5.9 Pathway diagram: amorphous seed, $K_{\chi,bulk} = 2$ kcal/mol 108
5.10 Pathway diagram: β-barrel seed, $K_{\chi,bulk} = 2$ kcal/mol 109
5.11 Pathway diagram: fibrillar seed, $K_{\chi,bulk} = 1.25$ kcal/mol 110
5.12 Pathway diagram: amorphous seed, $K_{\chi,bulk} = 1.5$ kcal/mol 111
5.13 Pathway diagram: amorphous seed, $K_{\chi,bulk} = 1.25$ kcal/mol 112
5.14 Pathway diagram: amorphous seed, $K_{\chi,bulk} = 1$ kcal/mol 113

6.1 Depiction of field variables measuring membrane fluctuations . . . 121
6.2 Pathway diagram of peptides aggregating on a membrane 124
6.3 Distribution of aggregate structure transitions on a membrane . . 125
6.4 Distribution of aggregate structures on a membrane 126
6.5 Aggregate morphologies unique to membranes 127
6.6 Binding/assembly kinetics of aggregates on a membrane 131
6.7 Local ordering of membrane head groups under a bound fibril . . 134
6.8 Membrane fluctuation power spectra 136
6.9 Lipid tilt magnitude and preferred orientation 137

7.1 Aggregates template on surfaces 145

A.1 Desolvation potential 151
A.2 Collapse of Neutral Polymers 153
A.3 Collapse of Methane Polymers 155
A.4 Collapse depends on chain length 156

A.5 Images of methane polymer under different water models 157

Chapter 1

Introduction

1.1 Coarse-Graining

This work involves molecular dynamics simulations of biomolecules, specifically peptides and membranes, using coarse-grained models. Coarse-graining is a technique of representing a high resolution model with a simpler, less detailed one known as the coarse-grained (CG) model. Examples of coarse-grained models are shown in Fig. 1.1, including the widely used MARTINI model. In biomolecular simulations, the high resolution model is frequently an *all atom* or *atomistic* model, meaning that all atoms in the molecule are explicitly represented. This procedure is depicted in the third and forth panel of Fig. 1.1, showing how one can take an atomistic representation of a polypeptide and unite the atoms into a CG model. Popular classical atomistic force fields include CHARMM [1], AMBER [2], and OPLS-AA [3]. Coarse-grained representations of biomolecules typically combine several atoms into a single rigid unit (almost always spherical, with occasional exceptions [4]). Also, some models go beyond combining atoms and represent the entire molecule as a unit, such as the rod-like model [5] in panel 1 of Fig. 1.1. The

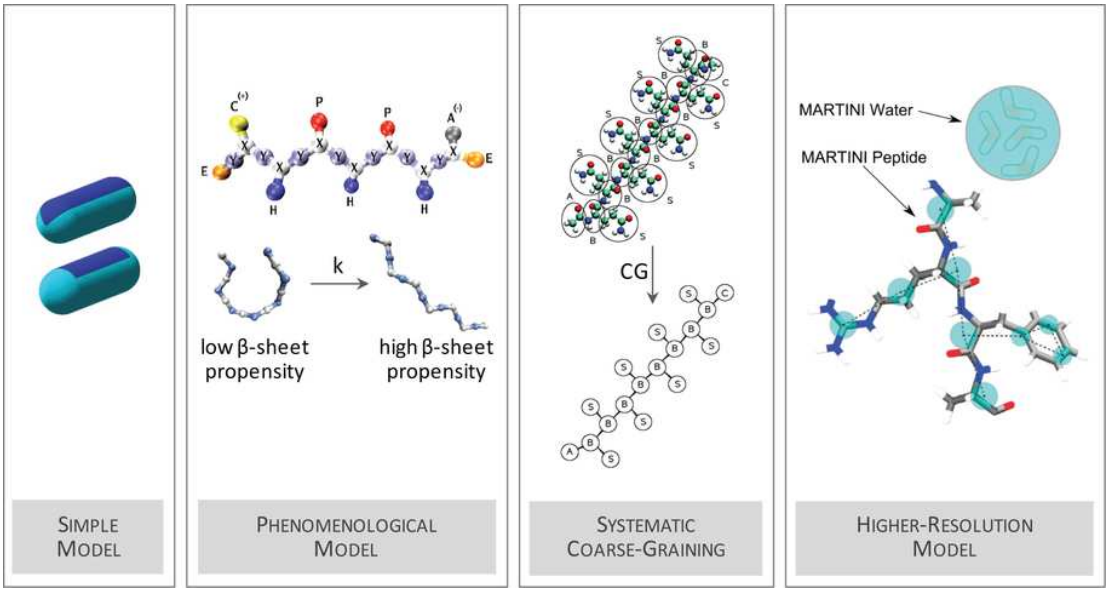

Figure 1.1: Hierarchy of coarse-grained models. Rod-like model of Vacha adapted from reference [5], our phenomenological 3-bead model [7], systematic coarse-graining by MS-CG of polyglutamine adapted from reference [8], and the MARTINI peptide and water model [9].

structural similarity between amyloid fibrils composed of different peptides seems to imply a degree of universality in the mechanism of fibril formation [6], lending support to the use of simplified peptide models that omit some molecular details of the peptide, yet retain the essential physical elements governing aggregation.

The primary computational hurdle with molecular simulations is the necessity of computing interaction forces between all pairs of molecules (such interactions are known as *pair potentials*). This operation scales as the number of atoms squared. For systems involving many atoms, it requires considerable sampling time, making coarse-graining essential. Protein aggregation is an important process where the CPU time required to capture the entire process from monomer to aggregate is prohibitive with atomistic simulations. This is due to it spanning long time scales and involving many molecules, as seen in Fig. 1.2.

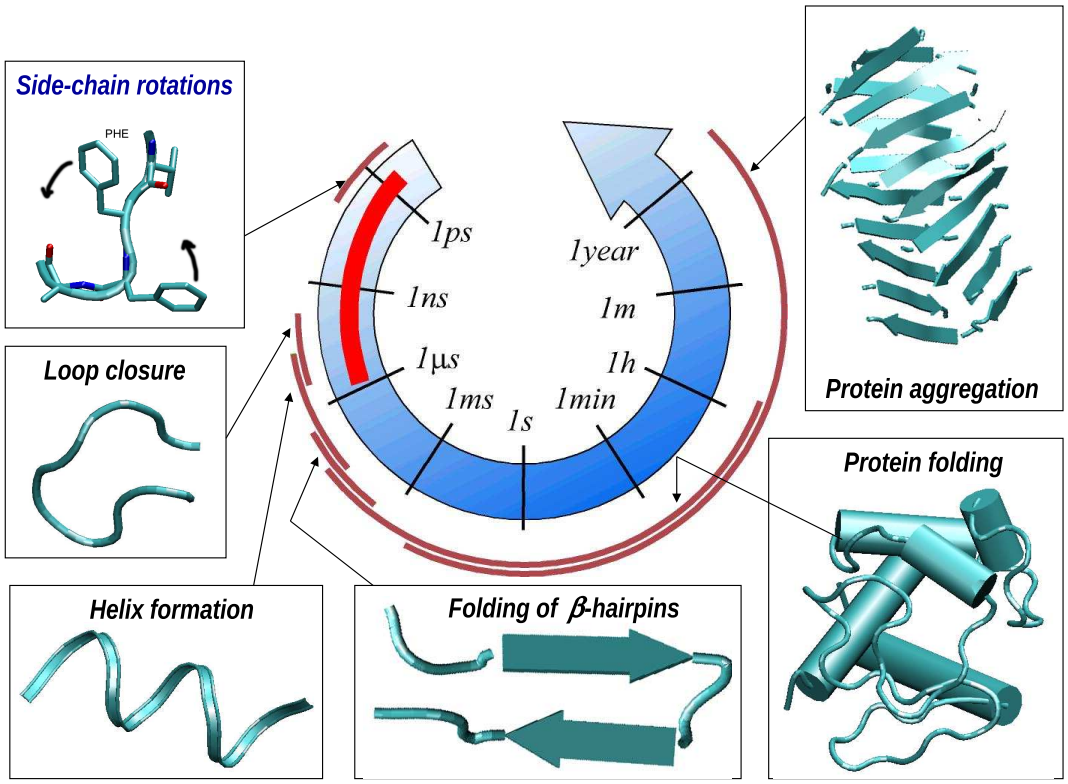

Figure 1.2: Depicts the time scales necessary for various biomolecular processes, with increasing complexity. Protein aggregation is especially difficult to sample due to the involvment of many protein molecules and the extreme time scales necessary to capture the process.

Below we explain the biological relevance of protein aggregation, introduce our peptide model, and discuss some recent developments in computer simulations (contrasting all atom and coarse-grained models) of aggregation.

1.2 Proteins

Proteins play a vital role in an organism, most notably the catalysis of metabolic reactions. The three dimensional structure a protein adopts is necessary to its function. The majority of proteins are not random walk polymers (known as *random coils*) but have a specific structure, or *fold*, as seen in "Protein folding" of Fig. 1.2.

Protein structure is divided into four categories. Primary structure refers to the amino acid sequence, which is the chemical sequence of the polypeptide as manufactured by the ribosome during protein assembly. Secondary structure refers to short length scale ordering of the protein, such as turns, α-helices, and β-sheets, depicted in Fig. 1.2. The tertiary structure is the fold of the protein (Fig. 1.2, bottom right), or the spacial arrangement of the protein's secondary structure. Quaternary structure refers to the ordered assembly of multiple proteins into complexes.

The cell relies on a constant concentration of biologically active proteins in order to function. When proteins do not fold properly, the cell activates a sophisticated machinery of chaperones and proteasomes to assist folding or degrade incorrectly folded proteins. When a severe imbalance of incorrectly versus correctly folded proteins occurs, the cell's defense mechanism is overwhelmed, and proteins begin self-assembling into large, supramolecular structures [11]. This aggregation process has been linked to disease (see Fig. 1.3). Alzheimers Disease,

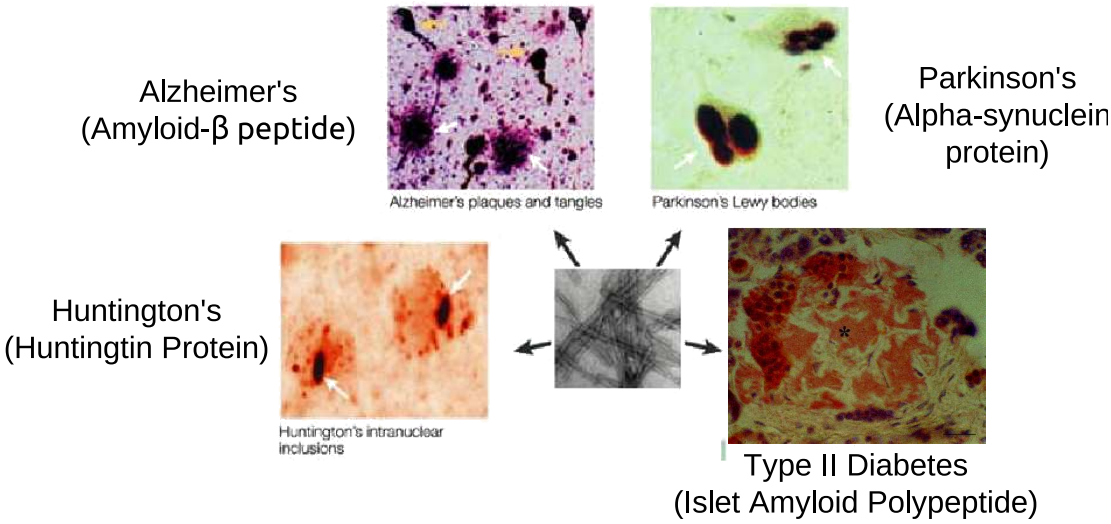

Figure 1.3: A depiction of four important amyloid diseases involving the formation of plaques of protein/peptide aggregates, adapted from reference [10].

Parkinsons Disease, and Type II Diabetes, are just three of over 40 amyloid diseases characterized by clinically observed deposits of protein aggregates known as amyloid fibrils [12]. While mature fibrils have long been suspected to cause amyloid diseases, it is now becoming apparent that smaller aggregates may also lead to detrimental effects of aggregation on the cell. Possible mechanisms include cell membrane damage by small oligomers (by creating ion pores, or mechanically deforming the membrane), or through the disabling interaction of oligomers with healthy proteins [13]. The kinetics of aggregation can be described, in most cases, as a classical nucleation-growth process, with a lag phase where oligomers form, with fibril growth following nucleus formation [14].

However, other mechanisms have been proposed [15] and much remains unknown about the nature of oligomers and the pathways to aggregation. Additionally, aggregation is especially sensitive to experimental conditions [16, 17] and amino acid sequence [6, 18–21]. Even for a single sequence, peptide aggregates

can exhibit polymorphism [22–31]. Changes in solvent, or mechanical agitation, for instance, can lead to alternate aggregation pathways and resulting aggregate morphologies [16, 32–34].

This becomes profoundly important when considering aggregate toxicity [17, 25, 26, 30], which is found to be negatively correlated with aggregate structural stability and positively correlated with hydrophobic exposure. Additionally, cytotoxicity has been demonstrated for pre-fibrillar assemblies of proteins not associated with aggregation diseases [35–37]. Fibrils are, therefore, typically less toxic than unstable, pre-fibrillar oligomers [35, 38–40]. This suggests that stabilizing the fibrillar form of an aggregate may reduce toxicity.

Some peptides have the capability to aggregate into both fibrillar and amorphous structures [41]. While polymorphism is often the result of environmental factors and mechanical agitation of the sample, this is not always the case: some experimental samples yield aggregates with various morphologies under the same external conditions [25–27, 30]. Polymorphism has been shown to result from kinetic effects and the morphology of different seeds (pre-formed template fibrils) present in solution [17, 25, 30]. Hence, kinetic barriers between different morphologies are sufficiently high that a given structure, which may not necessarily be the most thermodynamically stable one, can persist in solution.

Amyloid fibrils can be imaged by electron microscopy and atomic force microscopy, bind to dyes such as Congo Red and Thioflavin T that are specific to β-sheet structure, and have a characteristic cross-β X-ray diffraction pattern [43]. This cross-β spine structure is found to be common among numerous types of amyloid fibrils, with two β-sheets pressed against each other with interdigitating side chains [42]. Examples of these structures can be seen in Fig. 1.4. The core sequence of this cross-β spine is very small, only a few residues long, and is observed

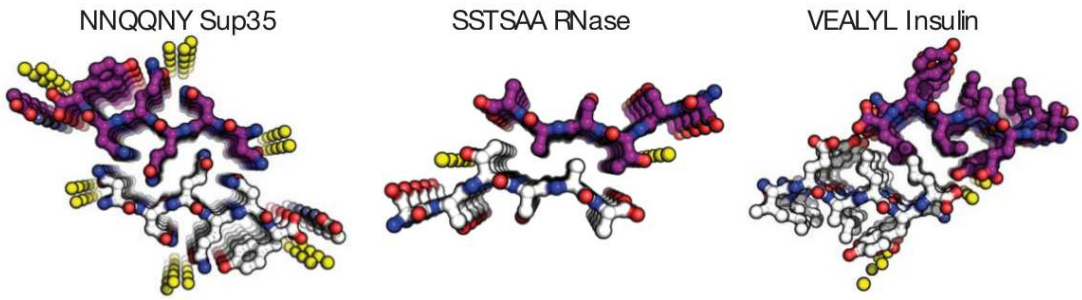

Figure 1.4: Cross sections of the core sequence of cross-β spine aggregates, adapted from Sawaya et al. [42].

to form the backbone of a large class of amyloid fibrils.

The principal challenges in simulating the aggregation process are the associated time and length scales (Fig. 1.2). With this in mind, the choice of protein model and simulation technique must be taken with care. Simulating the earliest stages of aggregation (monomers up to perhaps tetramers) can be performed with atomistically detailed protein models in explicit solvent (using enhanced sampling techniques). Likewise, simulating the end-product of aggregation, starting from structural coordinates from solid state NMR data, can readily be performed in the same detailed manner. However, in order to simulate the aggregation process itself, from monomers to large aggregates, one must be willing to sacrifice atomistic details and invoke coarse-grained models, such as those depicted in Fig. 1.5.

The concentration required for aggregation in the bulk is on the order of micromolar [49], however, some proteins aggregate in the cell at concentrations in the nanomolar range [50]. An explanation for this phenomena is that aggregation is mediated in the cell through interactions with other moieties, in particular biomolecular surfaces in the cell. These surfaces could remodel proteins into aggregation-prone forms, increase the local protein concentration on the cell surface, and serve as templates for aggregation. Confinement to two dimensions

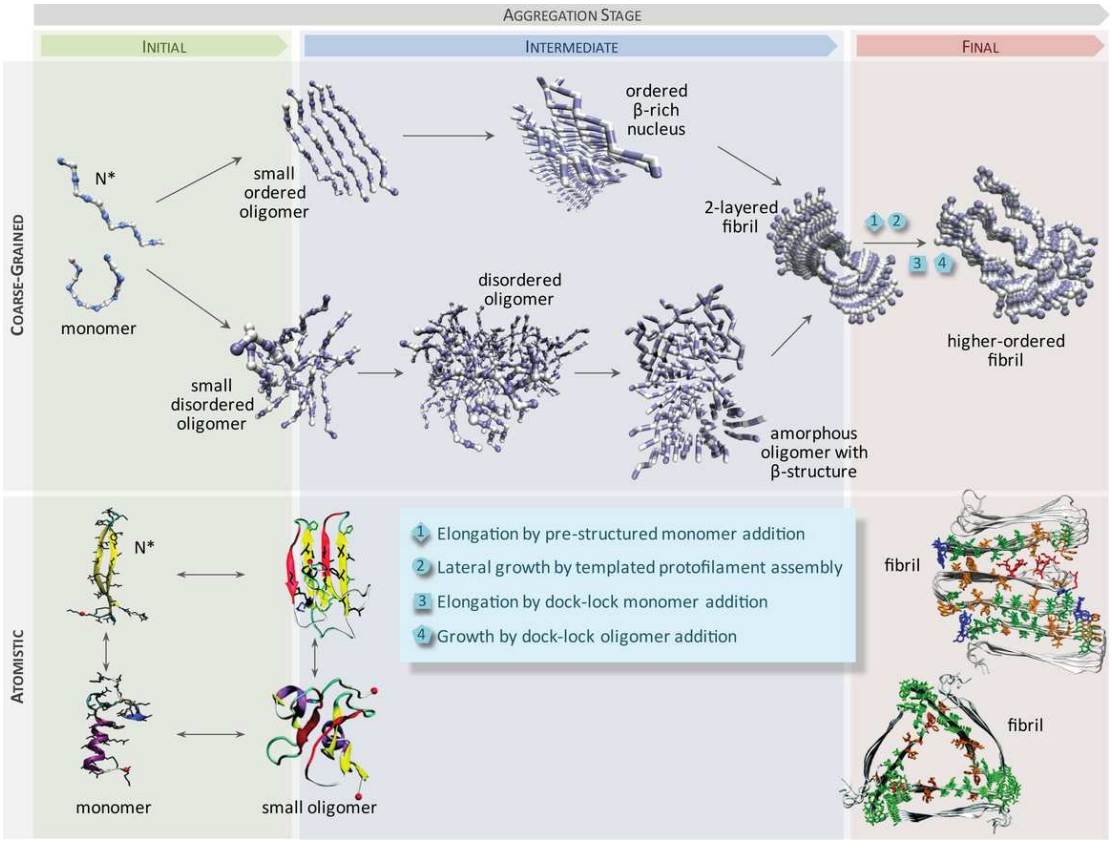

Figure 1.5: An overview of the contributions of atomistic and coarse-grained modeling to the study of protein aggregation. The lower panel emphasizes that atomistic simulations, with present computational resources, are limited to small oligomers, and pre-formed aggregates. Examples are drawn from the assembly of hIAPP peptides, with monomers and small oligomers shown on the left-hand side, and with fibrils shown on the right-hand side. Images adapted from references [44–47]. The upper panel highlights the ability of our coarse-grained peptide model to cover the full spectrum of aggregates, and illustrates different pathways that the peptides can adopt as they self-assemble into fibrils. This image was adapted from reference [48].

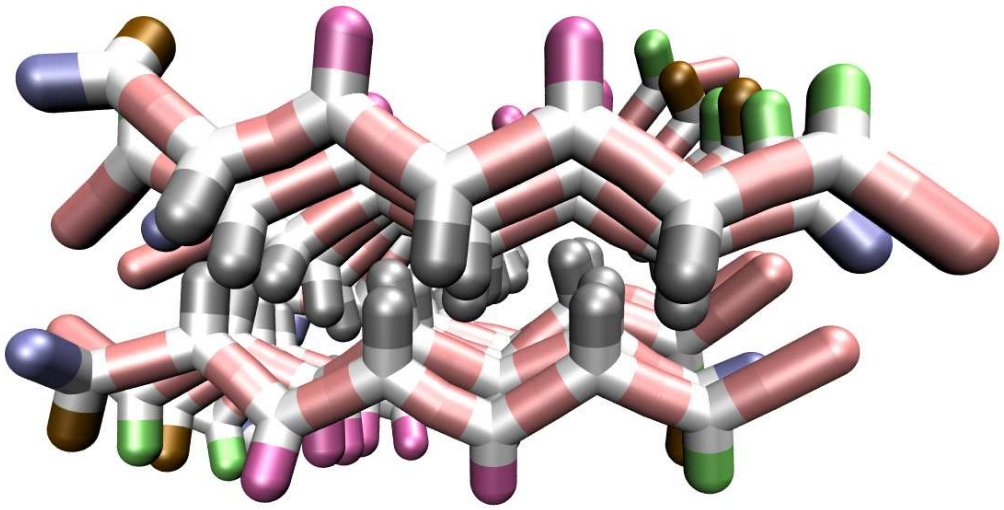

Figure 1.6: Shows the cross section of a double layered fibril using our model. Its cross section is that of a steric zipper with interdigitated hydrophobic residues.

increases peptide collision probability [51], accelerating aggregation compared to bulk conditions [52–54], and surface tethering can lower the entropy cost to form an ordered state [55].

1.3 Our Peptide Model

We employ a coarse-grained peptide model developed by Bellesia and Shea [7]. It is designed to mimic a twisted cross-β structure of amyloid fibrils [56]. Multiple layers stack together into a dry steric zipper with interdigitating hydrophobic

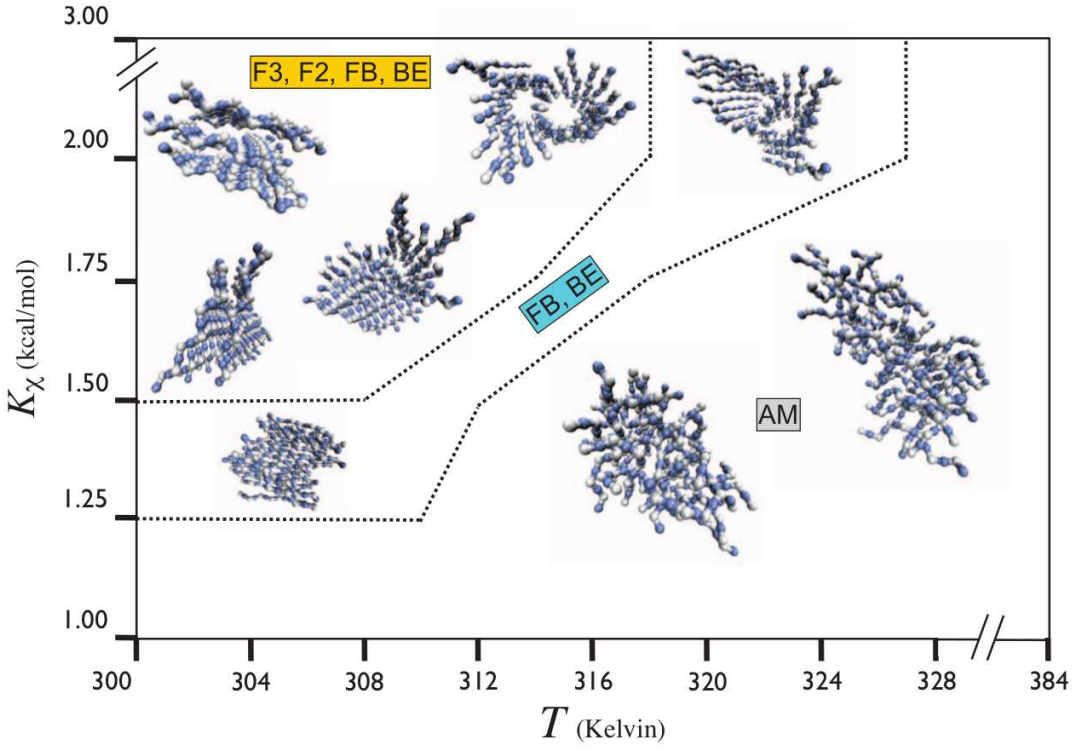

Figure 1.7: A phase diagram depicting the various morphologies observed with our peptide model in the bulk, from reference [57].

residues between sheets, as seen in Fig. 1.6. Analogous β-sheet stacking is commonly observed in the core of a wide range of amyloid fibrils (Fig. 1.4 and [42]).

The most important feature of our peptide model is how it encapsulates a rich diversity of aggregate morphologies into a single tunable parameter with a clear physical interpretation: the chiral rigidity (K_χ) of the peptide backbone. This parameter is the resistance exhibited by the peptide to twisting angles past its optimal right-handed chirality. This chiral preference gives rise to a preferred *left-handed* twist of fibrillar aggregates in the bulk.

Note that our peptide model does not use the full spectrum of amino acids, but rather reduces them to four basic types: hydrophobic, hydrophilic, cationic, and anionic. We consider only short sequences of alternating hydrophobic-hydrophilic

side chains, with oppositely charged residues at the ends. Thus our chiral parameter is effectively tuning sequence.

The behavior of this aggregation model in the bulk has been well characterized by Bellesia and Shea [7, 57, 58]. The phase diagram of the aggregate morphology as a function of chiral rigidity and temperature is shown in Fig. 1.7. One can observe that the system undergoes an order-disorder transition by either raising the temperature or decreasing the chiral parameter. We sometimes refer to this parameter as the system's *β-sheet propensity*, given that we tend to observe β-sheet-rich structures at high values of K_χ and amorphous aggregates at low values.

As a model system, our peptides qualitatively agree very well with experimental observations. It is remarkable that so coarse-grained a peptide can yield known peptide morphologies such as β-barrels and twisted fibrils. Kinetics where fibrillar order emerged through rearrangement of disordered oligomers, seen in several experimental studies [12], were observed for our model [58]. The formation of the β-barrel structure was found to exist sometimes on- and sometimes off-pathway in the kinetics [58], concurring with experimental findings [12, 28].

Below we provide an overview of theoretical and computational approaches to protein aggregation [48, 59, 60]. We begin by discussing atomistic simulations of the early and late stages of aggregation, after which we discuss coarse-grained models as a means of bridging these two regimes (Fig. 1.5). Finally, we conclude with new directions in the simulation of protein aggregation, with a focus on incorporating cellular elements into the modeling.

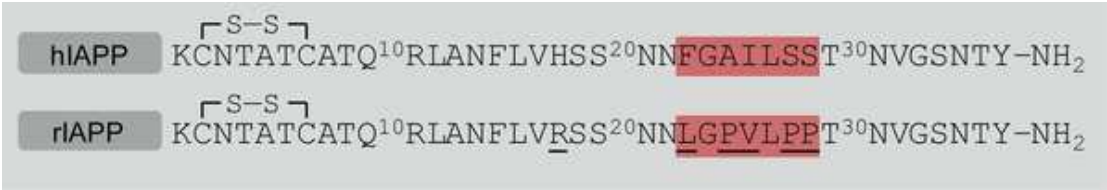

Figure 1.8: Sequences of the aggregating human hIAPP and the non-aggregating rat rIAPP peptides.

1.4 Atomistic Simulations of Monomers, Small Oligomers, and Mature Fibrils

Monomers are the starting point of aggregation, yet they are surprisingly difficult to study experimentally. The reason for this is that aggregation occurs under conditions of high concentration, making it difficult to isolate the behavior of a single molecule. In the case of globular proteins (nonaggregating and spherically structured), it is not the native protein (for which the structure is well characterized) that aggregates, but rather a destabilized aggregate-prone state. In the case of natively unfolded proteins, the protein populates a host of interconverting conformations, making it nearly impossible to resolve a single structure in experiment, particularly with traditional ensemble averaging techniques. The same holds true for small oligomers, being another diverse and transient species.

Simulations, on the other hand, are uniquely positioned to study the behavior of single molecules. Assuming the force fields are adequate (a subject of contention), one can characterize the structures of monomeric and small oligomeric species using enhanced sampling techniques. Methods such as replica exchange molecular dynamics (Chapter 2.4) [61] and metadynamics [62] have been instrumental in yielding early aggregate structural information.

The success of an atomistic force field is in its ability to capture the struc-

ture and kinetics of a specific system. In contrast to our phenomenological peptide model (introduced in Section 1.3) of a generic hydrophobic-hydrophilic peptide, atomistic models strive for a high degree of chemical specificity. Thus in this section we will introduce a specific peptide, which has a number of interesting features with respect to aggregation propensity, as an example to demonstrate the successes and limitations of atomistic simulations. The Islet Amyloid Polypeptide (IAPP, or Amylin) is 37 residues long and is co-secreted with insulin by the pancreatic islet beta-cells. This peptide has a normal function in glucose regulation, but in cases where it is over-expressed the peptide aggregates into amyloid fibrils. The aggregation process (possibly through the interaction of small oligomers with membranes) is linked to Type II Diabetes [63, 64]. The IAPP peptide can be found in several species, from fish to humans, differing by just a few amino acid substitutions. Such point mutations lead to dramatically different aggregation propensities of the peptides. For instance, while the cat and human forms aggregate quite readily, the pig and rat forms do not spontaneously self-assemble into amyloid fibrils. The sequences of the aggregating human IAPP (hIAPP) and of the non-aggregating rat IAPP (rIAPP) are shown in Fig. 1.8. Circular dichroism experiments indicate that IAPP is a random coil, but a secondary chemical shift analysis of NMR spectra reveals that this peptide, while primarily unstructured, can adopt some helical structure, particularly in the N-terminal region [65, 66]. Despite this region being a conserved sequence in all IAPP species, the extent of helical structure was found experimentally to be higher in the non-aggregating rat IAPP variant than in the highly aggregating human variant, implying a cooperative interaction. Simulations are ideal to probe the conformations of these intrinsically disordered peptides and identify whether aggregate-prone conformations can be detected in the amyloidogenic sequences. Computational studies

differ in the protein force field, the solvent model (explicit or implicit), and the simulation protocol (replica exchange molecular dynamics simulations, metadynamics, or long, constant temperature molecular dynamics simulations). Simulations of IAPP monomers all report that the peptides are natively disordered (no single predominant fold as would be the case in a globular protein), and detect marked differences in the monomeric structures adopted by aggregating and non-aggregating IAPP variants. These studies led to the suggestion that hIAPP can populate two conformational families (bottom left panel of Fig. 1.5): an aggregate-competent family (hairpin) and a physiological family (helix-coil) that binds to the membrane and is responsible for the normal role of IAPP as a hormone.

Atomistic simulations, though expected to be the most detailed and precise of classical simulation protocols, do not all give consistent results from force field to force field. The extent of hairpin structure observed varies significantly between force fields. In particular, simulations by Winter (OPLS-AA/L /SPC/E) [67] and Mittal (ff03w/ TIP4P/2005) [68] show hardly any β-sheet content, with the peptides instead forming coil and helical conformations. These simulations would suggest a mechanism by which the helical portion of the peptide is responsible for initiating aggregation. This viewpoint is supported by a number of experimental observations that point to transient increased helicity upon aggregation, and the fact that adding helical-inducing agents (such as HFIP) increases aggregation rates [69].

The first thing to consider regarding these differences is that, sampling issues aside, the force fields were optimized for globular folded proteins, rather than intrinsically disordered proteins, and may over-stabilize secondary structure in unfolded states. More modern force fields, such as the ff03w used by Mittal, have been tweaked to correct for this, but we still have no definitive answer as to

which force field is most correct. A second lesson is that monomer simulations may not be sufficient to determine how aggregation proceeds, as they do not capture the cooperative interactions resulting from inter-peptide conformations. Simulations in the Shea and de Pablo groups have shown that hIAPP can adopt a variety of dimer conformations, and that the formation of dimers can remodel the monomeric structure [45, 70]. A diverse set of dimers was observed in simulations, including dimers of hairpins with interfaces consistent with the aggregation hot spots determined experimentally by Kapurniotu and co-workers [71], as well as dimers that resemble the strand-loop-strand morphology of the fibril [72].

We stress that force fields are still works in progress, that monomeric studies can at best suggest a possible mechanism for aggregation, but that studies of larger oligomers must be performed. We are not yet at the stage where we can simulate large assemblies de novo atomistically, and we will introduce coarse-graining techniques in subsequent sections. But first, we turn to atomistic simulations of fibrils.

Fibrils, the end-products of aggregation, are difficult to study experimentally because they are a large, insoluble, non-crystalline species. Low resolution structural information can be gleaned from TEM and AFM, but perhaps the best way to obtain atomistic information is from solid state NMR. Using a number of constraints including chemical shifts and inter/intramolecular dipole-dipole coupling, detailed coordinates for fibril structures have been obtained. An important advance has been the determination of a strand-loop-strand motif, predicted computationally by the group of Nussinov [73], and observed by solid state NMR [74] in the context of agitated fibrils of the Alzheimer Amyloid-β peptide. This motif was later found to be common not only in polymorphs of the Alzheimer Amyloid-β peptide and its familial mutant, but also for amyloid fibrils of other peptides

[72].

As for most amyloid fibrils, IAPP amyloid morphology depends critically on sample preparation (quiescent versus agitated, buffer conditions, etc.). This polymorphism has been detected in electron microscopy studies, revealing fibrils with ribbon structures, as well as left-handed twisted structures [75]. Simulations have contributed to our understanding of fibril morphology in a number of ways. First, in the computational determination and refinement of structures from experimental data. For instance, new computational algorithms became necessary to derive structural information from ESR spectroscopy experiments [76]. The models that emerged from these studies showed that the β-strands of the twisted polymorph had an in-register parallel arrangement, with a pronounced strand stagger and a helical twist resulting from monomer stacking.

Molecular dynamics simulations play a role not only in refining NMR structures, but also in exploring alternate fibril morphologies, as well as cross-seeding [77]. Simulations have shown that the protofibrils can stack in different ways, with different interfaces, and with more than just two subunits [46, 77, 78]. A symmetric triangular arrangement is remarkably stable [47]. This structure, yet to be observed experimentally, is reminiscent of the 3-fold symmetric structure of quiescently grown Aβ40 fibrils, solved by solid state NMR [79]. It is possible that this arrangement, along with the strand-loop-strand motif, constitutes a general pattern for many amyloid peptides. Two hIAPP morphologies from simulations are shown on the lower right of Fig. 1.5.

Additionally, molecular dynamics simulations can provide important insights into the dynamical properties of fibrils. Indeed, solid state NMR samples are mostly dehydrated and experiments are performed at low temperatures. Solvating the resulting structure and running simulations at ambient temperature gives

insights into the stability and flexibility of the structures. In the case of hIAPP, the peptides forming the protofilament are tightly arranged, and the loop region is mostly dry. This is in sharp contrast to protofilaments of the Alzheimer Amyloid-β40 and 42 peptides, which have the same overall topology, but expose loop regions that permit channels of water [80, 81].

1.4.1 Coarse-Grained Models of Protein Aggregation

In the previous paragraphs, we highlighted examples of detailed atomistic simulations of the early and late stages of aggregation. Missing are all the crucial intermediate steps between small oligomers and mature fibrils. Several important issues such as the detailed pathways of aggregation have so far eluded experimental capability. Furthermore, with present day computational resources, these questions cannot be answered with atomistically detailed models. A viable alternative are coarse-grained (CG) models, the insights of which are the focus of this section.

Coarse-graining involves simplification of the peptide sequence and interactions. This procedure comes with a trade-off of accuracy versus computational efficiency, and should depend on the smallest important length scale of the system of study. In practice, however, it is non-trivial to determine a priori to what extent small coarse-grained length scales affect the physics of aggregation.

A wide range of CG models with different resolutions and parameterization schemes have been introduced in recent years. Fig. 1.1 summarizes the main classes of CG models, from basic phenomenological models to more sophisticated ones parameterized from atomistic or experimental data.

The most highly coarse-grained models represent each peptide as a single

unit. Examples include the cuboid model of Muthukumar [82], the tube model of Auer [83, 84], the rod-like model of Vacha (shown in Fig. 1.1) [5], and the orientable stick model of Irback [85]. These models sacrifice sequence-level resolution, but allow the simulation of up to an impressive 10^5 peptides. A slightly higher resolution model involves coarse-graining over atomic length scales, for instance, with one or more beads per residue. These models can be on- or off-lattice, phenomenological, or parameterized more explicitly from atomistic or experimental data. In a lattice model, the permitted atomic coordinates of the molecule are constrained to a grid. Examples of lattice phenomenological models include the one-bead per residue model of Li [86, 87], the two-bead model of Bolhuis [88], and the multi-bead model of Frenkel [89]. Off-lattice phenomenological models include the two-bead Caflisch model [90, 91] and our three-bead peptide model [7, 57, 58] (shown in Fig. 1.1). Phenomenological models are not meant to reproduce a peptide sequence, but rather to elucidate the important physical properties that govern peptide self-assembly. They typically consist of a backbone and of hydrophobic and hydrophilic side chain beads, rather than the full array of amino acids. Instead of parameterizing each bead to a specific amino acid, average interaction energies are obtained. The aim of these models is to explore interaction space, and the energetic parameters are varied to mimic the aggregation propensities of different amino acid compositions.

The phenomenological models described in the previous paragraph are all capable of generating large fibril assemblies, but they do not provide sequence-dependent information. Non-phenomenological models are necessary to describe the properties of a particular sequence. These models can be either high or low resolution, but they are all parameterized from atomistic or experimental data. One coarse-graining approach is systematic coarse-graining, a bottom-up method-

ology for obtaining the optimum coarse-grained potentials to match the behavior of all atom simulations or experimental data [8, 92]. Recent versions of this technique include the relative entropy method developed by Shell [93], the multiscale coarse-graining (MS-CG) method developed by Voth et al. [94], and the iterative Boltzmann inversion (IBI) method developed by Mller-Plathe et al. [95]. These systematic CG methods map from an all atom to a relatively simple 2-3 bead representation, not dissimilar in resolution to the phenomenological models described above (see Fig. 1.1 for a polyglutamine mapping used in a MS-CG simulation). A nice feature of systematic coarse-graining methods is that they eliminate non-essential degrees of freedom, and allow an analysis of which features are truly necessary to describe aggregation. However, their primary drawback is that they already necessitate obtaining good all atom statistics in order to parameterize the CG model. Additionally, by their nature, these potentials are system specific, and in principle require reparameterization of all interactions if the system changes in any way. Nonetheless, these methods are ideal for studying the self-assembly of many like molecules, since the inter- and intramolecular potentials are typically obtained from a system of fewer molecules.

High resolution non-phenomenological CG models include the MARTINI model (Fig. 1.1) [96], the OPEP model [97], and the PRIME Model [98]. The MARTINI model unites roughly four heavy atoms to a single bead (both in the protein and water models), and is parameterized to match experimental thermodynamic data. The OPEP model has an all-atom backbone with CG side chains, and is parameterized from a set of test proteins to predict the lowest energy structures. The PRIME model has a similar level of resolution to the MARTINI model and is parameterized via learning algorithms to maximize the energetic gap between PDB structures and decoys.

The principal advantage of coarse-graining is to make large scale systems accessible to computer simulation. These include systems of hundreds of peptides over tens of microseconds [99], or high throughput studies of hundreds of sequences to discover aggregate-prone sequences [100]. Exploring these time and length scales reveals new features in the pathways of aggregation. A few consistent pictures emerge from simulations using different coarse-grained resolutions.

Even the simplest peptide representations (cuboid, rod, and stick models) capture the sigmoidal kinetics of aggregation observed experimentally [5, 82, 85, 101–104]. Despite their simplicity, these models shed new light into the origin of the sigmoidal kinetics, linking it to a two-dimensional nucleation event involving the formation of at least a two-layered sheet [82, 85], consistent with the steric zipper picture (Figs. 1.4 and 1.6). The phenomenological models of Shea, Caflisch and Vacha provided further insights into the nucleation process, showing that the pathways to aggregation depend critically on the nature of the peptides. They each introduced a parameter in their model to set the aggregation propensity of the peptide (in our peptide model, for instance, through modulation of backbone rigidity). Changing this parameter is comparable to introducing a mutation or altering the solvent conditions. Their simulations showed that peptides with low β-sheet propensity aggregated via disordered oligomers, from which β-structure emerged, (a nucleated conformational-conversion model), whereas high-β sheet propensity peptides populated N* (aggregate-competent) conformations that assembled directly into ordered β-rich oligomers [57, 58, 90, 91]. These two limiting cases are shown in the upper panel of Fig. 1.5. The above coarse-grained simulations, although not sequence specific, provide important insights into possible aggregation pathways that may become accessible under different experimental conditions. Indeed, experiments on the SH3 protein have shown that aggrega-

tion to fibrils can proceed via ordered or disordered aggregates depending on pH [16]. The pH can affect the structures of the peptides (analogous to changing the flexibility parameter in our coarse-grained model), leading to one pathway being favored at high pH, and another at low pH. These simulations reconcile the experimental observation of both structured and unstructured/fluid oligomeric assemblies during the fibril formation process [105–108]. The non-phenomenological models, which probe specific protein sequences, gave insight into the nucleation mechanism of specific proteins. For instance, the assembly of polyalanine was shown to proceed via formation of disordered oligomers, in both simulations using systematic coarse-graining (relative entropy method) [92] with molecular dynamics simulations, and the PRIME model with discontinuous molecular dynamics [109].

Coarse-grained models have led to new insights into fibril growth as well. To study elongation, even more so than nucleation, requires a large number of peptides. The simplest CG models have been important in elucidating the fibril elongation process. The cuboid model of Muthukumar [82], the tube model of Auer [83], and the one-bead lattice models of Li [87], among others, captured a mechanism for elongation, in which short, less stable protofibrils become peptide reservoirs furthering growth of the primary fibril. We will show in Chapter 5 that the mechanism of fibril growth, much like the nucleation process described in the preceding paragraph, depends on the β-strand propensity of the peptide. In the case of peptides with high β-strand propensity, elongation occurs by addition of pre-structured N* monomers or small ordered oligomers to the ends of the existing fibrils, and lateral growth by addition of a pre-formed β-sheet. Peptides with lower β-strand propensity, on the other hand, bind to the fibril as unstructured monomers or small oligomers and use the fibril as a template to rearrange their

structure into a fibril-commensurate structure (dock-lock mechanism [110–112]). As in the case of nucleation, these simulations reconcile many disparate experimental observations regarding fibril growth (including elongation by monomer addition [113] via a dock-lock mechanism [114], and addition of oligomers to fibril ends [115]), in terms of the nature of the aggregating peptides. Simulations using the higher resolution PRIME model have shed light into the detailed pathways of assembly of specific sequences, for instance showing a templated assembly mechanism where fibrils elongate by the addition of monomers to the ends, one at a time, in the case of fragments of the Aβ and Tau peptides [116, 117]. A simulation of a fragment of the IAPP peptide using the MARTINI model showed that the fibril growth mechanism was temperature dependent, with elongation dominating lateral growth at lower temperatures, a preference lost as temperature is increased [118].

Efforts in coarse-graining extend beyond the molecular length scale. Buehler and co-workers developed a continuum treatment in which the fibril itself is an elastic chain of beads [119]. This level of detail sacrifices an analysis of how an amyloid fibril's constituents assemble for the ability to study events that occur on much longer time and length scales, in this case plaque assembly of up to 240 *fibrils*. Eom et al. have employed a CG normal mode analysis on all atom simulations to study elastic modes of an hIAPP fibril (bending, torsion, stretching) for various structural hierarchies (e.g., parallel/antiparallel β-sheets) [120]. They show how fibril structure patterns such as a stacked antiparallel β-structure increase the fibril bending rigidity, and found shear effects necessary to explain the behavior of mechanical rigidity as a function of size. Finally, fibril self-assembly has been studied using kinetic models that have revealed the importance of secondary processes, including fibril fragmentation, lateral growth, and monomer-dependent

nucleation, in determining the experimentally observed kinetic profiles [121–124].

1.4.2 Aggregation in the Cellular Milieu

Aggregation in vivo occurs in the complex environment of the cellular milieu, in the presence of large biomolecular surfaces such as membranes [13, 125]. Such systems are in general too large for treatment by current atomistic simulations, and therefore are prime candidates for the development of modern coarse-grained models. The transition from simulations of aggregation in bulk solution to aggregation on various interfaces is a relatively recent development. It is the next logical step in attempting to model the full complexity of the in vivo environment. To this end, CG models have been used to simulate protein aggregation on lipid vesicles [126], on small lipid micelles [127], in the presence of lipid surfactant [128], on a membrane surface [129] (also see our work in Chapter 6), and inside lipid bilayers [130–133].

Lipids change the environment of the proteins, affecting their structure. For instance, Samson et al. showed using a MARTINI model that hydrophobic mismatch (the size of the protein's hydrophobic region relative to the thickness of the membrane's hydrophobic core) can drive protein aggregation [133]. Likewise, in Chapter 6, we use a phenomenological model combining a CG peptide amyloid model [7, 57] with the Brannigan-Brown CG lipid bilayer model [134] to show how the membrane biases peptides to elongated β-sheet morphologies on the membrane surface, even if they formed amorphous aggregates in the bulk. In turn, aggregates can alter the structure of a membrane or other lipid assembly. Rather dramatically, for example, N-BAR aggregates can skew the topology of a spherical vesicle into a tubular network [126]. The hIAPP peptide is known to interact and

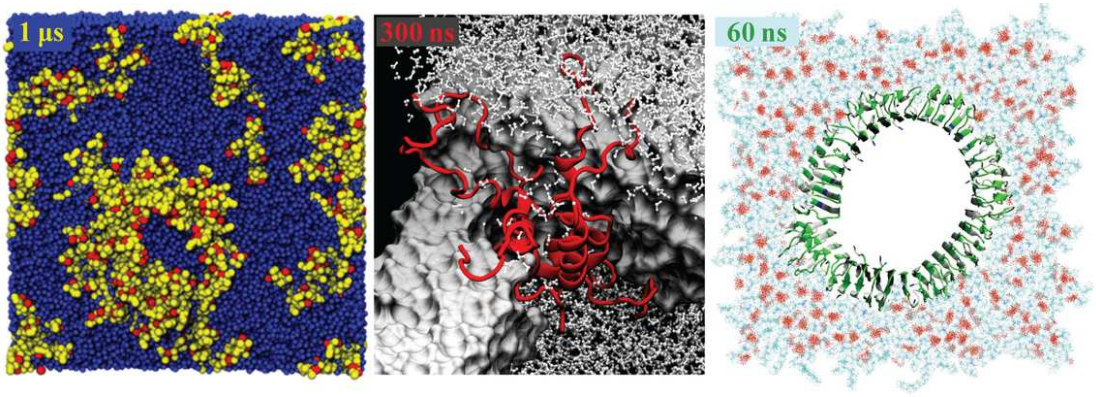

Figure 1.9: The interaction of hIAPP with membranes. First panel: Snapshot from a coarse-grained MARTINI simulation of the assembly of hIAPP in a membrane. Adapted from reference [130]. Second panel: Snapshot of a simulation of an atomistic model of a pore consisting of five helical hIAPP peptides. Adapted from reference [130]. Third panel: Snapshot of a simulation of an atomistic model of a pore consisting of β-strand-loop-strand hIAPP peptides. Adapted from reference [138].

damage cell membranes, but the mechanism of cytotoxicity remains a matter of debate. Ion-like channels consisting of hIAPP oligomers have been reported [135], as has fibril growth on the surface of membranes, with vesicles visibly distorting in the process [136]. Interestingly, the non-toxic and non-fibrillizing rIAPP is equally capable of forming pores. A two-stage mechanism has been proposed in which hIAPP oligomers first form channels, followed by fibril growth, both contributing to toxicity [135, 137]. As described below, simulations can provide insights into the interactions between the hIAPP peptide and membranes, as well as suggest structural models for hIAPP ion channels.

Binding and adsorption of hIAPP to model membranes were investigated by several groups using both atomistic and coarse-grained models [139–141]. To investigate why rIAPP-membrane oligomers are non-toxic, Karttunen and coworkers performed a multiscale modeling simulation in which they first used the

CG MARTINI model to simulate the assembly of 36 hIAPP and 36 rIAPP peptides for 26 μs, with the peptides initiated in a helical conformation [130]. hIAPP monomers remained inside the membrane, while rIAPP monomers migrated to the surface, consistent with experimental observations of differences in orientation of these two peptides with respect to the membrane [142, 143]. In addition, the hIAPP peptides formed much larger oligomers than rIAPP peptides. A snapshot of a CG hIAPP oligomer is shown on the left hand panel of Fig. 1.9. Structures obtained from the CG models were used to build atomistic models of pentamer oligomers, which were then simulated for 0.3 μs. The hIAPP pentamers resembled barrels and were stable, but lost significant helicity during the course of the simulation. A snapshot of the hIAPP pentamer is shown in the central panel of Fig. 1.9.

1.5 Concluding Thoughts

We have highlighted some recent advances in simulations of protein aggregation, from atomistic to coarse-grained simulations, to provide the reader with a context in which to understand our work. Much work remains in the development of atomistic force fields, enhanced sampling protocols, and new coarse-graining techniques. We hope we have demonstrated the necessity of coarse-grained models in order to sample the full aggregation process. In Chapter 2 we will describe the force field and geometry of our coarse-grained models which we shall use in the work from Chapters 3–6. Chapter 3 will focus on the thermodynamics of peptide aggregation on a solid surface, showing how the surface biases toward ordered fibril structures. Chapter 4 will describe the initial kinetics of aggregate formation on the same solid surface, contrasting kinetically trapped states with the equilibrium

morphologies computed in Chapter 3, and elucidate how the surface guides the pathways to aggregation. Chapter 5 discusses the kinetics of peptide aggregation on the surface of a pre-formed aggregate seed, giving an analysis of how the seed modulates aggregation mechanisms such as condensation-ordering and templated growth. In Chapter 6 we move to an analysis of aggregation on the surface of a lipid bilayer. We study how a fluid surface affects aggregation kinetics, and also how the presence of ordered fibrils affects the membrane fluidity. In all of these chapters, the primary focus is a study of the effect of various surfaces on the aggregation of our peptide model, looking for general features of surface-bound aggregation and contrasting how the specific nature of different surfaces yields unique aggregation kinetics.

Chapter 2

Methods

2.1 Peptide Model

2.1.1 Model Geometry

The peptide model we employ for molecular-dynamics studies of peptide aggregation consists of seven residues. It is depicted in Fig. 2.1. A coarse-grained model, it includes twenty-three interaction centers per peptide. It is not intended to model a specific peptide sequence. Rather it is designed as a simple physical model to capture the phenomenology of peptide aggregation and to elucidate which components of the model cause each of the diverse aggregation pathways.

The peptide backbone alternates between two types of interaction centers (X and Y). Sidegroups are attached to the backbone on the X sites. At the ends are cationic and anionic groups (C and A), which have respective charges of $+e$ and $-e$. The peptide residues are in trans conformations alternating between hydrophobic (H) and polar (P) groups. We include terminal groups, or endcaps (E), which interact with purely repulsive steric potentials with all groups. The residue

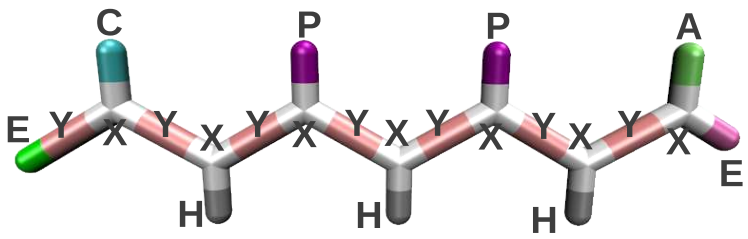

Figure 2.1: Depicts the seven-residue coarse-grained peptide we employ in molecular dynamics simulations of peptide aggregation. The peptide consists of two backbone interaction centers per residue (X and Y), hydrophobic side chains (H), polar side chains (P), cationic (C) and anionic (A) side chains with charges $+e$ and $-e$ respectively, and end caps (E). Typically, in figures of this peptide, we show only the backbone (X and Y) for simplicity.

sequence used is ECHPHPHAE, except in the work of Chapter 6, where the hydrophobic and hydrophilic residues are exchanged: ECPHPHPAE. This sequence is convenient since it is a short peptide sequence favoring fibrillar alignment, giving a rich diversity of aggregate morphologies at modest computational expense. Its packing into a fibril is similar to β-spine structures observed experimentally (compare Figs. 1.6 and 1.4). While our model does not use explicit water, we account for some of its effects by the hydrophobic interaction and Langevin dynamics.

2.1.2 Potentials

The energetics of the peptide system consist of pair interactions (both bonded and nonbonded), three-body angle potentials, and four-body dihedral potentials. The full Hamiltonian, a functional of all interaction site coordinates, is

$$H = U_{\text{bond}} + U_{\text{angle}} + U_{\text{dihedrals}} + U_{\text{NB}}. \tag{2.1}$$

We shall now show these terms in detail.

Bond Length Potential

$$U_{\text{bond}} = \sum_{\text{bonds}} \tfrac{1}{2} K_{\text{b}(ij)} (r_{ij} - r_{0ij})^2, \tag{2.2}$$

where $K_{\text{b}(ij)} = 200.0$ kcal/mol Å^{-2}, r_{ij} is the bond length between atoms i and j, and $r_{0ij} = 2.0$Å.

Angle Potential

$$U_{\text{angle}} = \sum_{\text{angles}} \tfrac{1}{2} K_{\theta(ijk)} (\theta_{ijk} - \theta_{0ijk})^2, \tag{2.3}$$

where $K_{\theta(ijk)} = 40.0$ kcal/mol rad^{-2}, θ_{ijk} is the angle between successive atoms ijk, $\theta_{0iXk} = 2\pi/3$, and $\theta_{0XYX} = \pi$.

Dihedral Angle Potential

Dihedral potentials along the backbone are defined by:

$$U_{\text{dihedrals}} = \sum_{\text{dihedrals}} \left(D \cos\left(3\alpha_{ijkl}\right) + G \cos(\alpha_{ijkl}) \right), \tag{2.4}$$

where $D = G = 0.25$ kcal/mol, and α_{ijkl} is the dihedral angle, which takes the value of 0 in the cis conformation and $\pm\pi$ in the trans conformation (favored by this potential). A chiral dihedral term determines the stiffness of the backbone:

$$U_{\text{chiral}} = \sum_{\text{chiral}} K_\chi \cos(\alpha_{ijkl} + \delta), \tag{2.5}$$

where K_χ is the chiral dihedral stiffness (or β-sheet propensity) and varies from 1 to 2 kcal/mol depending on the simulation, and $\delta = -\pi/9$ breaks chiral symmetry to favor a right-handed, near-trans conformation.

2.1.3 Nonbonded Interactions

Pairwise nonbonded interactions (both inter- and intra-peptide) are modeled as a Lennard-Jones potential term plus a Coulomb interaction to include charges:

$$U_{\mathrm{NB}} = \sum_{\mathrm{pairs}} \left\{ 4\epsilon_{ij} \left((\sigma_{ij}/r_{ij})^{12} - \lambda_{ij}(\sigma_{ij}/r_{ij})^{6} \right) + C_C \frac{q_i q_j}{r_{ij}} \right\}. \tag{2.6}$$

The sum is over all interaction center pairs ij. The interaction distance parameter is always $\sigma_{ij} = 2.0$Å with the exception of $\sigma_{XY} = 3.0$Å. Backbone-backbone and sidechain-sidechain interactions have parameters $\epsilon_{XX} = \epsilon_{XY} = \epsilon_{YY} = 0.5$ kcal/mol, $\epsilon_{HH} = 0.3$ kcal/mol, $\epsilon_{PP} = 0.04$ kcal/mol, $\epsilon_{HP} = 1.0$ kcal/mol and $C_C = 16.603$ kcal/mol e^{-2}Å. The only charged interaction centers are C and A with charges $+e$ and $-e$ respectively. We use $\lambda_{ij} = 1$ generally, with the following exceptions: hydrophobic-polar interactions have $\lambda_{HP} = 0.01$, and purely repulsive interactions ($\lambda_{ij} = 0$ and $\epsilon_{ij} = 1.0$ kcal/mol) occur for backbone-side-groups (XH, XA, YH, *etc.*) and interactions involving the end caps (EE, EX, *etc.*). The non-Coulombic part of pair interactions between charged groups (AA, AC, CC) likewise has $\lambda_{ij} = 0$ and $\epsilon_{ij} = 1.0$ kcal/mol.

2.1.4 Peptide-Surface Interactions

In the work of Chapters 3 and 4 we conduct simulations of the seven-residue peptide model on a hydrophobic solid surface, depicted in Fig. 2.2. This surface

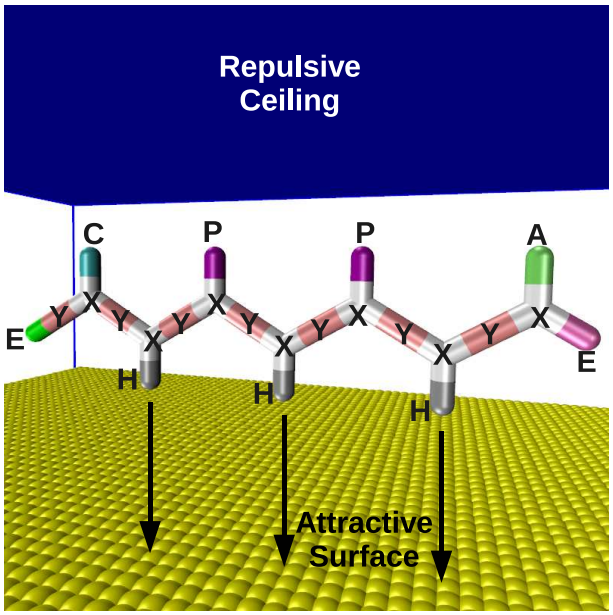

Figure 2.2: Depicts the elements of the model used in Chapters 3 and 4: the peptide, the surface, and the repulsive ceiling potential. The peptide model consists of two backbone interaction centers per residue (X and Y), hydrophobic side chains (H), polar side chains (P), cationic (C) and anionic (A) side chains with charges $+e$ and $-e$ respectively, and end caps (E).

consists of spherical interaction centers arranged in a square lattice of spacing 2Å. The positions of the surface beads are fixed, and interact only with the peptides.

Each hydrophobic residue of a peptide experiences an attractive Lennard-Jones interaction with each surface bead,

$$V_{\mathrm{LJ}} = 4\epsilon \left((\sigma/r)^{12} - (\sigma/r)^{6} \right), \tag{2.7}$$

mimicking the hydrophobic effect in water. Here r is the separation between a peptide's hydrophobic residue and a surface bead. We use varying degrees of surface attraction. The values $\epsilon = 0.30$, 0.42, and 0.55 kcal/mol are referred to respectively as weak, medium, and strong surface attractions.

The remaining interaction sites of the peptide (non-hydrophobic), experience the repulsive terms of the Lennard-Jones potential:

$$V_{\mathrm{LJ}} = 4\epsilon(\sigma/r)^{12}, \tag{2.8}$$

with the same values of ϵ and σ used for the hydrophobic beads in the Lennard-Jones potential.

In principle, since our simulations use periodic boundary conditions, both sides of the surface would be exposed to peptide binding. However, we prevent this anomaly using a repulsive ceiling potential which prevents peptides from exceeding heights of 50Å above the surface (shown in the top of Fig. 2.2). It is implemented as a harmonic potential:

$$U_{\mathrm{ceiling}} = \sum_{\mathrm{atoms}} \Theta(z_i - z_0) \tfrac{1}{2} K_c \cdot (z_i - z_0)^2, \tag{2.9}$$

where $\Theta(z)$ is the Heaviside function (ensuring the potential is only applied when

$z_i > z_0$), z_i is the z-coordinate of atom i, $z_0 = 50$Å, and $K_c = 10$ kcal/mol Å^{-2}. Thus the peptides are bounded between the surface and a 50Å ceiling.

2.2 Lipid Model

In Chapter 6 we combine a variant of a coarse-grained peptide amyloid model described above with the Brannigan-Brown coarse-grained lipid bilayer model [134]. The model is shown in Fig. 2.3 [144]. In Chapters 3 and 4 we use the peptide model to study the effect of backbone rigidity on the kinetics of assembly and on the morphology of aggregates formed by these peptides in the bulk and in the presence of a solid surface [7, 57, 58, 145–147]. The Brannigan-Brown lipid model was developed as a generic solvent-free coarse-grained model for studying the biophysics of self-assembling lipid bilayer systems. It has been used extensively to test and validate various analytical models, exhibiting behavior similar to more detailed lipid models found in the literature [134, 148–152].

The peptide potentials are identical to the ones used in Chapters 3–5 but have been converted to the dimensionless units used for the membrane model. The original potentials can be recovered using the reduced units: $\sigma = 7.5$Å and $E_0 = 0.6573$ kcal/mol.

The lipid model consists of a head bead, an interfacial bead, and 3 tail beads. The harmonic bond potentials have stiffness and equilibrium separation of $k_r = 9995\ E_0\sigma^{-2}$ and $r_0 = 1.0\sigma$. The harmonic bond angles have stiffness and equilibrium angle of $k_\theta = 7.3\ E_0$ rad^{-2} and $\theta_0 = \pi$. There is no energetic cost associated with dihedral rotations.

The pair potentials governing lipid interactions are defined through three

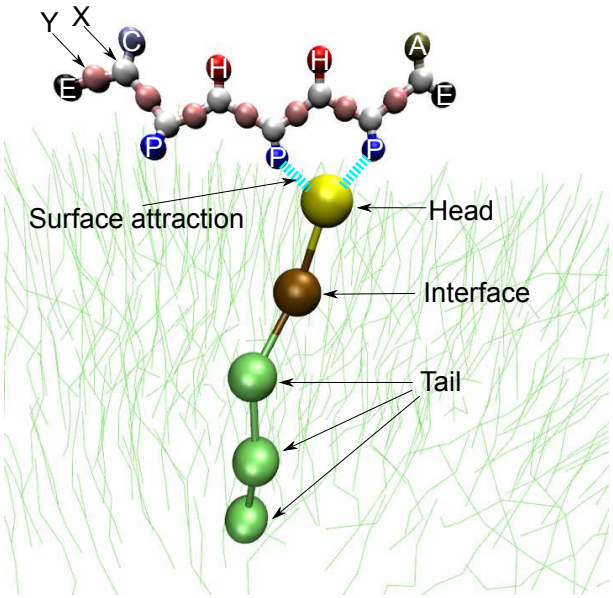

Figure 2.3: Geometry and interaction between peptides and lipid molecules. A single lipid is highlighted, with the remaining lipids in the bilayer depicted as thin green lines. The interaction sites of the peptide are the backbone (X and Y); polar, hydrophobic, cationic, and anionic side chains (P, H, C, and A); and the endcaps (E). The interaction sites of the lipid are the head, interface and tail beads. The polar side chains of the peptide experience an attractive interaction with the head groups of the lipids. In other images of the peptides we will show only the XY backbone for clarity.

terms:

$$U_{core}(r) = c_{core}(\sigma/r)^{12}, \tag{2.10}$$

$$U_{int}(r) = -c_{int}(\sigma/r)^{2}, \tag{2.11}$$

$$U_{tail}(r) = -c_{tail}(\sigma/r)^{6}, \tag{2.12}$$

where $c_{core} = 0.4\ E_0$, $c_{int} = 3.0\ E_0$, and $c_{tail} = 1.0\ E_0$. The hydrophilic lipid heads (see Fig. 2.3) interact with all other lipid sites only through repulsive U_{core} interactions. Interface beads interact with other interface beads through both re-

pulsive U_{core} interactions and also the soft attractive U_{int} interaction. Tail beads interact both with other tail beads and with interface beads via a Lennard-Jones type interaction composed of both U_{core} and U_{tail} contributions. Note that U_{core} and U_{tail} are truncated (and employ a force switching function to avoid discontinuities [148]) at 2σ, and U_{int} at 3σ. Truncation of the otherwise long ranged U_{int} is an essential component of the interaction introduced to mimic the hydrophobic effect and should not be viewed as an approximation to a true r^{-2} potential.

Protein-Lipid Interactions

Attraction of the peptides to the bilayer is modeled as a Lennard-Jones interaction of strength ϵ between polar peptide sites and the lipid head beads. We varied between $\epsilon = 1.29\ E_0$ (weak interaction) and $3.04\ E_0$ (strong interaction), using an interaction range of $\sigma_{ij} = 0.53\sigma$, i.e., $U_{LJ} = 4\epsilon((\sigma_{ij}/r)^{12} - (\sigma_{ij}/r)^6)$. Interactions between other possible lipid-peptide site combinations (e.g., peptide backbone to interface bead or hydrophobic side chain to tail bead) are purely repulsive, including only the r^{-12} component of U_{LJ}. We study a range of attractions between the membrane and the peptide to mimic lipids with different head groups, as head group composition has been shown to affect peptide-lipid binding [153–155].

2.3 Langevin Dynamics Implicit Solvent Model

The representation of water in classical molecular dynamics simulations is a challenging problem. There are several atomistic representations of water, such as TIP3P [156] and SPC/E [157]. In simulations of protein folding, atomistic representations are common because a protein can occupy a sphere that is hardly larger than the protein itself. Thus one can populate the empty space with water with-

out introducing significantly more atoms than are necessary for the protein itself. The process of fibril *formation* is altogether different. In these simulations, the constituent proteins are initialized apart from each other, that is, with significant gaps between them that would require filling with solvent.

Coarse-grained water models reduce the number of atoms used in pair computations significantly, such as the MARTINI water model which takes advantage of water's tetrahedral structure to represent four molecules by a single bead (see Fig. 1.1). However, even CG water models are prohibitive for larger systems consisting mostly of solution.

We adopt an implicit solvent model using Langevin dynamics. This model consists of three components. The first treats water as a thermal bath which provides random kicks to the system. Particles are kicked every time step in a random direction with a randomly chosen magnitude (sampled uniformly, for speed) to guarantee that the system is kept at a target temperature. The second component is a damping term. This adds a force antiparallel to each particle's velocity to account for the solvent viscosity. The third component attempts to account for the energetic and entropic effects of the water on the proteins. This affects hydrophobic residues of the peptides. In a real system, hydrophobic residues are not attracted to water, where hydrophilic residues are. The result of this is that proteins attempt to bury their hydrophobic residues (this is known as the *hydrophobic effect*). This effect is entirely lost upon dropping explicit water, and so to account for it we increase the attractive interaction between hydrophobic residues.

Implicit solvent models are not as accurate as explicit models, but they become necessary for systems with an excess of solvent.

The additional force on particles under Langevin dynamics is

$$F_{Langevin} = -\zeta \dot{x} + \sqrt{2\zeta k_b T} R(t), \tag{2.13}$$

where ζ is the friction coefficient, and $R(t)$ is sampled from a distribution where $\langle R(t) \rangle = 0$ and $\langle R(t) R(t') \rangle = \delta(t - t')$.

2.4 Replica Exchange Molecular Dynamics

Replica exchange molecular dynamics (REMD) [61], also known as *parallel tempering* when employed with temperature swaps, is an enhanced sampling technique for MD simulation designed to more quickly sample rough free energy landscapes. We employ this method in the simulations of Chapter 3. The difficulty with typical molecular dynamics simulations is that at temperatures low compared to the landscape's free energy barriers, the system will become trapped in local minima, with the probability of crossing the barrier exponentially suppressed. If the temperature were higher than the barrier it would cross easily. The idea behind REMD is to run the system at multiple temperatures in parallel, and then to periodically allow these parallel replicas to swap temperatures. This way, a replica that is trapped in a local minimum at the desired temperature could suddenly find itself running at a higher temperature, cross the free energy barrier, and then settle back to the desired temperature again.

Of course the goal is to preserve the correct statistics of the averages of all observables. This is accomplished by correctly assigning the probability of a temperature swap, which means to enforce detailed balance. That is, the probability of performing a swap operation is proportional to the Boltzmann weight of the

new state over the old one:

$$w(X \to X')W(X) = w(X' \to X)W(X'), \tag{2.14}$$

where the argument X is the state (temperature, position list, momenta list) of *all replicas* ($X = \bigoplus_i \{(T_i, \mathbf{q}_i, \mathbf{p}_i)\}$), $w(A \to B)$ is the transition probability of swapping from state A to B, and $W(X)$ is the Boltzmann weight of state X. Since the replicas do not interact, the latter is the product of the Boltzmann weight of each replica:

$$W = \exp\left(\sum_i \beta_i H(\mathbf{q}_i, \mathbf{p}_i)\right). \tag{2.15}$$

Consider swapping two replicas, $m \leftrightarrow n$. This swap will be labeled as the transition from state $X \to X'$. Since all other replicas are unchanged, we can consider only m and n terms in Eq. 2.14.

First we will make the ansatz that we will need to rescale the momenta as follows:

$$\mathbf{p}_m \to \mathbf{p}'_n = \sqrt{\frac{T_m}{T_n}}\mathbf{p}_n \tag{2.16}$$

Thus, the ratio $w(X \to X')/w(X' \to X)$ can be determined:

$$w(X \to X')/w(X' \to X) \;=\; \frac{W(X')}{W(X)}$$

$$\begin{aligned} = \;& \exp\{-\beta_m H(\mathbf{q}_n, \mathbf{p}'_n) - \beta_n H(\mathbf{q}_m, \mathbf{p}'_m) \\ & +\beta_m H(\mathbf{q}_m, \mathbf{p}_m) + \beta_n H(\mathbf{q}_n, \mathbf{p}_n)\}. \end{aligned}$$

Note that the form of $W(X')$ is similar to $W(X)$, but with temperatures β_i swapped and $\mathbf{p}$ rescaled. Breaking energies into kinetic and potential terms:

$$\begin{aligned} &= \exp\{-\beta_m(K(\mathbf{p}'_n) + V(\mathbf{q}_n)) - \beta_n(K(\mathbf{p}'_m) + V(\mathbf{q}_m)) \\ &\quad +\beta_n(K(\mathbf{p}_m) + V(\mathbf{q}_m)) + \beta_m(K(\mathbf{p}_n) + V(\mathbf{q}_n))\} \\ &= \exp\{-\beta_m\left(\frac{T_m}{T_n}K(\mathbf{p}_n) + V(\mathbf{q}_n)\right) - \beta_n\left(\frac{T_n}{T_m}K(\mathbf{p}_m) + V(\mathbf{q}_m)\right) \\ &\quad +\beta_n(K(\mathbf{p}_m) + V(\mathbf{q}_m)) + \beta_m(K(\mathbf{p}_n) + V(\mathbf{q}_n))\}. \end{aligned}$$

Here we can see that our choice of momenta rescaling immediately cancels all kinetic energy terms:

$$= \exp\{-(\beta_n - \beta_m)(V(\mathbf{q}_m) - V(\mathbf{q}_n))\}.$$

Thus we can choose the following metropolis criterion to decide swap probabilities to satisfy detailed balance:

$$w(n \leftrightarrow m) = \begin{cases} 1 & \text{if } \Delta \leq 0 \\ \exp(-\Delta) & \text{otherwise} \end{cases} \tag{2.17}$$

where $\Delta = (\beta_n - \beta_m)(V(\mathbf{q}_m) - V(\mathbf{q}_n))$. This satisfies detailed balance, Eq. 2.14, and therefore guarantees that the correct Boltzmann statistics are sampled for each temperature. We stress, however, that because for a given temperature the swaps make the trajectory are discontinuous, kinetic information is lost. Only thermodynamic information is preserved.

Chapter 3

Thermodynamics of Peptide Aggregation on a Solid Surface

The formation of peptide aggregates mediated by an attractive surface is investigated using replica exchange molecular dynamics simulations (Chapter 2.4) with a coarse-grained peptide representation (Chapter 2.1). Replica exchange allows us to study the thermodynamics and equilibrium structures of the system at the cost of losing kinetic data.

A surface exposes proteins to selective pressures which alter the space of energetically-accessible conformations, possibly leading to the formation of misfolded, aggregation-prone protein conformations. Surface adsorption, both on biological membranes and on synthetic surfaces [51, 158–169], can increase the local concentration of proteins in such a way as to nucleate aggregation. Protein aggregation in the presence of biological membranes may have a toxic effect *in vivo* through the formation of oligomeric species that damage the cell membrane [11, 170, 171]. Understanding in a generic sense under which conditions certain types of aggregates may form is important for a better understanding of

aggregation-induced toxicity.

Surfaces play an important role in biomaterial-related aggregation processes [172, 173]. De-novo designed oligopeptides have been shown to assemble into a diverse set of nanostructures such as (i) fibrillar gels used as scaffolding for tissue engineering, (ii) nanotubes and nanovescicles with potential application as drug delivery agents, and (iii) assembled peptide monolayers interacting with surfaces [161, 174, 175]. Protein-surface interactions are important for integration of implanted devices or materials with biological tissues [176, 177], in assembly of protein-nanomaterial interfaces [178], and in fabrication of bio-nanostructures [179].

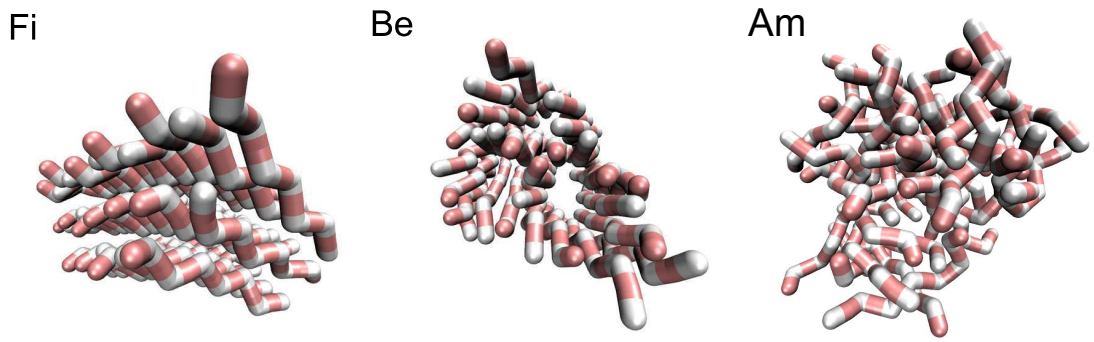

Figure 3.1: These are the main types of bulk aggregate structures: Fi) fibrils, Be) β-barrels, Am) amorphous aggregates. Generally, in the presence of a solid surface, we do not observe Fi and Be structures *in the bulk*, although we see some small, single-layered fibrils occasionally in the bulk near the binding transition temperature for our surface simulations with a strong surface attraction and stiff chiral dihedrals.

In this chapter, we use a coarse-grained computational model to probe the interaction of self-assembling amphiphilic peptides with a solid, uniformly attractive surface (Fig. 2.2). An earlier study focused on the self-assembly of this peptide model in the bulk (in other words, in the absence of an explicit surface) [57]. This

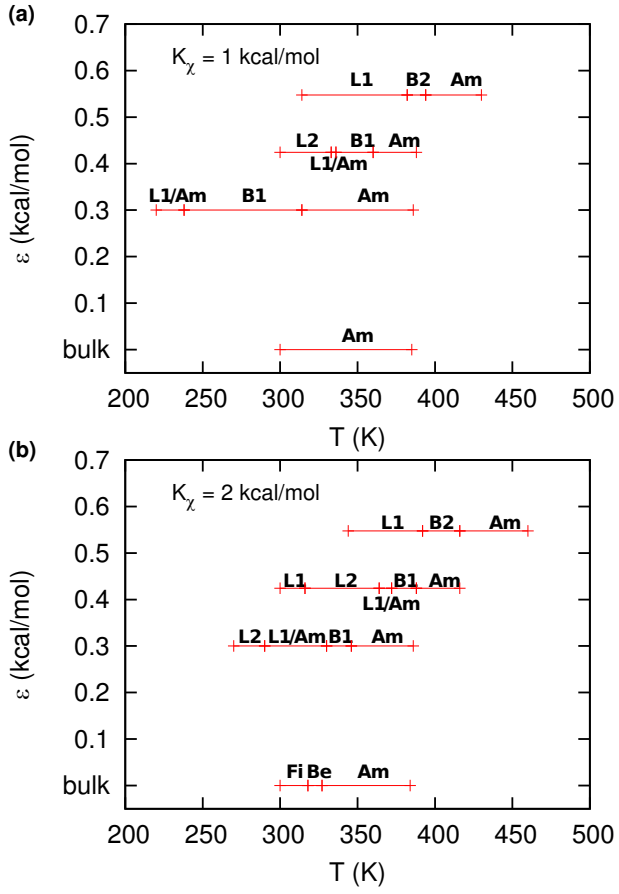

Figure 3.2: Phase plots showing dominant aggregate morphologies observed in equilibrium within simulated temperature ranges for each parameter set $\{\epsilon, K_\chi\}$. Fig. (a) is with $K_\chi = 1$ kcal/mol and (b) is with $K_\chi = 2$ kcal/mol. Regions outside of the lines are not sampled in our simulations. The data at the bottom of each panel are from a previous study [57] with no surface (*i.e.*, in the bulk) and are shown for comparison. The following abbreviations are used: L1) single layers on surface, L2) double layers on surface, L1/Am) single layers with attached amorphous aggregates, B1) binding phase: a coexistence state of amorphous aggregates in the bulk and single- or multi-layered aggregates on the surface, frequently with large amorphous aggregates attached to them, B2) alternate binding phase: a coexistence state of peptides scattered individually or part of small aggregates in the bulk and single-layered aggregates on the surface, Am) amorphous aggregates in bulk, Fi) fibrillar structures in bulk, and Be) β-barrel structures in bulk. Visualizations of these states are shown in Figs. 3.3 and 3.1.

work showed that chiral rigidity, or intrinsic β-sheet propensity of the peptides (as determined by the chiral dihedral parameter K_χ), played a significant role in determining aggregate morphology in the bulk. Results from these studies are summarized at the bottom of each panel in Fig. 3.2 and in Chapter 1.3. Chirally stiff peptides ($K_\chi = 2$ kcal/mol, see Chapter 2.1) form twisted, multi-layered fibrillar aggregates (Fi) up to temperatures of approximately 318K, then β-barrel-like structures (Be) up to 327K, and finally amorphous aggregates (Am) above 327K [57]. Images for these morphologies are shown in Fig. 3.1. In the case of chirally flexible peptides ($K_\chi = 1$ kcal/mol), on the other hand, bulk aggregates reside in an amorphous state at all temperatures sampled.

3.1 Methods

Refer to Chapter 2.1 for the general description of the peptide and surface model. Each system, or parameter set $\{\epsilon, K_\chi\}$, was simulated using replica exchange molecular dynamics ([61] and Chapter 2.4) with 30 replicas at varying temperature. Each simulation was run for 225ns total with each temperature undergoing 3000 replica swaps occurring every 75ps. For each system, a temperature range was chosen such that the surface binding transition occurred in the middle of the range. While replica exchange simulations do not provide information on kinetic mechanisms of aggregation, they do determine the thermal average behavior of the system. It should be emphasized that all observations are of equilibrium structures as a function of temperature, not of time.

Six different Hamiltonians were considered in our simulations, using three different strengths of surface attraction ($\epsilon = 0.30$, 0.42 and 0.55 kcal/mol), and two values of the chiral dihedral stiffness parameter ($K_\chi = 1$ and 2 kcal/mol). For

each simulation, fifty peptides were placed in a simulation box in a randomized initial configuration. The box had dimensions $L_x = L_y = 200$Å and $L_z = 50$Å. We used periodic boundary conditions in the x and y directions. In the z direction, the surface, covering the bottom of the box, prevented the peptides from crossing the lower boundary, and a ceiling potential (see Chapter 2.1) pushed peptides whose height exceeded 50Å back into the box so that the effective z dimension was $L_z = 50$Å. Thus peptides could not cross the top boundary and interact with the reverse side of the surface.

3.1.1 Order Parameters

We studied the behavior of several order parameters as a function of temperature for varying chiral stiffness (K_χ) and surface attraction (ϵ). After the system had sufficiently equilibrated, we computed each order parameter on the last frame of every 75ps replica swap. The value of an order parameter at a given temperature is the mean of all computed order parameters at that temperature.

The mean peptide height (z_{av}) is the average height of the peptides' hydrophobic residues above the plane of the surface. This parameter quantifies the association/dissociation of the peptides from the surface. When peptides are fully bound to the surface, the mean height is at a minimum value of $z_{\text{av}} = 2$Å and in the fully unbound state, the mean height becomes $z_{\text{av}} = 25$Å, which is half the vertical dimension of the simulation box. The mean peptide height is the order parameter used to define the transition temperature of the system: the temperature where average height increases most steeply with temperature. Another order parameter measuring the degree of surface binding is the number of peptides bound to the surface (N_B). This counts the number of peptides whose three

hydrophobic interaction centers have an average height within 5Å of the surface and a standard deviation less than 1.5Å.

We also look at three structural order parameters which are useful in characterizing the structure of aggregated peptides in the bulk [57]. The number of contacts (C_1) counts the contacts between backbones of adjacent peptides. A contact is counted between X interaction centers (Fig. 2.2) in the backbones if the nearest neighbor X-X distance is less than 3.5Å. The orientational order parameter (Q) measures the degree of alignment between peptides. It equals 1 when all peptides are parallel (or antiparallel) and goes to 0 when their orientations are uncorrelated. It is defined as the largest eigenvalue of the 3×3 matrix:

$$Q_{\alpha\beta} = \frac{1}{2N} \sum_{i=1}^{N} (3u_{\alpha}^{(i)} u_{\beta}^{(i)} - \delta_{\alpha\beta}), \tag{3.1}$$

where the sum is over all peptides, $\alpha, \beta = x, y, z$, and the vector $\mathbf{u}$ is the normalized vector from the first to last X interaction center along the backbone. This order parameter has been used previously in the literature [57, 110, 180].

The final structural order parameter computed is the connectivity (N_{C_1}) which counts the number of fibrillar aggregates, where two adjacent peptides are part of the same aggregate if all of their X backbone interaction centers form a contact as determined by C_1. N_{C_1} takes on a high value of 50 (the number of peptides in the system) when peptides do not aggregate or aggregate amorphously, and a minimum value of 1 when all peptides are part of a single fibrillar aggregate.

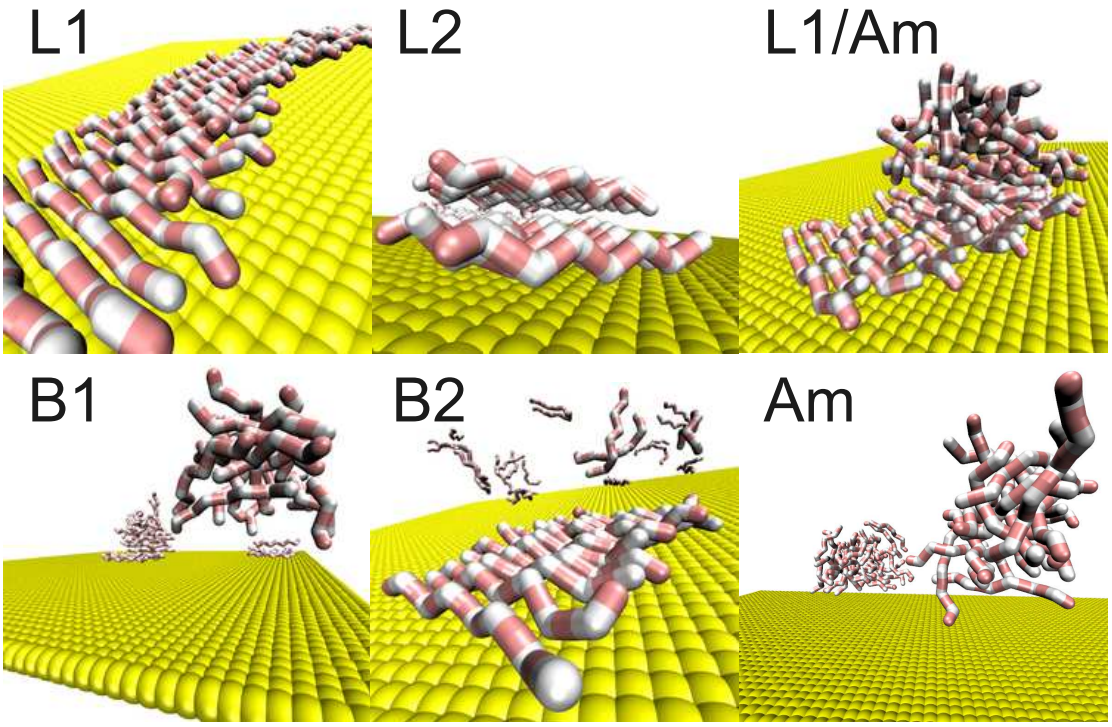

Figure 3.3: A visualization of the most common equilibrium phases observed in our simulations. The following abbreviations are used: L1) single layers on surface, L2) double layers on surface, L1/Am) single layers with attached amorphous aggregates, B1) binding phase: a coexistence state of amorphous aggregates in the bulk and single- or multi-layered aggregates on the surface, frequently with large amorphous aggregates attached to them, B2) alternate binding phase: a coexistence state of peptides scattered individually or part of small aggregates in the bulk and single-layered aggregates on the surface, and Am) amorphous aggregates in bulk. The binding phase states B1 and B2 differ by the presence of amorphous aggregates observed and the existence of multi-layered aggregates in type B1 but not type B2.

3.2 Results

3.2.1 Peptides adopt different aggregate structures in the bulk than on surfaces

We find that peptide aggregation in the presence of an attractive solid surface leads to formation of aggregate structures that differ from those observed for bulk aggregation. These results are summarized in Fig. 3.2, which shows dominant aggregate morphologies populated in equilibrium as a function of temperature for all parameter sets simulated. Remarkably, at temperatures where aggregates are bound to the surface, the temperature progression of dominant structures observed is dictated solely by the strength of the surface attraction.

As we lower the temperature, equilibrium states switch from aggregates in the bulk to aggregates bound to the surface. With the strong surface attraction, for either chiral stiffness, this phase transition from unbound to bound states involves the fewest types of aggregate structures. Just below the temperatures where bulk and bound states coexist, peptides are maximally bound to the surface as a single-layered fibril. Just above these temperatures, they aggregate solely in the bulk without binding to the surface. The binding phase is a coexistence of the states above and below, except that peptides in the bulk do not significantly aggregate. This type of binding phase, seen only for the strong surface attraction, is denoted B2 (see Fig. 3.3). Peptides stay bound to the surface until temperatures are sufficiently high that surface-preferred fibrillar states lose to amorphous aggregates which are far easier to form in the bulk. This transition happens very quickly with temperature.

The transitions for medium and weak surface attractions involve more types

of aggregate structures than for the strong surface attraction. They include residuals of amorphous aggregates below the binding phase in the form of the L1/Am phase (see Fig. 3.3). Also, fibrillar structures at temperatures immediately below the binding phase are not all single layers: there is a significant presence of double layers as well. This type of binding phase, seen only for the weak/medium surface attractions, is denoted B1 (see Fig. 3.3). The most striking difference between weak/medium surface attractions and the strong surface attraction is the existence of amorphous aggregates in the binding phase of the former but not the latter.

The progression of dominant aggregate morphologies with temperature does not depend on the chiral stiffness parameter, unlike in the bulk. As seen from Fig. 3.2, the structure progression as temperature is lowered for $\epsilon = 0.55$ kcal/mol is Am, B2, L1; the equivalent progression for $\epsilon = 0.30$ or 0.42 kcal/mol is Am, B1, L1/Am, L2, L1. These progressions are *qualitatively* independent of K_χ. However, the transition temperatures between different phases of the progression are K_χ-dependent, with transitions occurring at higher temperatures for stiffer chiral dihedral potentials.

While the temperature progression of dominant aggregate morphologies is the same for either chiral dihedral stiffness, there are differences in *rarer* structures observed, although only with weak surface attraction. In this case, for rigid (but not flexible) chiral stiffness, we occasionally see small fibrillar aggregates in the bulk near the binding phase. This is to be expected since we know from bulk simulations that at this temperature some fibrils are present. We do not observe this difference between $K_\chi = 1$ and 2 kcal/mol at higher surface attractions because their binding phases occur at higher temperatures where bulk simulations confirm that only amorphous aggregation occurs.

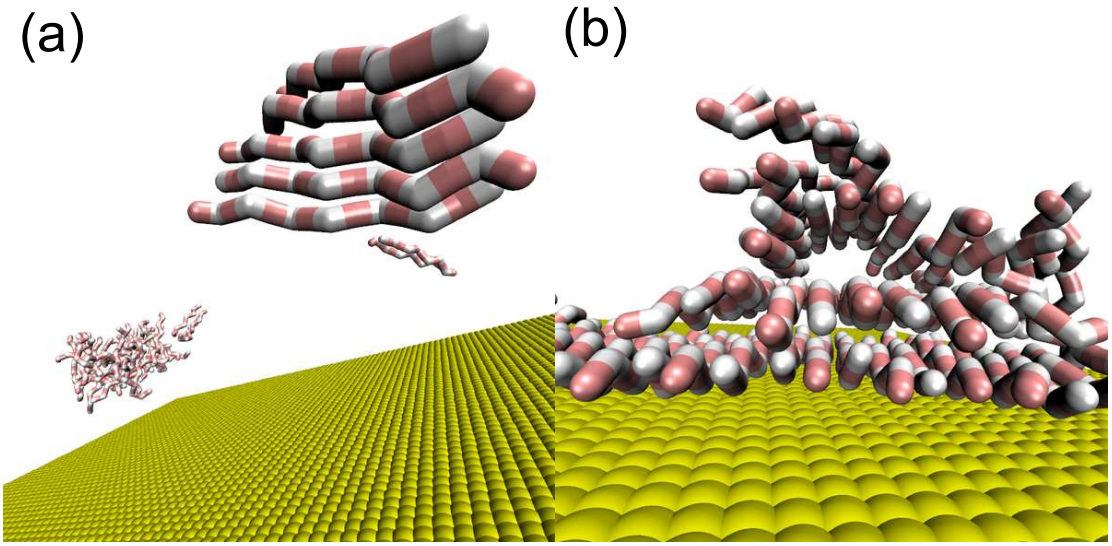

Figure 3.4: Shows some of the less common (non-dominant) structures observed. Near the binding transition temperature, we occasionally see small fibrils in the bulk (a) for stiff dihedrals and weak surface attraction. For the same parameters, we rarely observe what is nearly a triple-layered aggregate, whose third layer is malformed (b). This is the closest observed structure to a triple-layered aggregate and also the closest to a β-barrel.

We do not observe any triple-layered fibrils in any of our simulations. While in the bulk, peptides where $K_\chi = 2$ kcal/mol would form triple-layered fibrils (L3) within the range of approximately 300-310K, surface attraction strongly favors single or double layers over triple layers. In some cases, we see structures that are similar to triple layers but they have the property that the third layer is malformed into a partial β-barrel (Fig. 3.4 (b)). These structures are observed infrequently in the L2 or L1/Am phases of $K_\chi = 2$ kcal/mol (but not observed for 1 kcal/mol) with weak or medium surface attractions. They are the closest structures observed to β-barrels in our simulations. The strong surface attraction is too strong to permit a double-layered phase, so these near-L3 structures are not observed in this case. The system energetically favors single- or double-layered fibrils to maximize

contact with the surface. While we do see certain rare fibrillar structures with rigid dihedrals that are not observed with flexible ones, progressions of *dominant* aggregate morphologies are identical.

The fibrillar structures observed on the surface are not entirely the same as those observed in previous work in the bulk. In bulk simulations, the fibrillar aggregates twisted along their length (along an axis perpendicular to the peptides themselves) [57]. This effect, induced by the peptides' chirality, is not seen on the surface, which presses the fibrils flat against itself.

3.2.2 Binding transition sharpened by surface attraction and chiral stiffness

Features of binding transition captured by a single order parameter

The mean height of the peptides above the surface (z_{av}) quantifies their degree of binding to the surface. Indeed, as the system is cooled, the average height undergoes a transition from being unbound from the surface to a bound state (see Fig. 3.5 (a)).

For flexible peptides, the transition with a low surface attraction ($\epsilon = 0.30$ kcal/mol) is not as sharply defined. However, increasing either surface attraction or chiral dihedral stiffness leads to a considerably sharper transition. Sharper transitions correspond to a more clearly-defined sigmoidal shape, which is indicative of a more cooperative transition. In earlier work, we found that increasing chiral dihedral stiffness increases the propensity to form ordered β-sheet structures [57]. These fit more naturally on a flat surface than a disordered structure would and, as a result, peptides with a higher β-sheet propensity parameter will remain bound to the surface at higher temperatures and consequently their transi-

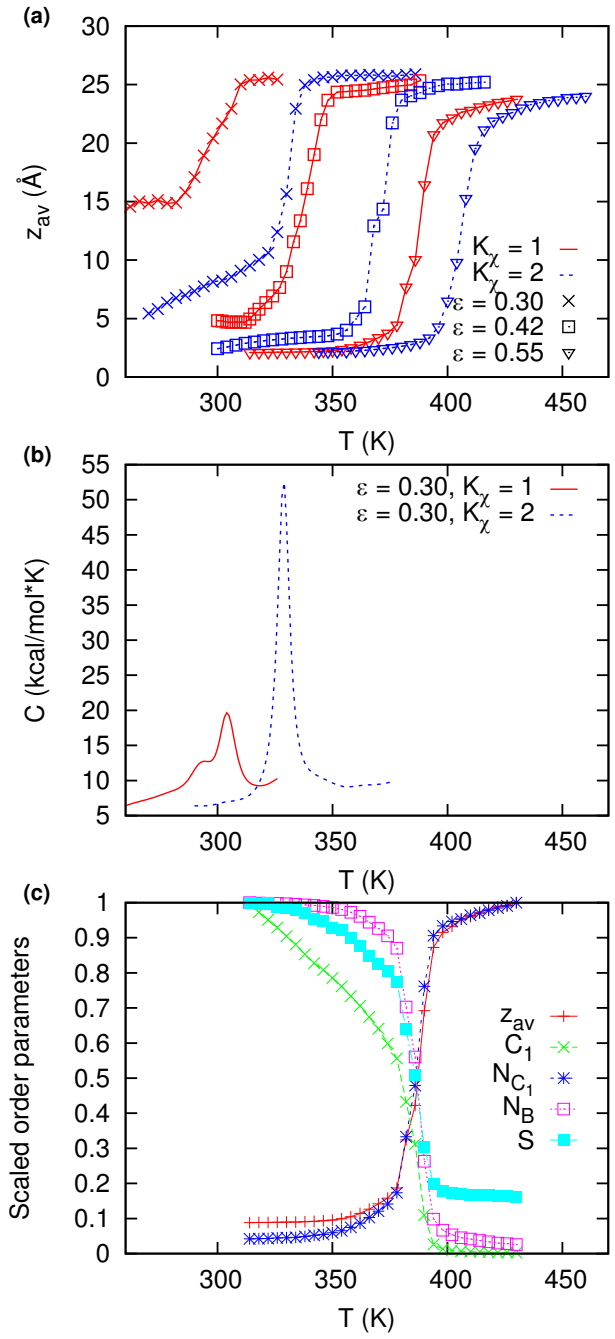

Figure 3.5: Fig. (a): transition of the average height order parameter, $z_{\rm av}$. Units of ϵ and K_χ are kcal/mol Fig. (b): shows the heat capacity for two simulations with the weak surface attraction ($\epsilon = 0.30$ kcal/mol). Only two sets of parameters are compared for clarity. Fig. (c): the transition is shown in various order parameters (described in Section 3.1.1) normalized to their maximum value. This simulation is for $\epsilon = 0.55$ kcal/mol and $K_\chi = 1$ kcal/mol, but all other values of the parameters showed similar behavior.

tion temperatures are higher. Likewise, peptides with a higher surface attraction have a higher binding transition temperature and a sharper transition. Of the six data sets in Fig. 3.5 (a), the two rightmost (with strongly attractive surfaces) are sharpest and fall very rapidly from the maximum z_{av} value into the phase bound to the surface as temperature is decreased. These correspond to the type B2 binding phase, where coexistence of free and surface-bound aggregates occurs without the presence of amorphous or multi-layered aggregates on the surface. The maximum slopes of the remaining data sets, the four left-most in Fig. 3.5 (a), are not as steep. More importantly, these curves are not as perfectly sigmoidal and do not drop directly to the 2Å minimum of the ideal single layer phase below the transition. This tail corresponds to intermediate phases where amorphous aggregates exist on top of a layer (Fig. 3.3 L1/Am) and the formation of double layers (Fig. 3.3 L2). Thus the mean height order parameter plots capture the structural complexity of the transitions (compare Figs. 3.5 (a) and 3.2).

The transition also shows identical behavior for seemingly unrelated order parameters: structural order parameters measuring the degree of order in the aggregates, and binding order parameters measuring the degree to which peptides are bound to the surface. All of these parameters give analogous forms for the transitions. Fig. 3.5 (c) plots the transition for one simulation projected onto all order parameters suitably normalized.

Analogous behavior of different order parameters is indicative of a cooperative transition. The surface binding-unbinding transition happens at the same temperature and with the same features as the order-disorder transition. Structural order of the system is completely governed by its attraction to the surface.

The features of the transition are also seen from a plot of the heat capacity (Fig. 3.5 (b)). There is a sudden rise in heat capacity centered at the point of

steepest ascent in plots of the order parameter z_{av} *vs.* T (Fig. 3.5 (a)). The width of the heat capacity spike corresponds to the width in the jump of the mean height order parameter, and narrower heat capacity spikes correspond to sharper transitions in Fig. 3.5 (a). Thus sharpness of the peak is indicative of the level of cooperativity in the transition from bulk amorphous aggregates to a state with aggregates bound to the surface. Fig. 3.5 (b) shows that for a given surface attraction, the chiral stiffness sharpens the transition.

Chiral Stiffness Shifts Transition Temperatures

The transition temperatures, at least for the five sharp transitions (all except $\epsilon = 0.30$ kcal/mol, $K_\chi = 1$ kcal/mol), seem to increase linearly as a function of surface attraction (Fig. 3.6). Interestingly, a substantial tuning of chiral dihedral stiffness appears to have a negligible effect on the slope of this line. Our results indicate that increasing chiral stiffness from 1 to 2 kcal/mol has the same effect on the transition temperature as increasing the surface attraction by 0.08 kcal/mol, as seen in Fig. 3.7. We use a number of methods to characterize the location of the transition: the midpoint of the steepest ascent of the order parameter (Fig. 3.5 (a)), the halfway point where the mean peptide height reaches half its maximum value, and points of critical behavior in the free energy as a function of temperature. As the transition becomes more cooperative, these different methods of identifying the transition temperature converge to the same value.

Low Free Energy Barrier at Transition Temperature

The nature of the transition from bound to unbound aggregates is highly dependent on surface attraction and chiral stiffness. Previous work in bulk aggregation [57] showed that the transition was a weak first order transition with two states

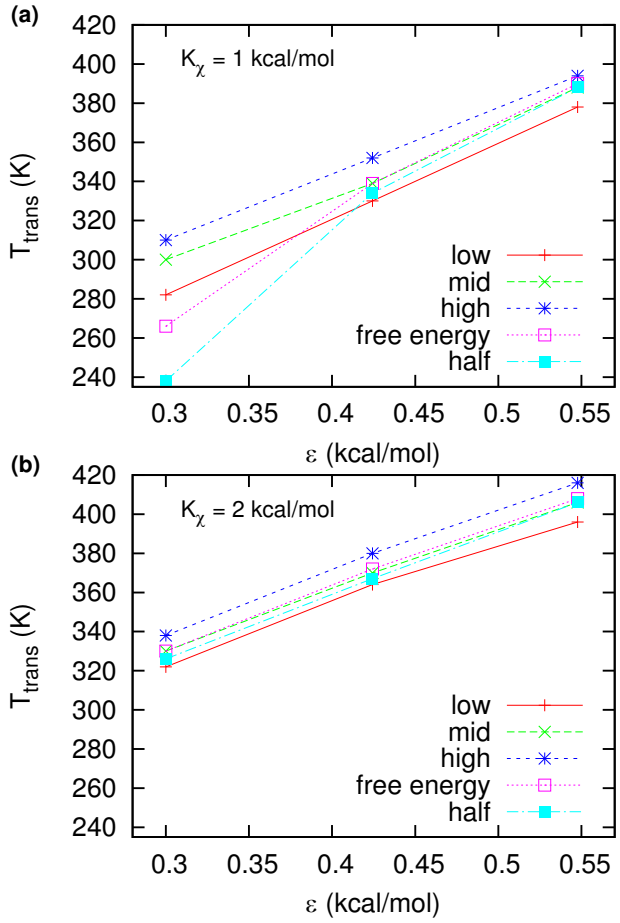

Figure 3.6: A summary of the binding transition temperatures for all parameter sets. Fig. (a) is for $K_\chi = 1$ kcal/mol and Fig. (b) is for $K_\chi = 2$ kcal/mol. Both plots have the same scale. The "low", "mid" and "high" transition temperatures are judged from the bottom, middle and top of the regions of steepest slope in Fig. 3.5 (a). These give an idea of the range over which the most rapid transition is taking place. The "free energy" transition is judged from plots of the free energy, see Fig. 3.8. The "half" transition temperature occurs when the average height is $z_{\rm av} = 12.5$Å, precisely halfway to its maximum averaged value.

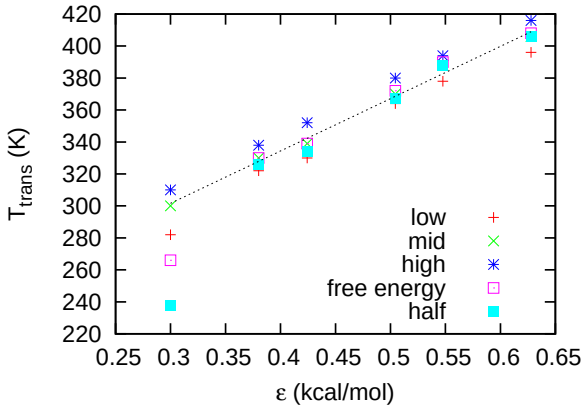

Figure 3.7: Shows the binding transition temperatures for varying surface attraction. This plot combines data from Figs. 3.6 A and B, assuming that increasing K_χ from 1 to 2 kcal/mol is equivalent to raising ϵ by 0.08 kcal/mol.

separated by a 1 kcal/mol barrier. We also observe this transition with the surface with the parameters $\epsilon = 0.42$ kcal/mol and $K_\chi = 2$ kcal/mol (Fig. 3.8 (a)). However, for the majority of binding transitions we observe that the state is highly sensitive to temperature and jumps from one state to another, but not via a clear first order transition, since at the transition the barrier flattens between the two states (Fig. 3.8 (b)).

3.2.3 Isolating Interactions Highlights Aggregation/Binding Cooperativity

The effects of peptides' polymer nature can be isolated from their inter-peptide interactions by removing all interactions between one peptide and another. These "noninteracting" peptides have a transition that is substantially softer than the transition for interacting peptides, which demonstrates the degree of cooperativity between aggregation forces and surface attraction to affect the binding transition. A comparison between the transitions of the interacting and noninteracting pep-

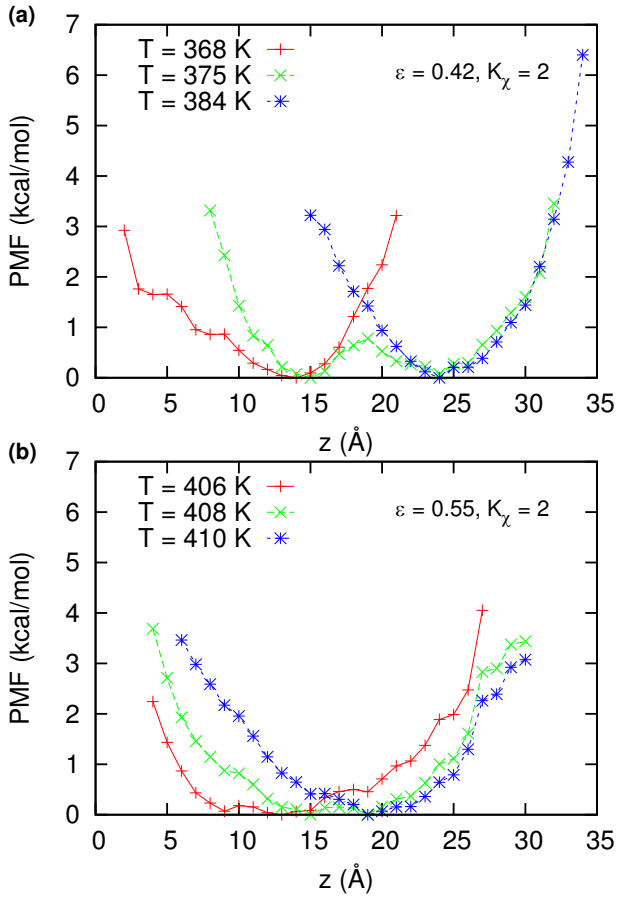

Figure 3.8: Plot of the free energy across the transition. The middle profile is at the transition temperature. Units of ϵ and K_χ are kcal/mol, suppressed in the plots for neatness. The parameters used are (a) $\epsilon = 0.42$ kcal/mol and $K_\chi = 2$ kcal/mol and (b) $\epsilon = 0.55$ kcal/mol and $K_\chi = 2$ kcal/mol.

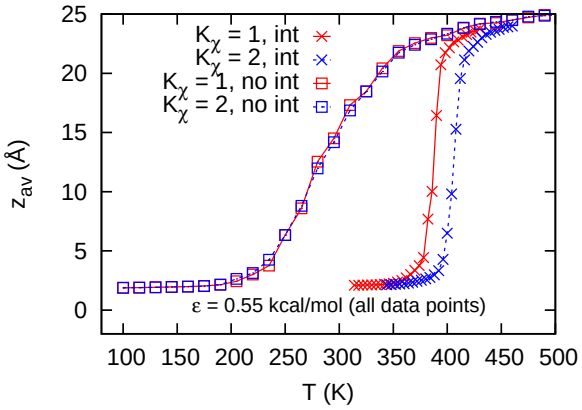

Figure 3.9: Transition of the average height order parameter, with data for the model with full peptide-peptide interactions ("int") and a simplified model with peptide-peptide interactions removed ("no int"). Units of K_χ are kcal/mol, suppressed in the plot for neatness. These simulations have a surface attraction of $\epsilon = 0.55$ kcal/mol.

tides is shown in Fig. 3.9. Tuning chiral stiffness has no effect on the transition of noninteracting peptides, which indicates that the increase of the transition temperature with the chiral stability of the interacting peptides comes entirely from its cooperative effect with peptide-peptide interactions in stabilizing ordered fibrillar structures. Therefore, binding of the aggregates to the surface is the cooperative result of surface attraction, the β-sheet propensity parameter K_χ and peptide-peptide interactions.

The peptide-surface model can be simplified to zeroth order by considering a model where the only interaction is between a peptide interaction center and a surface. While this is clearly a coarser model than even noninteracting peptides, and definitely a coarser model than fully interacting peptides, we feel that it is illuminating to compare a peptide surface-model to its most coarse-grained form. This simplest model for the attraction of peptides to the surface has a Boltzmann distribution of peptide heights given by a Lennard-Jones attraction of peptides

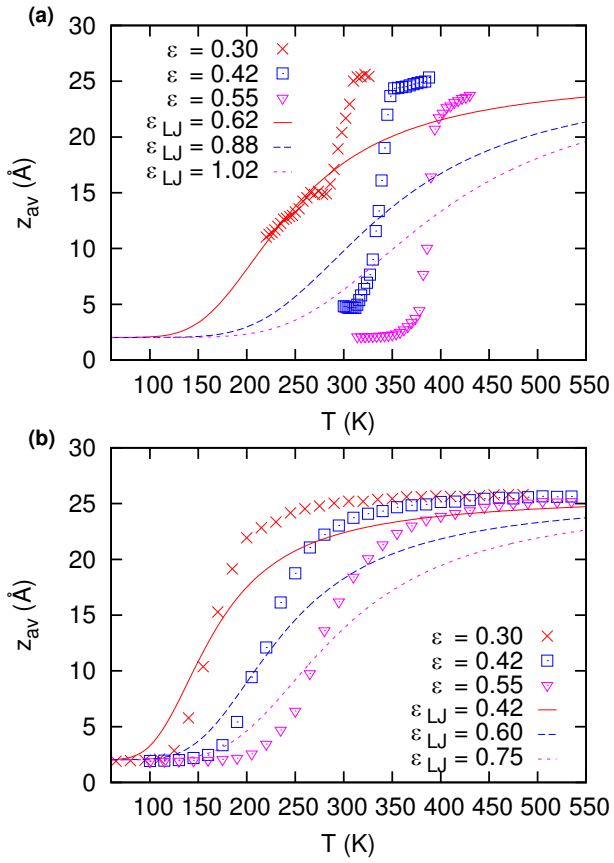

Figure 3.10: Plots of the transition in the peptide mean height order parameter, z_{av}. Units of ϵ and ϵ_{LJ} are kcal/mol, suppressed in the plots for neatness. Fig. (a) fits simulation results (data points, also in Fig. 3.5 (a)) for $K_\chi = 1$ kcal/mol with the zeroth order approximation of a peptide-surface interaction (solid or dashed curves): a Lennard-Jones surface density interacting with a peptide interaction center. The zeroth order fit chooses a value of ϵ_{LJ} such that they cross at the halfway point of the transition (see Section 3.2.2). Fig. (b) fits the equivalent zeroth order approximation to simplified results of noninteracting peptide simulations (where all peptide-peptide interactions are removed).

to the surface, with a probability density $p(z) \propto \exp(-U_0(z)/k_bT)$. If we coarse-grain the surface to a surface density κ of Lennard-Jones particles, the potential as a function of height becomes:

$$U_0(z) = 4\pi\epsilon_{\mathrm{LJ}}\kappa\sigma^2\left(\frac{1}{5}\left(\frac{\sigma}{z}\right)^{10} - \frac{1}{2}\left(\frac{\sigma}{z}\right)^{4}\right), \tag{3.2}$$

where ϵ_{LJ} and σ are the Lennard-Jones well depth and range before coarse-graining. Using $\sigma = 2$Å as in our simulations (so that the limit of z_{av} as $T \to 0$ is correct), we can get a theoretical prediction for mean peptide height *vs.* temperature for this zeroth order peptide-surface model shown in Fig. 3.10. An important point is that although the noninteracting peptide model is much more finely detailed than this zeroth order model, this detail does not add any qualitative features to the transition. The zeroth order model yields only a slightly softer transition than noninteracting peptides (see Fig. 3.10 (b)), and the two models share these features: the transition becomes softer with increasing surface attraction and the z_{av} *vs.* T curves are purely sigmoidal. However, the transitions with peptide-peptide interactions present (Fig. 3.10 (a)) are very poorly fit by the zeroth order model. The simplified model yields curves dramatically softer that do not capture the non-sigmoidal behavior or increasing sharpness with surface attraction that are key features of the fully interacting model. So noninteracting peptides are relatively well modeled by a trivial Boltzmann distribution of peptide heights, but fully interacting peptides are not. This emphasizes the fact that the transition only becomes nontrivial when we include all interactions in the model (especially many-body effects): structural detail from the chiral stiffness parameter K_χ, aggregation through peptide-peptide interactions and surface attraction.

A simple argument shows that in the idealized noninteracting particle case, the transition temperature will increase linearly with ϵ, as suggested by Fig. 3.7. The transition occurs at a z_{av} value roughly halfway between the surface and the upper boundary. So the transition temperature is the solution to

$$z_{\mathrm{av}} = 12.5\text{Å} = \int_0^{25\text{Å}} dz\ z\ p\left(V_{\mathrm{ni}}(z; \epsilon_{\mathrm{LJ}/k_bT})\right), \tag{3.3}$$

where $p\left(V_{\mathrm{ni}}(z; \epsilon_{\mathrm{LJ}}/k_bT)\right)$ is the probability density of z which is a functional of $\epsilon_{\mathrm{LJ}}/k_bT$ in the Boltzmann distribution. The solutions to this equation have $\epsilon_{\mathrm{LJ}} \propto T_{\mathrm{trans}}$. The difference in the non-idealized case is that ϵ *vs.* T_{trans} is linear with a nonzero constant term rather than proportional. This nonzero constant term suggests interactions other than only surface-peptide attraction affect the transition temperature, but only by a constant shift (*cf.* the shift seen between Fig. 3.6 (a) and (b)). Here we are assuming that T is small enough that $\langle z_{av} \rangle$ above 25Å becomes negligibly populated at the transition temperature. We found this assumption to be valid for all Hamiltonians we considered.

3.3 Summary and Discussion

We find that the addition of a surface to the computational model of peptide aggregation in the bulk [57] has considerable qualitative and quantitative effects on the transition from disordered to ordered structures as the system is cooled. The rich diversity of structures observed in bulk aggregation is lost with the addition of the surface, which strongly favors ordered fibrillar aggregates close to the surface. Multi-layered aggregates observed in the bulk are limited to two layers after equilibration on the surface, and β-barrel structures in the bulk are lost.

Also, chiral dihedral stiffness ceases to have a qualitative effect on the progression of dominant morphologies observed through the transition. Instead, only the strength of the surface attraction affects which dominant structures are observed across the disorder to order transition, which coincides with the peptide binding transition to the surface.

The nature of the binding transition is strongly dependent on the peptides' attraction to the surface. To analyze the binding transition, we monitored equilibrium structures at varying temperature. For strong surface attraction at either value of chiral stiffness, we observe that the binding transition occurs with a coexistence of unaggregated peptides in the bulk and single-layered aggregates on the surface. However, for weak and medium levels of surface attraction there is a significant degree of amorphous aggregation both in the bulk and attached to surface-bound fibrils. In addition, we see double layers bound to the surface as well as single layers, unlike for strong surface attraction.

Quantitatively, chiral dihedral stiffness acts cooperatively with surface attraction to affect the transition temperature and transition sharpness, shifting transition temperatures to higher values as chiral dihedral stiffness increases. This occurs because increasing chiral dihedral stiffness leads to increased population of extended β-structured conformations. These include fibrillar conformations [6, 111] that are preferred by the surface since they maximize surface-aggregate contact.

Fig. 3.5 (c) shows that transitions defined by the following order parameters are equivalent: surface binding based order parameters, such as the mean height, and order parameters based purely on the aggregates' structural order, such as the orientational parameter. This equivalence occurs since the structural order of the peptides is dictated by surface interactions acting cooperatively with the

chiral stiffness shown to govern structural order in the bulk [57].

Isolating the effects of various interactions confirms that the binding phase transition results from cooperativity of β-sheet propensity, surface attraction and peptide-peptide interactions. We were able to model statistics of the binding of a *single* peptide as a point particle in a potential depending only on its mean height above the surface with good qualitative accuracy. However, this simplification could not model aggregation of *many* interacting peptides on the surface, which stresses the cooperative interaction of peptide-peptide forces with surface attraction. Thus peptide aggregation couples to its surface attraction in a nontrivial way.

We find that the presence of the surface heightens propensity for fibrillar aggregate formation by coupling the peptides' natural β-sheet propensity to their surface attraction. Fibrillar aggregates form on the surface at high temperatures where they form only amorphous aggregates in the bulk. As an example, toxic species in aggregation diseases could consist of a number of aggregate structures ranging from small soluble oligomers to mature fibrils [12]. Our simulations show that surfaces can alter aggregate morphology, and in this respect hint that surfaces could either induce or prevent formation of a toxic species. Understanding the nature of aggregation in the presence of surfaces is a crucial step to understanding how proteins aggregate *in vivo*.

Chapter 4

Kinetics of Peptide Aggregation on a Solid Surface

Mechanisms of peptide aggregation on hydrophobic surfaces are explored using molecular dynamics simulations with a coarse-grained peptide representation. Systems of peptides are studied with varying degrees of backbone rigidity (a measure of β-sheet propensity) and degrees of attraction between their hydrophobic residues and the surface.

We showed in Chapter 3 that the equilibrated aggregate structures forming in the bulk differed from the structures that aggregate on the surface. The aggregates underwent a clear binding transition: switching from a state bound to the surface at low temperatures to a state free in bulk solution at higher temperatures. Near the transition temperature, the system had a coexistence phase, or *binding phase*, of surface-bound and unbound peptides. By adding the surface, there emerged two distinct classes of binding phases as a function of temperature. With a strong surface attraction, the binding phase involved fewer morphologies; for medium and weak surface attractions, the binding phase involved more inter-

mediary structures, such as double-layered aggregates, and amorphous aggregates attached to single-layers. While chiral stiffness increased the binding transition temperature and sharpness, it did not affect the ordered *sequence* of equilibrium structural phases observed by varying the temperature, although it did affect at what temperatures these transitions occurred.

Here, we compare this work in particular to the thermodynamic calculations of Chapter 3, where we studied the binding and aggregation transitions observed by lowering temperature. The sequence of dominant morphologies of these transitions are found in Fig. 3.2. Images of the various morphologies along with their abbreviations are found in Figs. 3.3 and 3.1. In this chapter, rather than analyzing structures accessible to the system in thermodynamic equilibrium, we study the mechanisms and pathways of the peptides' initial binding to the surface. This enables us to contrast aggregate formation and growth in the bulk with formation and growth mediated by the surface. It reveals how the aggregation is initiated kinetically, and by what mechanisms the aggregates approach their final equilibrated structures.

4.1 Methods

4.1.1 Order Parameters

We calculate several order parameters in this chapter. The mean peptide height (z_{av}) measures the average height of the peptides' three hydrophobic residues above the surface. The orientation (Q) is a measure of peptide alignment, equaling 1 when all peptides are in a parallel (or anti-parallel) alignment, and equaling 0 when their orientations are uncorrelated. The equation to describe Q is Eq. 3.1 and

it is discussed in the literature [110, 180]. The number of aggregates (N_A) measures the degree of aggregation by counting distinct aggregates. With our definition, a lone peptide is counted as a single aggregate, so the number of aggregates has a maximum value of the number of peptides in the system, and a minimum of 1 when the peptides are fully aggregated. Finally, the mixing parameter ($C_{1,2}$) evaluates whether the X interaction centers of adjacent peptides are all within 3.5Å of each other, and counts the number of such adjacencies where the two neighboring peptides are of different types (in this case, a seed peptide and a free peptide). It measures to what degree peptides of the two types mix with each other in a fibril.

4.1.2 Simulations

Three types of simulations were conducted. The main type analyzed (see all of Section 4.2 except for 4.2.1 and 4.2.4) initialized 50 peptides in a dispersed random initial configuration above the surface in a $20 \times 20 \times 5$ nm^3 box, the z dimension enforced by a ceiling potential and the surface. For each parameter set and temperature studied, 120 parallel simulations were conducted at random initial configurations. The simulation time was 180ns, which was sufficient to observe the metastable states of the initial kinetics.

The simulations were conducted at temperatures corresponding to either the "low" or "mid" point of the mean peptide height *vs.* temperature transition, whose plot is an increasing sigmoidal curve (Fig. 3.5 (a)). The "low" point of the transition is at the point below the transition temperature where the sigmoidal curve changes from being flat to a steep ascent, and the "mid" point of the transition is the temperature where the slope of mean height *vs.* temperature

is steepest. We are mainly concerned with kinetics below the transition temperature, as the results are more stable with temperature and can be said to represent the kinetics of aggregation at temperatures where the peptides bind to the surface in equilibrium, but at temperatures high enough that we see a variety of aggregate structures.

Six different parameter sets were studied, with the surface attraction varying from weak to strong ($\epsilon = 0.30$, 0.42, or 0.55 kcal/mol) and the chiral dihedral stiffness varying between flexible and rigid ($K_\chi = 1$ or 2 kcal/mol). The temperature was controlled by a Langevin thermostat. The temperatures simulated below the transition temperature for the flexible dihedrals were 282K, 330K, and 378K, respectively, for the weak, medium, and strong surface attractions. For the rigid dihedrals, the temperatures simulated were 322K, 364K, and 396K. At the midpoint in the transition, the temperatures for the flexible dihedrals were 300K, 339K, and 388K; the temperatures for the rigid dihedrals were 330K, 370K, and 406K.

The second type of simulation was a seeding simulation (Section 4.2.1). Here we used parameters such that only single-layered fibrillar aggregates could form: $\epsilon = 0.55$ kcal/mol, $K_\chi = 1$ kcal/mol, and $T = 378$K; and $\epsilon = 0.55$ kcal/mol, $K_\chi = 2$ kcal/mol, and $T = 378$K. Of the 50 peptides in the system, 15 were initialized as a single-layered fibril (the *seed peptides*) on the surface and the remainder were randomly distributed in the bulk (the *free peptides*). The intent of these simulations was to study how the free peptides mix with a fibrillar seed. We conducted 64 parallel simulations for each parameter set, each for 180ns. The simulation box was the same as our other simulations.

The third type of simulation was a diffusion simulation (Section 4.2.4), and it initialized all peptides as a single-layered fibril on the surface. This simulation

was conducted for fibrils 10, 20, 30, 40, and 50 peptides long. The parameters used were $\epsilon = 0.42$ kcal/mol, $K_\chi = 1$ kcal/mol, and $T = 300$K. We conducted 200 parallel 180ns simulations for each system size. The simulation box was the same as our other simulations.

4.2 Results

4.2.1 Formation of a Single Layer

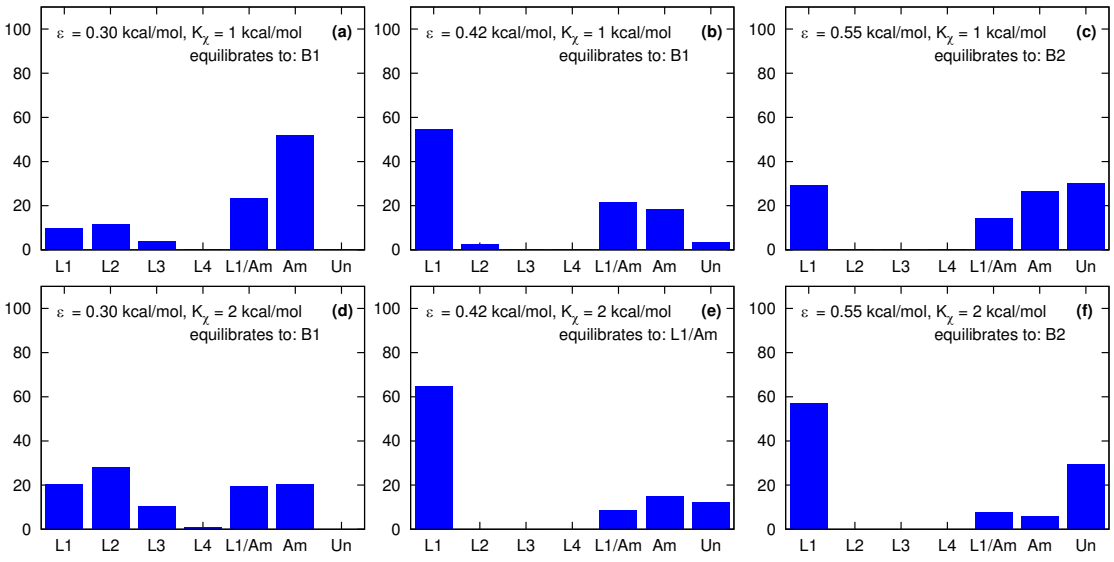

Figure 4.1: Percentage distribution of structures found at the surface binding transition temperature. Representative of the morphologies present at the end of 120 parallel 180ns simulations for varying surface attraction (ϵ) and chiral stiffness (K_χ). They are weighted by the number of peptides involved in each aggregate structure. Aggregate phases counted in the graph are: surface-bound single- to quadruple-layered fibrils (L1-L4), surface-bound layered fibrils with attached amorphous aggregates (L1/Am), amorphous aggregates in the bulk (Am), and unaggregated peptides in the bulk (Un). The graphs indicate which phase the system would equilibrate to with the given set of parameters.

We analyzed the most common structures observed after 180ns of kinetic

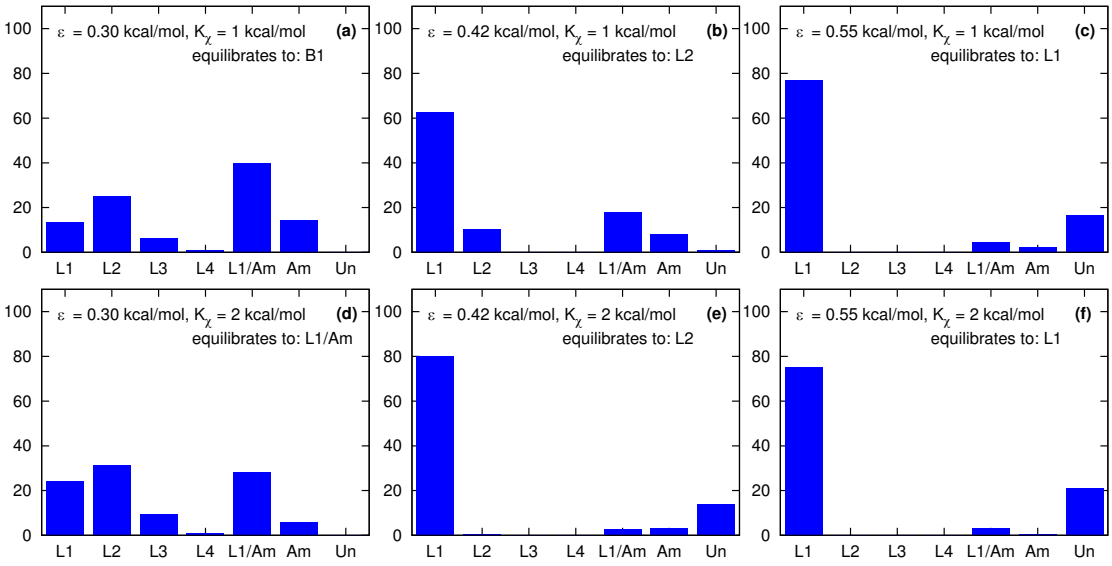

Figure 4.2: Percentage distribution of dominant aggregate phases observed in a kinetic trap at the end of 120 parallel 180ns simulations for varying surface attraction (ϵ) and chiral stiffness (K_χ). They are weighted by the number of peptides involved in each aggregate structure. Aggregate phases counted in the graph are: surface-bound single- to quadruple-layered fibrils (L1-L4), surface-bound layered fibrils with attached amorphous aggregates (L1/Am), amorphous aggregates in the bulk (Am), and unaggregated peptides in the bulk (Un). The graphs indicate which phase the system would equilibrate to with the given set of parameters (as determined in Chapter 3). All simulations are conducted at the low point of the binding transition, below the transition temperature.

simulation, comparing these to our previous thermodynamic results from Chapter 3. The comparisons were made at equivalent points in the transition (the "low" point, below the transition temperature, see Section 4.1.2). We compare equilibrium configurations with the state of the system in its metastable *kinetic trap* that forms during the initial kinetics. Similar data for structure distributions at the transition temperature are shown in Fig. 4.1.

From Fig. 4.2, we observe a significant population of single-layered fibrils bound to the surface for all parameter sets, in particular for stronger surface attractions. Accordingly, we shall first study the formation of single layers in

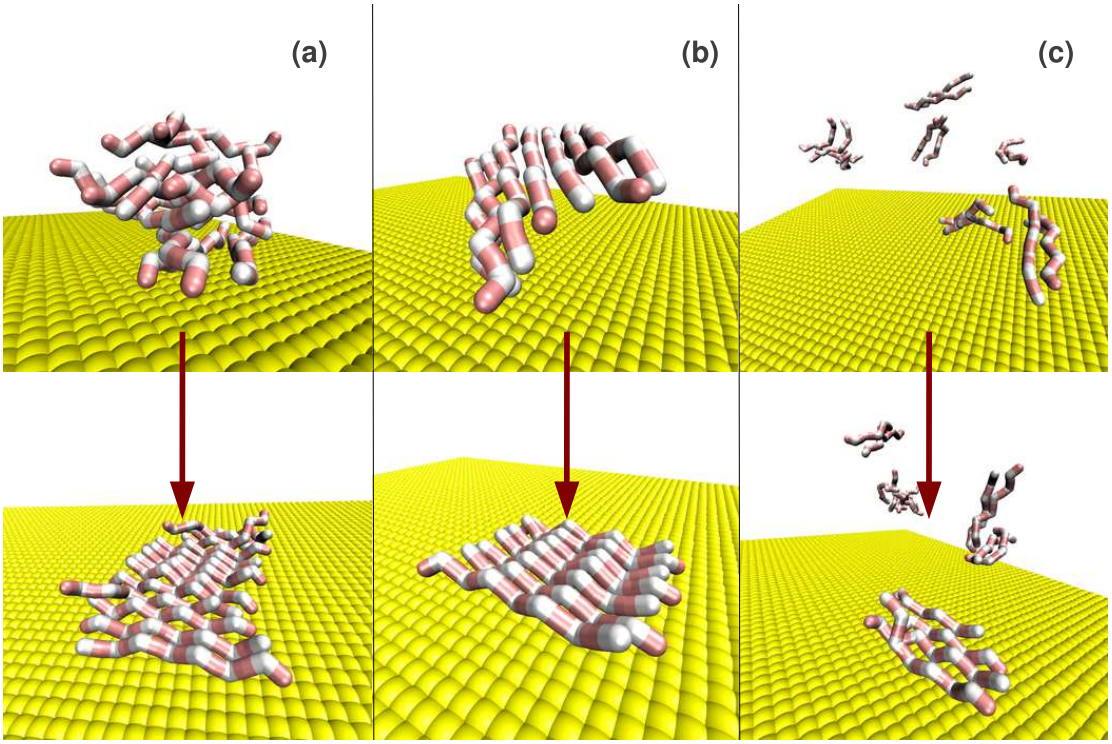

Figure 4.3: Depicts the primary methods by which a single layer can form on the surface. In panel (a), an amorphous aggregate forms in the bulk and then binds to the surface. Peptides near the bottom lock into place as they align favorably with the surface, and slowly a fibrillar layer forms. In panel (b), a fibrillar aggregate forms in the bulk. This fibril lies down on the surface directly. In panel (c), unaggregated peptides in the bulk land on the surface. When other peptides also bind to the surface, they will preferentially orient themselves with the first fibril, and in this way, the initial peptides nucleate fibril formation.

greater detail.

There are three mechanisms by which single layers assemble on the surface, as seen in Fig. 4.3. In mechanism (a), a condensation-ordering transition, an amorphous aggregate forms in the bulk and then binds to the surface. Aggregates near the bottom then align with the surface, eventually forming an ordered fibril. In mechanism (b), a single-layered fibril forms in the bulk and then lies down onto the surface. In mechanism (c), individual peptides bind to the surface, and when

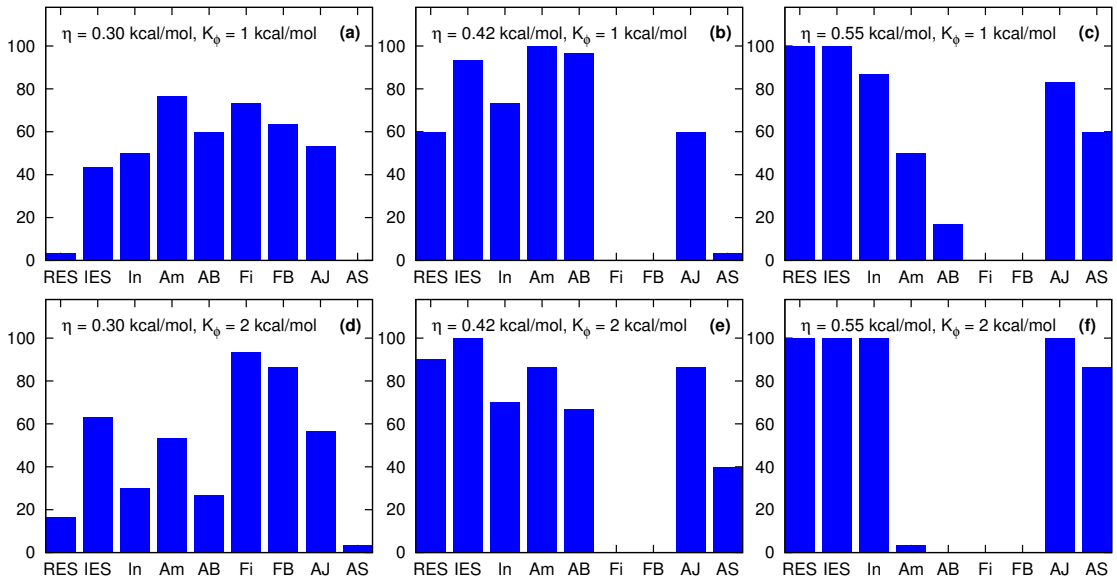

Figure 4.4: Frequency distribution of various kinetic pathways in 30 simulations. 100% means the particular mechanism was observed consistently in each simulation. Abbreviations of pathways on the horizontal axis are as follows: (RES) peptides release spontaneously from the end of a surface-bound fibril, (AES) peptides add spontaneously to the end of a surface-bound fibril, (In) unaggregated peptides deposit individually onto the surface, (Am) amorphous aggregates form in the bulk, (AB) pre-formed amorphous aggregates in the bulk bind to the surface, (Fi) fibrillar aggregates form in the bulk, (FB) pre-formed fibrillar aggregates in the bulk bind to the surface, (AJ) two surface-bound fibrillar aggregates combine into a single one, and (AS) a surface-bound fibrillar aggregate splits into two.

a sufficient number of these have formed a small pre-fibril, they nucleate further fibril growth. The pathway to the formation of single-layered fibrils is affected by the surface attraction and chiral dihedral stiffness parameters, with some variation due to randomness. With the weakest surface attraction, we see all three pathways to some degree. Which of them is dominant depends on the chiral stiffness. With a high chiral stiffness, mechanism (a) occurs at approximately twice the frequency of the other two pathways (refer to Fig. 4.4). With the flexible chiral dihedrals, most single layers form by mechanism (b), though not by a substantial margin.

At medium surface attractions, fibrillar aggregates no longer form in the bulk, so only the pathways of Fig. 4.3 (a) and (c) remain accessible. In both these cases, the dominant pathway to form single-layered fibrils on the surface is by amorphous aggregates in the bulk (Fig. 4.3 (a)).

With the strong surface attraction, the dominant pathway for the formation of single layers is by individual peptide deposition (Fig. 4.3 (c)). This pathway is observed more frequently as surface attraction increases. The degree of individual deposition in the initial kinetics characterizes parameter sets with the sharpest binding transitions in equilibrium (*i.e.*, the jump in mean peptide height during the binding transition is steepest). We never observe the pathway of amorphous aggregates binding to the surface (Fig. 4.3 (a)) for the strong surface attraction with the rigid chiral dihedrals, but it is observed in roughly 20% of simulations for the strong surface attraction, *flexible* chiral dihedral parameter set (refer to Fig. 4.4). After equilibration, amorphous aggregates are no longer present for either chirality, since their final phases are both of type B2 (refer to Fig. 3.3), yet the chiral stiffness affects the pathways accessible to reach this final state by altering the accessible bulk morphologies of the system.

A striking observation is that peptides rarely insert themselves *directly* into the middle of a surface-bound fibrillar aggregate. Rather, a much more dramatic interaction occurs, the dominant examples of which are seen in Fig. 4.5. The layer needs first to break up to allow the new peptides in.

Figs. 4.5 (a)-(c) show peptide insertion into a clean break in a fibril. A pair of peptides floating in bulk solution interact with the middle of the aggregate, causing it to split apart into two pieces, each still bound to the surface. After the two peptides attach themselves to the end of one piece, the split fibrils close back together into a single aggregate, with two new peptides in the middle.

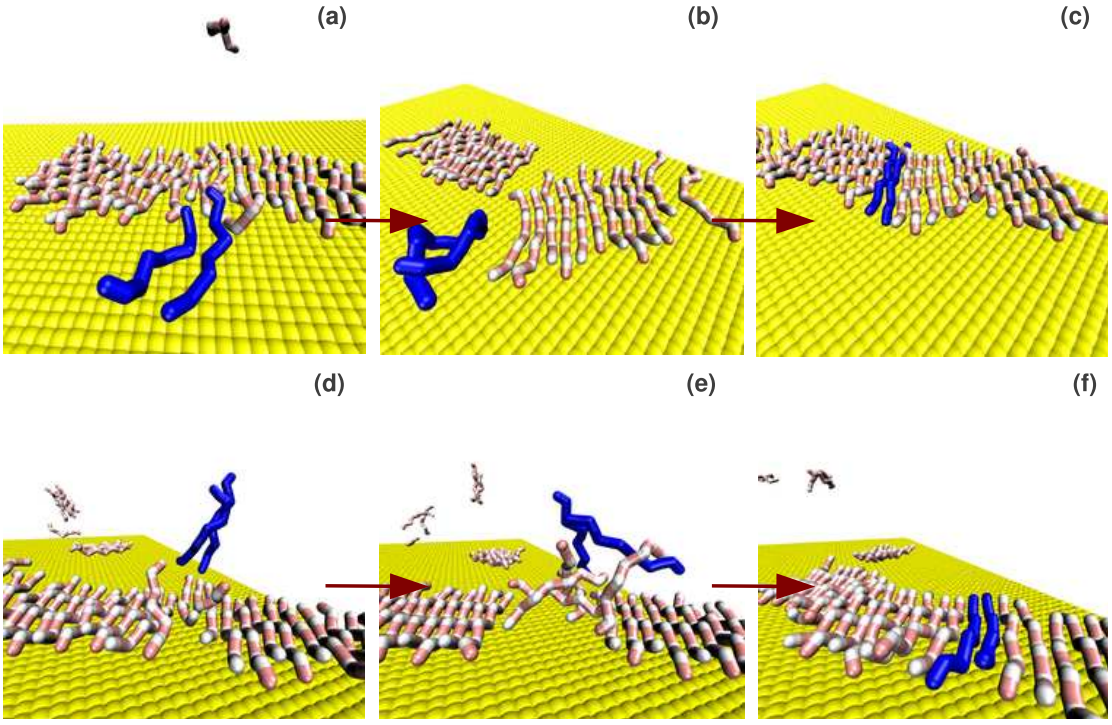

Figure 4.5: Panels (a)-(c) and (d)-(f) show the two most common ways peptides can insert themselves into a single-layered aggregate on the surface. Panels (a)-(c) show peptides inserting into a clean break in the fibril. Panels (d)-(f) show peptide insertions occurring from an amorphous disruption in the center.

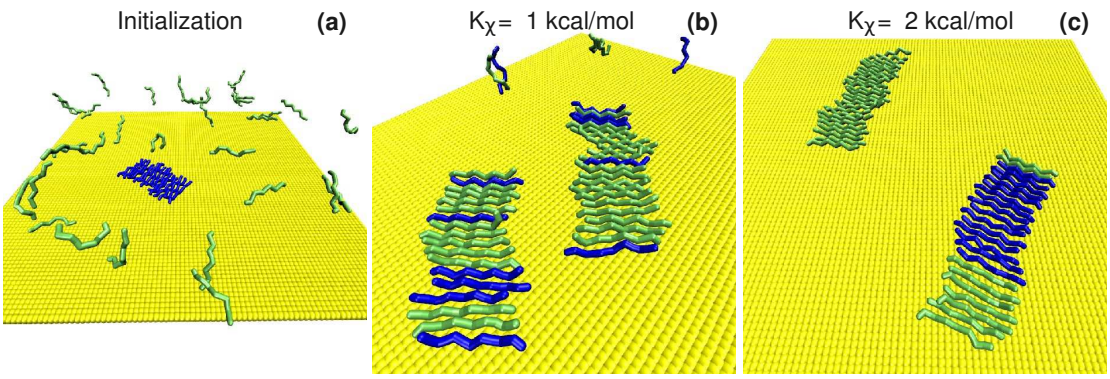

Figure 4.6: Images of the seeding simulation. Fifteen peptides were initially seeded as a single-layered fibril (panel (a)). Panel (b) shows a typical final state for the flexible chiral dihedrals after 180ns, and panel (c) shows the same for rigid chiral dihedrals. Both cases are simulated with the strong surface attraction. Note that in panel (b) there are still peptides unaggregated in the bulk. This causes increased mixing of of the two peptide types as peptides release into the bulk and re-bind to the fibrils.

Peptides can also interact with the center of the aggregate to cause an amorphous disruption in the fibril, in which the inserting peptides become entangled (as seen in Fig. 4.5 (d)-(f)). The "wound" in the center then closes itself, and the disrupted peptides rearrange back into the aggregate, with the initially free peptides now in the middle.

Seeding

We conducted an additional study to analyze in greater detail the assembly and disassembly of single-layered aggregates bound to the surface. The seeding simulation, described in the Methods Section 4.1.2, initializes some of the peptides into a fibrillar aggregate on the surface (Fig. 4.6 (a)), and contrasts the fibril layer formation process for chirally flexible and rigid peptides.

In the final states for flexible peptide fibrils, the 15 seed peptides are typically broken up into 2-10 pieces, separated by the non-seed peptides; for rigid peptides,

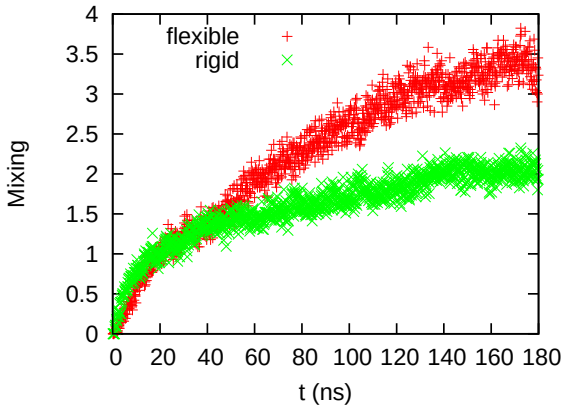

Figure 4.7: The mean number of contacts between bulk and seed peptides over time. This plot represents the degree to which the free peptides and seed peptides mix together in fibrils (mixing parameter defined in Section 4.1.1).

the initial 15-peptide fibril is rarely broken up (Fig. 4.6 (b)-(c)). From Fig. 4.7, we see that up to an average of one contact between seed and free peptides, the rate of mixing in the flexible and rigid peptide cases are similar. After this point, however, we observe that the flexible peptides induce faster mixing of free and seed peptides in surface-bound fibrillar aggregates.

Most of the ways in which the fibril can assemble or disassemble involve only a few peptides. A small number of peptides can be added to or removed from the fibril at the end or the middle. This process can happen spontaneously or via interactions with other free peptides. Fig. 4.8 illustrates these processes.

Figure 4.9 depicts a breakdown of the most common pathways leading to mixing of peptides within a fibril. Most common is for the fibril to break up, either by separating into two fibrils (AS) or by releasing some of its constituents, typically at the end (Fig. 4.8 RES or REI). The separated peptides later integrate into different aggregates, which is how mixing between free and seed peptides primarily occurs. Thus mixing is possible despite virtually all peptide exchanges

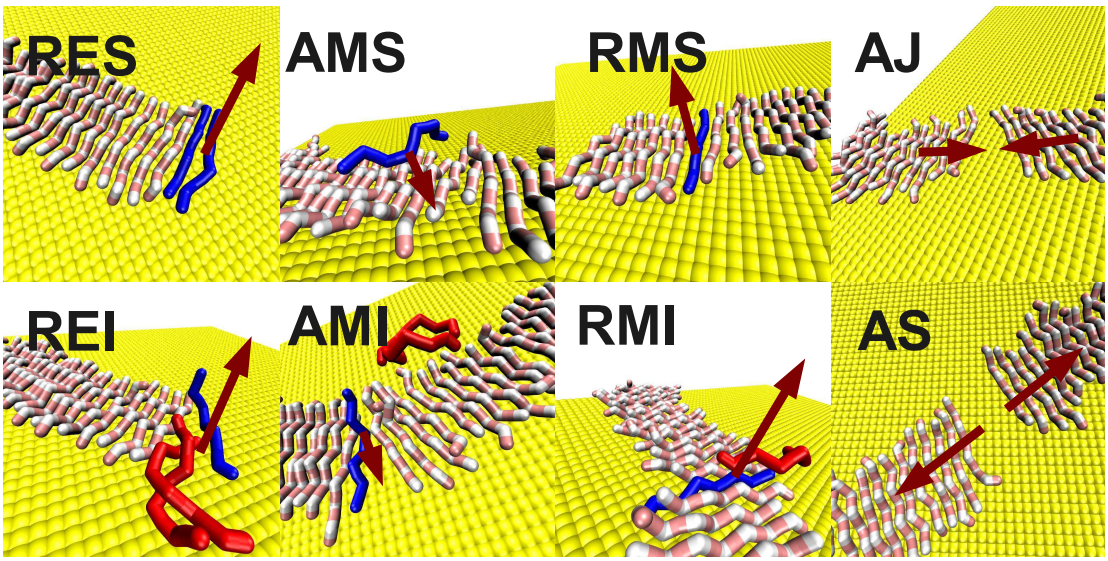

Figure 4.8: Explains abbreviations describing fibrillar assembly or disassembly on the surface. Individual peptides may be added or released from either and end or the middle of a surface-bound fibril. The additions or releases may be spontaneous or may be assisted by free peptides in the bulk. The mechanisms are as follows: (RES) peptides released spontaneously from the end, (REI) peptides released from the end via interaction with bulk peptides, (AMS) peptides added spontaneously to the middle of the fibril, (AMI) peptides added to the middle of the fibril via interaction with bulk peptides, (RMS) peptides released from the middle of the fibril spontaneously, (RMI) peptides released from the middle of the fibril via interaction with bulk peptides, (AJ) two fibrillar aggregates join together, and (AS) two fibrillar aggregates separate. Not shown is AES, which looks identical to RES, but with the arrow pointing in the opposite direction.

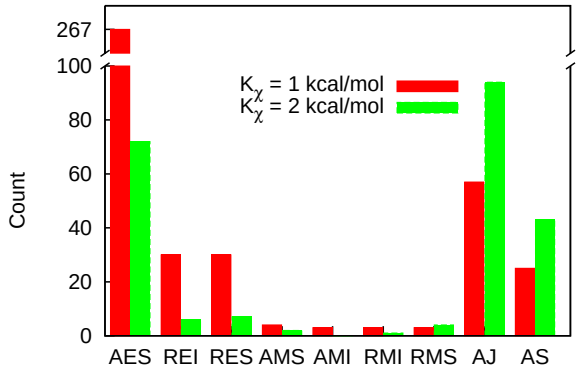

Figure 4.9: The frequencies of pathways resulting in assembly or disassembly of fibrillar aggregates on the surface during the seeding simulations. Only those pathways which *increase or decrease mixing* between seed and free peptides are considered. The count is the number of times a pathway was observed within 30 simulations, each lasting 180ns. Abbreviations are explained in Fig. 4.8. AES refers to peptide additions to the end of a fibril.

occurring at the ends of the aggregates.

If the fibrils never break up during the simulation, the maximum number of additions to the ends of the fibrils (AES) which can increase mixing between seed and free peptides is two per simulation: one free peptide attaching to each end of the original seed fibril. Should more than two such AES events occur that increase the mixing between free and bulk peptides in the fibril, then the fibril must necessarily break up to expose seed peptides for further additions to the ends. Two AES events per simulation amount to 60 such events over the course of 30 simulations. Note that the number of such AES events that increase mixing for the rigid dihedrals (Fig. 4.9) is only slightly higher than 60. Since for flexible dihedrals there are well over 200 AES events, this confirms how stable the surface-bound fibrils are with rigid chiral dihedrals compared to the flexible dihedrals.

Releases are much rarer for stiffer peptides due to them having a greater propensity toward β-sheets, hence requiring more energy to separate from the fibril. This can be seen from Fig. 4.6 (b) and (c), where the flexible peptide simulation shows seed peptides released into the bulk, but the rigid peptide simulation shows all seed peptides are still part of the original seed. The frequency of fibril separation on the surface (AS) is increased for rigid peptides, caused by there being more peptides involved in fibrillar aggregates on the surface in this case.

4.2.2 Other Aggregate Structures

Increasing surface attraction causes the single-layered aggregate to dominate the observed aggregate structures (see Fig. 4.2). Therefore, during the initial kinetics as well as in equilibrium, the surface decreases the diversity of accessible aggregate structures. Additionally, many of the morphologies accessible at lower surface attractions are only metastable kinetic traps that do not persist to equilibrium.

However, the diversity of morphologies observed in the initial kinetics is greater than in equilibrium. These include dominant structures below the binding temperature, such as triple- and quadruple-layered fibrils (see Fig. 4.10 (b)), β-barrels (which can bind to the surface, see Fig. 4.10 (d)), and multi-layered fibrils in the bulk (see Fig. 3.1 Fi). There is a minimal energetic cost to bind multi-layered fibrils to the surface, untwisting them to conform to the flat surface, though the energetic benefit of binding to the surface dominates this.

Instead of binding directly to the surface, as in Fig. 4.3, aggregates forming in the bulk can bind to a surface-bound fibril (see Fig. 4.10 (a) and (b)). These are significant pathways leading to the formation of multi-layered fibrils. The other mechanism is for a multi-layered fibril in the bulk to bind to the surface

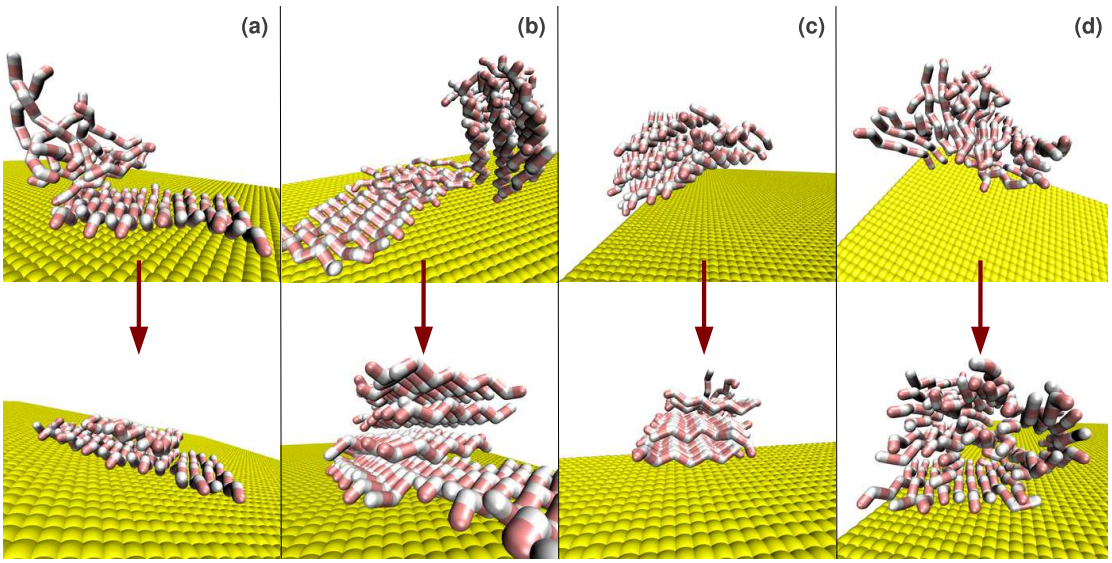

Figure 4.10: Depicts the pathways by which non-single-layered aggregates can form on the surface. In panel (a), an amorphous aggregate forms in the bulk first, and then attaches to a single-layered, surface-bound fibril. Peptides near the bottom lock into place when they align favorably with the initial fibril, and slowly a second fibrillar layer forms. In panel (b), a fibrillar aggregate forms in the bulk. This fibril lies down on a surface-bound fibril. In panel (c), a multi-layered fibril forms in the bulk and binds directly to the surface. In panel (d), several fibrils attach together in the bulk in a mismatched way. This structure binds to the surface and the fibrils fold together to form a β-barrel on the surface.

directly (Fig. 4.10 (c)). There is no analogous pathway to Fig. 4.3 (c) that forms multi-layered fibrils. All pathways involve some initial aggregation in the bulk.

If a bulk amorphous aggregate lands on a pre-formed layer, it will form a double-layered aggregate. We do not observe the formation of triple- or higher-layered aggregates via this mechanism. If, however, the chiral stiffness and temperature are conducive to fibril formation in the bulk, bulk-formed fibrils can lie down on the surface or on a pre-formed single layer (see Fig. 4.10 (b) and (c)). Double-layered fibrils often form via this pathway, and occasionally higher-layered aggregates do as well. Since surface-bound triple and quadruple layers can only assemble from *fibrillar* aggregates in the bulk, there is a significant qualitative effect of bulk morphologies on the initial kinetics.

We also studied the initial binding kinetics equilibrating to the B2 phase (refer to Fig. 4.1). At the transition temperature for the $\epsilon = 0.55$ kcal/mol, $K_\chi = 1$ kcal/mol parameter set, roughly half of the peptides are involved in amorphous aggregates, either in the bulk or attached to surface-bound layers during the initial kinetics. However, these amorphous structures dissipate as the system equilibrates, since the final equilibrium state has no amorphous aggregation. Thus while the absence of any amorphous aggregation is a characterization of the B2 equilibrium phase, it does not characterize the initial kinetics leading up to it.

4.2.3 Order Parameter Equilibration Rates Indicate Cooperativity

In Chapter 3, we found that there were cooperative interactions between the following energetic terms: surface attraction, chiral stiffness, and peptide-peptide interactions. Cooperativity was found to increase at stronger surface attractions.

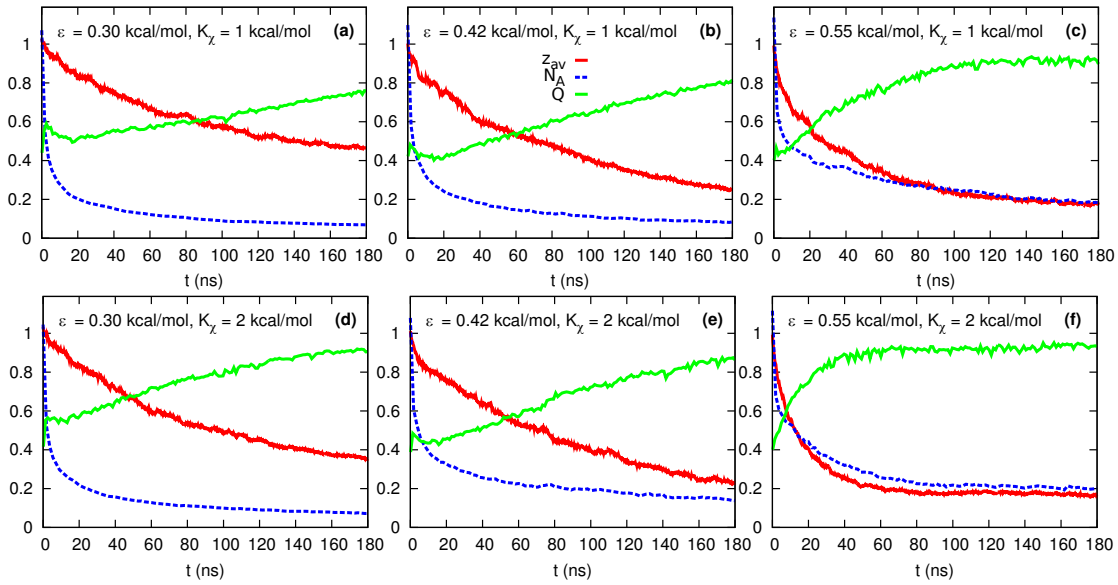

Figure 4.11: Plots of the order parameters of mean height (z_{av}), number of aggregates (N_A), and orientation (Q). The mean height has been normalized to 26Å and the number of aggregates has been normalized to 25. The orientation is as usually defined (normalized to 1). From left to right we have $\epsilon = 0.30$ kcal/mol, 0.42 kcal/mol, and 0.55 kcal/mol. The top row has $K_\chi = 1$ kcal/mol and the bottom has $K_\chi = 2$ kcal/mol. All of these simulations are conducted at the low point of the binding transition, below the transition temperature.

We now observe how the equilibration rates of various order parameters in the initial kinetics are indicative of the level of cooperativity of the system.

Three order parameters were tracked over time below the transition temperature (Fig. 4.11). For our equilibrium simulations in Chapter 3, order parameters measuring both surface binding and aggregate structure exhibited the same progression of structures with increasing *temperature*. However, in this section's kinetic simulations, they do not exhibit the same behavior as a function of *time*. The rate that the peptides' mean height above the surface equilibrates is strongly increased by surface attraction. The rate that the peptides aggregate (minus the slope of the number of aggregates *vs.* time) is affected weakly by either dihedral

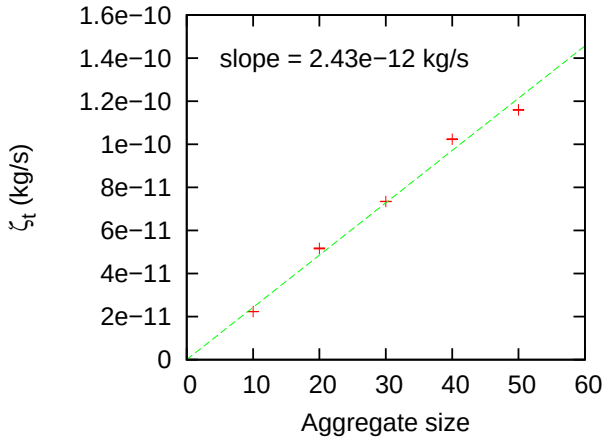

Figure 4.12: Shows the isotropic translational friction coefficients for a fibrillar aggregate on the surface. Conducted with $\epsilon = 0.42$ kcal/mol and $K_\chi = 1$ kcal/mol.

stiffness or surface attraction.

Note that the equilibration rates are very different for the three order parameters plotted in Fig. 4.11 for low surface attractions, but for strong surface attractions their rates are similar. The more cooperative transitions are characterized by the matched behavior of the different order parameters.

In the less cooperative transitions, we see that aggregation and binding occur in the following order: peptide aggregation, orientation alignment (increase in peptide order), and finally binding to the surface. That is, for weaker surface attractions, aggregates form in the bulk first. This allows for such pathways as seen in Fig. 4.10, and confirms that bulk structures have the greatest effect on aggregation pathways in the least cooperative transitions. Conversely, for the strong surface attraction, it is rarer to observe the formation of aggregates in the bulk (refer to Fig. 4.4).

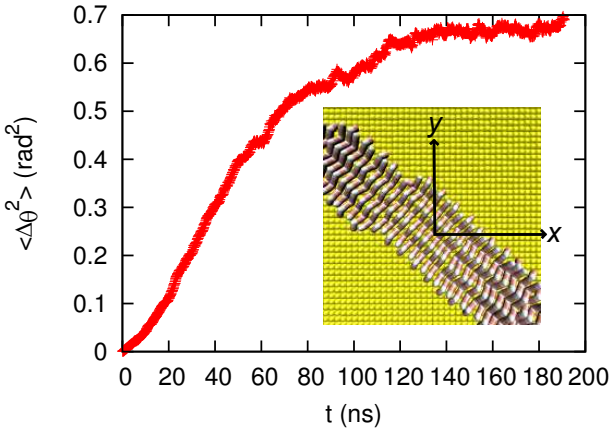

Figure 4.13: Fibrillar orientation exhibits non-Einstein diffusion behavior. At long times, the angle the fibrillar aggregate makes with the x axis of the surface consistently locks to $\pm\pi/4$. This plot is from the 50-peptide diffusion simulation, but the results are similar with different numbers of peptides. The parameters used for this figure are $\epsilon = 0.42$ kcal/mol, $K_\chi = 1$ kcal/mol, and $T = 300$K.

4.2.4 Diffusion

The kinetic statistics of fibrillar aggregates on the surface is diffusive, as expected. The diffusion constant is the same along the axis of the fibril and perpendicular to it, with a friction coefficient proportional to the size of the fibril (*i.e.*, its contact area with the surface).

The friction coefficient for rotational diffusion, however, is ill-defined, since the aggregate tends to align itself $\pi/4$ between the x and y axes of the surface, and the aggregate ceases to diffuse rotationally. A plot of the change in angle squared ($\langle(\Delta\theta)^2\rangle$) *vs.* time is nonlinear and asymptotically levels off as the fibril aligns to the critical angle. Thus the geometry of a surface can enforce a preferred direction for fibrillar growth, and fibrils will tend to grow along it. This phenomenon has also been observed experimentally on graphite, with fibrils growing along angles matching the crystallographic symmetry of that surface [181].

4.3 Summary and Discussion

We analyzed the kinetics of peptide aggregation on a solid surface, which complements our previous work in Chapter 3 on the equilibrium structures of the system. In the present chapter, we focus particularly on which metastable aggregate structures appear in the initial binding kinetics, and in what ways these reflect and differ from known equilibrium structures. We compare results with varying surface attraction and chiral stiffness not at the same temperatures, but at equivalent points along their binding transitions as determined by their mean peptide height *vs.* temperature profiles.

Chapter 3 used the enhanced sampling technique of replica exchange molecular dynamics to study the thermodynamics of peptide aggregation in the presence of a surface. Decreasing equilibration times to within roughly 40ns, this method allowed us to study the equilibrium structures of the system. However, since replica exchange simulations lose all kinetic information, we also conducted the present study in which we simulated the same system with constant temperature molecular dynamics so as to observe the initial kinetics of peptides binding to the surface. In these kinetic simulations, in particular for the weak and medium surface attractions, the system was still caught in significant metastable kinetic traps after 180ns of simulation time. This is not a problem with this work; its purpose was to observe the initial kinetics, as we have already analyzed the equilibrium structures. However, the slow equilibration of constant temperature molecular dynamics simulations validates our prior use of the replica exchange method to study equilibrium structures in such a complex system.

As observed experimentally [181–186], we find that the surface affects the nature of peptide aggregates. For our system, the surface strongly increases the

propensity of single-layered β-sheet fibrils bound to the surface. We find that there are three mechanisms by which such a layer can form: (a) by a bulk-formed amorphous aggregate binding to the surface and peptides near the bottom subsequently re-orienting into a fibril (a condensation-ordering transition), (b) by a bulk-formed single-layered fibril lying down flat on the surface, and (c) by peptides binding individually to the surface and nucleating fibril formation by individual peptide deposition. Peptides with a stiffer chiral backbone prefer mechanism (b) over (a), and stronger surface attractions prefer mechanism (c) over (a) and (b).

Growth of fibrils on the surface usually occurs via interactions with the ends of the fibril. When a peptide does insert into the middle of a fibril, typically the fibril breaks in the middle first, and the new peptide attaches to the end of one of the pieces before the fibril reforms. If peptides in the fibril tend to mix or shuffle their order, we find this to be caused by fibrillar instability, which is known for this peptide model to be higher with more flexible chiral dihedrals [57].

The population of non-single-layered aggregates decreases with stronger surface attractions, and many of these are only metastable and do not persist to equilibrium. Multi-layered fibrils form in a manner similar to single-layered fibril growth mechanisms. Often, though, instead of a bulk-formed aggregate binding directly to the surface, they bind instead to a pre-formed single-layered fibril. Here the types of structures accessible in the bulk significantly affect the subsequent surface-bound morphologies, since a maximum of two layers can assemble from a bulk-formed amorphous aggregate, but bulk-formed fibrillar aggregates are seen to form up to quadruple-layered surface-bound fibrils.

A feature observed previously in the equilibrium simulations is that the qualitative progression of dominant morphologies with temperature depends only on the surface attraction and not on the chiral stiffness. In particular, there

were two classes of binding phases near the transition temperature: one where there was a significant degree of amorphous aggregation (for weak and medium surface attractions), and another with no amorphous aggregation at all (for strong surface attractions). However, we find that in the initial kinetics leading up to the second class of binding phase, amorphous aggregates do form, the degree of which is strongly correlated with the flexibility of the chiral dihedrals in the peptide backbone.

The strongest surface attractions have the greatest degree of cooperativity between the surface attraction, chiral stiffness, and peptide-peptide interactions. In the kinetics, we find that the most cooperative parameter sets are characterized by the individual deposition of peptides onto the surface without aggregating in bulk solution. When we track order parameters measuring surface binding, degree of peptide aggregation, and fibrillar order of the aggregates over time, we note that the equilibration rates of these order parameters converge for the most cooperative transitions. For the least cooperative transitions, we find that aggregation occurs first, then fibrillar alignment, and lastly binding to the surface.

We analyzed the diffusion of a single layer on the surface, and found that the aggregate diffuses isotropically along its axis and in the perpendicular direction. However, the rotation of the fibril is *not* diffusive, but rather the alignment locks to orientations $\pm\pi/4$ from the axes of the grid of the surface. Similar behavior is seen with fibrils of the Aβ peptide on graphite, which form along lines separated by $2\pi/3$, matching its crystallographic symmetry [181].

While it is possible to study the roles of various interactions in peptide aggregation on surfaces using molecular simulations with atomistic detail [187–196], these studies are limited to a very small number of peptides (or a single peptide). Moreover, the coarse-grained simulations presented in this chapter provide

detailed mechanistic information regarding aggregation on surfaces at time scales and at a level of resolution not readily accessible experimentally. Hence coarse-graining [82, 86, 98, 197, 198] is an invaluable complement to atomistic simulations and experiments for probing aggregation both in the bulk and on surfaces.

Chapter 5

Seeded Peptide Aggregation

We are concerned here with the process of seeded peptide aggregation, where the system is initialized with a pre-formed aggregate, as depicted in Fig. 5.1. Systems which are not initialized with an aggregate seed exhibit a lag phase prior to nucleation, as seen in Fig. 5.2. A pre-formed seed can bypass the initial nucleation event, and thus the lag phase, required to initiate the aggregation process. A seeding simulation is ideal to study the growth mechanism of the fibril following the initial aggregation event. Seeded aggregation can also be thought of as aggregation on a surface, as the seed acts as a surface for the bulk peptides to template onto.

It has been found that polypeptides of one type can be used to seed fibrillar growth of a similar polypeptide [20, 21, 29, 199–204], differing by either small mutations or in length. However, altering the sequence of the monomers from that of the fibrillar seed results in decreased efficiency of fibril formation [20, 21]. In fact, co-aggregation between different peptide sequences is rare, and in general will only occur for very similar sequences. However, recent experimental evidence suggests that Aβ40 and Aβ42 mutually affect each other's aggregation kinetics

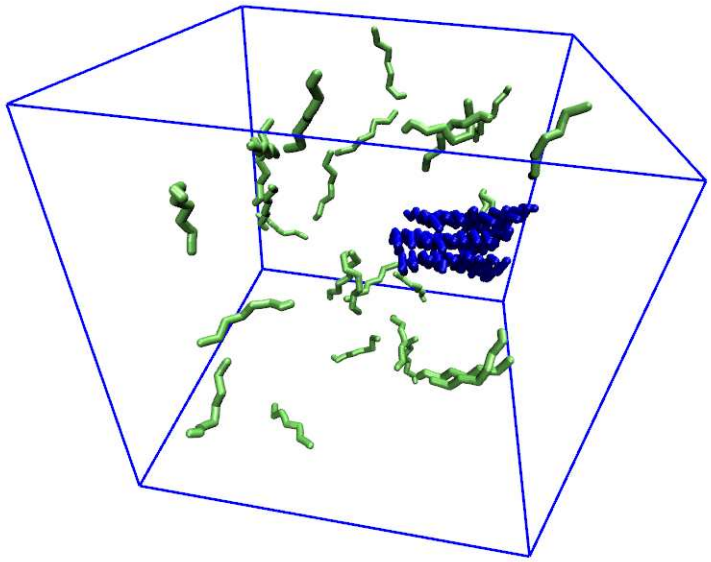

Figure 5.1: A depiction of seeded aggregation. The system is initialized with a pre-formed aggregate (three-layered fibril shown in dark blue) and the remainder of the peptides unaggregated in the bulk (shown in light green). The simulation box, with periodic boundary conditions, is also depicted.

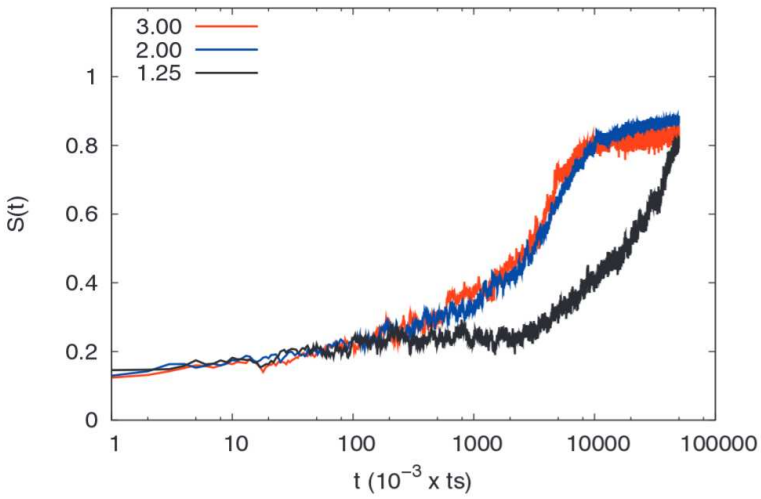

Figure 5.2: The sigmoidal kinetics characteristic of a lag phase observed in unseeded peptide aggregation in simulations by Bellesia *et al.*, using the same peptide aggregation from this work [58]. The graph plots the orientation parameter (Q) as a function of time for peptides with varying stiffness parameters, $K_\chi = 1.25, 2.00,$ and 3.00 kcal/mol.

through co-aggregation [199]. This is particularly relevant to biomedicine in light of the fact that small changes in the ratio of Aβ42:Aβ40 have a dramatic effect on neurotoxicity [205, 206]. Surprisingly, experiments have shown that peptides can aggregate in very small concentrations with peptides of an unrelated sequence by means of stabilizing interactions involving the peptide backbone, with potential applications in novel nanomaterials [207]. Changing the morphology of the peptide seed also results in fibrillar elongation with distinct efficiencies [208].

In this chapter, the effect of seeds in templating the morphology of peptide aggregates is examined using molecular dynamics simulations and the coarse-grained peptide representation described in Chapter 2.1. Particular attention is paid to contrasting how the β-sheet propensity of both seed and bulk peptides affects the kinetics of aggregate merging and growth. And in cases of intermediate β-sheet propensity, we can determine the roll of polymorphism in guiding fibrillar

growth.

5.1 Methods

5.1.1 Simulations

Of the 54 peptides in the system, 27 (the *seed peptides*) were initialized into an aggregate seed, while the remaining 27 (the *free peptides*) were randomly distributed within the $(10\text{nm})^3$ periodic simulation box. Some simulations had an amorphous seed aggregate, comprising flexible peptides ($K_\chi = 1.00$ kcal/mol); others had a fibrillar seed aggregate, comprising rigid peptides ($K_\chi = 2.00$ kcal/mol). For each type of seed aggregate, we considered free peptides with one of the following chiral dihedral stiffnesses: $K_\chi = 1.00, 1.25, 1.50$, or 2.00 kcal/mol. For each of these eight parameter sets, 52 parallel simulations were conducted with randomized free peptide initial conditions. Simulations ran at a temperature of 305K for 500ns. Additionally, we conducted 40 parallel simulations for rigid free peptides with a β-barrel seed aggregate (see Figs. 5.10 and 5.4).

5.1.2 Order Parameters

In our analysis, we shall be concerned with three order parameters. For each system, the order parameter is calculated as the average over the parallel simulations, and is time-dependent. First is the orientation (Q), which is a measure of peptide alignment, normalized to 1 when all peptides are in a parallel (or anti-parallel) alignment, and equaling 0 when their orientations are uncorrelated. The exact form of Q is Eq. 3.1 and it is found in the literature [58, 110, 180]. Second is the number of fibrillar contacts (C_1). For each pair of adjacent peptides where no

X interaction center on one peptide is farther than 3.5Å from an X interaction center on the other, one contact is counted. That is, it counts the pairs of peptides that are neighbors in the same fibril. Third is the nearest neighbor mixing (N_{fs}) which counts how well the free and seed peptides are mixed together in the combined aggregate. For each peptide in the simulation, N_{fs} determines whether the peptide nearest to it is a free or seed peptide. If the nearest peptide is of the *opposite* type, then N_{fs} is incremented by 1. Note that this definition of the mixing is not biased to amorphous or fibrillar aggregates (unlike the mixing from Chapter 4 where we studied seeding only for fibrillar aggregates).

5.2 Results

The pathways for the different systems are shown in Figs. 5.6-5.14. The seed aggregate is represented in dark blue, and the free peptides in light green. The large red arrows depict the dominant pathways, and the smaller green arrows depict lesser visited ones. The dynamics of the peptides and oligomers are diffusion-dominated until they collide and stick to other peptides. This sticking is reversible, although the general trend is to aggregation. From the thermodynamic study of the model in Chapter 3, we know that the structure will fluctuate out of an aggregated state. However, the time scale on which we are simulating here captures the initial aggregation kinetics but is not intended to represent the thermodynamics of the equilibrium state. Hence the final states shown here are only final for the *initial* process of aggregate formation.

Although the mechanisms observed by varying the β-sheet propensity of the peptide seed and the free peptides are diverse, the initial pathways can always be broken down into the following steps: (i) the free peptides diffuse in the bulk and

attach individually to the seed (*e.g.*, Fig. 5.6 B); (ii) the free peptides diffuse and aggregate among themselves (*e.g.*, Fig. 5.6 C); (iii) the free peptide aggregates collide with the seed (*e.g.*, Fig. 5.6 D); and (iv) the free aggregates merge with the seed and begin to rearrange in a way dependent on the dihedral stiffness of both the free and seed peptides (*e.g.*, Fig. 5.6 E-G). In the letterings of Figs. 5.6-5.14, A corresponds to the initial configuration, and B-E correspond to steps (i) through (iv). We now discuss the ways in which the pathways of four illustrative case systems are distinct.

5.2.1 Case 1: Homogeneous Seeding and Aggregation: Fibril Seed ($K_\chi = 2$ kcal/mol) and Free Peptides of High β-Sheet Propensity ($K_\chi = 2$ kcal/mol)

The first case we consider is a homogeneous seeding simulation, where both the seed and the free peptides are of the same type (same K_χ). In this case, the seed is a three-layered fibril consisting of rigid $K_\chi = 2$ kcal/mol peptides. In the bulk, peptides with $K_\chi = 2$ kcal/mol assemble readily into fibrils via the initial formation of ordered small β-sheet oligomers. This case is representative of fibril elongation for peptides with high β-sheet propensity. The most common fibrillar growth pathways are shown in Fig. 5.6. In step (i), the free peptides' high chiral stiffness holds them in a state favoring attachment to the fibril without rearrangement. Hence these peptides favor a *direct-lock* mechanism, also known as the 1-step fast deposition mechanism [59], which differs from the 2-step dock-lock mechanism [112, 209] in that docking and locking occur simultaneously with no structural rearrangement of the peptides. However, sometimes the stiff peptides will need to rotate and diffuse along the fibril before finding a suitable spot to

lock on. The direct-lock mechanism is also observed with stiff free peptides and a β-barrel seed (Fig. 5.10). We note that in step (ii), the free peptides form small ordered β-sheet oligomers (Fig. 5.6 C). In step (iii) the free sheet locks onto the seed simply by aligning to its orientation. Once they align, they immediately form an energetically stable configuration (known as the N* conformation), so the free peptides tend not to mix with the seed. This is analogous to the direct-lock mechanism seen for individual monomers in step (i), and also similar to the seeded growth mechanism seen by Hall *et al.* [210]. A lesser, yet interesting, pathway involves the initial formation of a β-barrel in the bulk (Fig. 5.6 C2) that attaches to the seed and then unrolls to form a new layer on the seed. The seed can thus grow both longitudinally and laterally, analogous to the growth of a β-spine discussed in Chapter 1.2. It shows little mixing between the original seed peptides (blue) and the bulk peptides (green).

5.2.2 Case 2: Heterogeneous Seeding and Aggregation: Fibril Seed ($K_\chi = 2$ kcal/mol) with Flexible Peptides ($K_\chi = 1$ kcal/mol)

The second case that we consider is the interaction of peptides with low β-sheet propensity (flexible peptides, $K_\chi = 1$ kcal/mol) with a fibril seed made from rigid peptides ($K_\chi = 2$ kcal/mol). In the bulk, the flexible peptides do not make fibrils but rather populate amorphous, disordered structures. Snapshots of representative configurations along the main aggregation pathways are shown in Fig. 5.7. Interestingly, the major species at the end of the simulations is a multi-layered fibril. Hence, even though the free peptides preferentially adopt amorphous structures on their own, the fibril seed can serve as a template for additional fibrillar

growth.

The mechanism of fibril growth from the fibrillar seed is dramatically different from the case considered above in which the free peptides were rigid. Step (i) is a typical dock-lock mechanism, where the free peptides bind to the seed and then straighten out to lock onto the fibril. The small disordered (amorphous) oligomers formed in step (ii) attach to the fibril seed in step (iii). An amorphous aggregate is highly entropic and dynamic, and therefore able to disrupt the stability of the fibrillar seed at the interface between the fibril seed and amorphous aggregate, seen most dramatically in Fig. 5.7 E. In this pathway, since amorphous aggregates readily absorb other aggregates into themselves, the free peptides mix to a high degree with the seed peptides (Fig. 5.3 (e)), although the peptides may still re-form β-sheet structures via a condensation-ordering transition after the initial disruption (Fig. 5.7 G). The end-result is a multi-layered fibril that shows significant mixing of the original (blue) fibril and the flexible (green) peptides.

In this system, highly-flexible peptides that in seedless aggregation conditions form unstable, amorphous aggregates with high hydrophobic exposure are incorporated into stable fibrillar aggregates that are less prone to interact with membranes and are potentially less cytotoxic.

5.2.3 Case 3: Heterogeneous Seeding and Aggregation: Fibril Seed ($K_\chi = 2$ kcal/mol and Free Peptides with Intermediate β-Sheet Propensity ($K_\chi = 1.5$ kcal/mol)

Perhaps the most interesting case corresponds to the one where the free peptides have moderate flexibility. In the bulk, these peptides aggregate to form a range of structures, including fibrils, β-barrels, and amorphous aggregates. We consider

here a fibril seed.

Fig. 5.8 shows representative conformations along the aggregation pathways. What is immediately apparent is that there is a much larger diversity of pathways, with more complex branching. This is due to the fact that peptides with intermediate flexibility exhibit a larger diversity of structures and therefore have a broader spectrum of interactions with the seed. One of the major end-products involves the formation of a poorly-mixed, ordered four-layered fibril (5.8 F), very much like the one seen in case 1 (homogeneous seeding of rigid peptides). The growth mechanism parallels that of case 1, with either individual peptides, or small β-sheet oligomers attaching to the fibril. A second dominant pathway results in the formation of what is predominantly a four-layered fibril, but contains a β-barrel (Fig. 5.8 F2). The Fig. 5.8 E$\rightarrow$F2 pathway occurs when the free peptides of the E state have a less ordered alignment than in the E$\rightarrow$F pathway. As a consequence of this, there is a higher degree of mixing in the F2 state than the F state. Similarly, the determining factor of whether the Fig. 5.8 B$\rightarrow$C or B$\rightarrow$C2 branch is taken is whether the free peptides initially form ordered or disordered oligomers before binding to the seed.

5.2.4 Case 4: Heterogeneous Seeding and Aggregation: Amorphous Seed ($K_\chi = 1$ kcal/mol) with Rigid Peptides ($K_\chi = 2$ kcal/mol)

The final case that we consider is "opposite" to case 2. This system has an amorphous seed made of flexible peptides, with rigid free peptides in the bulk (see Fig. 5.9). The initial stages of aggregation involve the embedding of a single peptide (step (i)), or of a small β-sheet (step (ii)) into the amorphous seed. These

absorbed peptides subsequently organize into β-sheet-rich structures, inducing the seed peptides to order with them. While the case with a rigid fibril and flexible free peptides leads primarily to the formation of mixed, yet ordered, multi-layered fibrils, the present case typically results in the formation of well-mixed, but only partially ordered, fibrils. The most common end-product (structure G in Fig. 5.9) has a well-mixed triple-layered fibril, to which is attached an amorphous, mixed aggregate. It is important to note that the proportion of flexible and rigid peptides is the same in cases 2 and 4, but that the initial conformation (flexible amorphous seed versus rigid fibril seed) dictates the final configuration. This is another example of kinetic trapping (as occurs in experiment and *in vivo*), since the equilibrium structure must be the same in both cases.

5.2.5 Mixing Order Parameter Differentiates Aggregation Mechanism

The pathway diagrams shown in Figs. 5.6-5.9 illustrate that the kinetics and the degree of mixing between seeds and free peptides are governed by the interplay of the β-sheet propensities of both the seed and free peptides. In order to quantify the formation of the aggregates and the degree of mixing we analyze a number of order parameters as a function of time (Fig. 5.3). We consider parameters representing the orientation (alignment of the peptides), the number of fibrillar contacts, and the degree of mixing. The left hand plots correspond to amorphous seeds, while the right hand plots are for fibrillar seeds.

Case 1, which involves a direct-lock mechanism of fibril-fibril attachment, has accelerated fibril growth compared to other mechanisms. The trajectories are characterized by a rapid initial fibrillar alignment, a high number of fibrillar con-

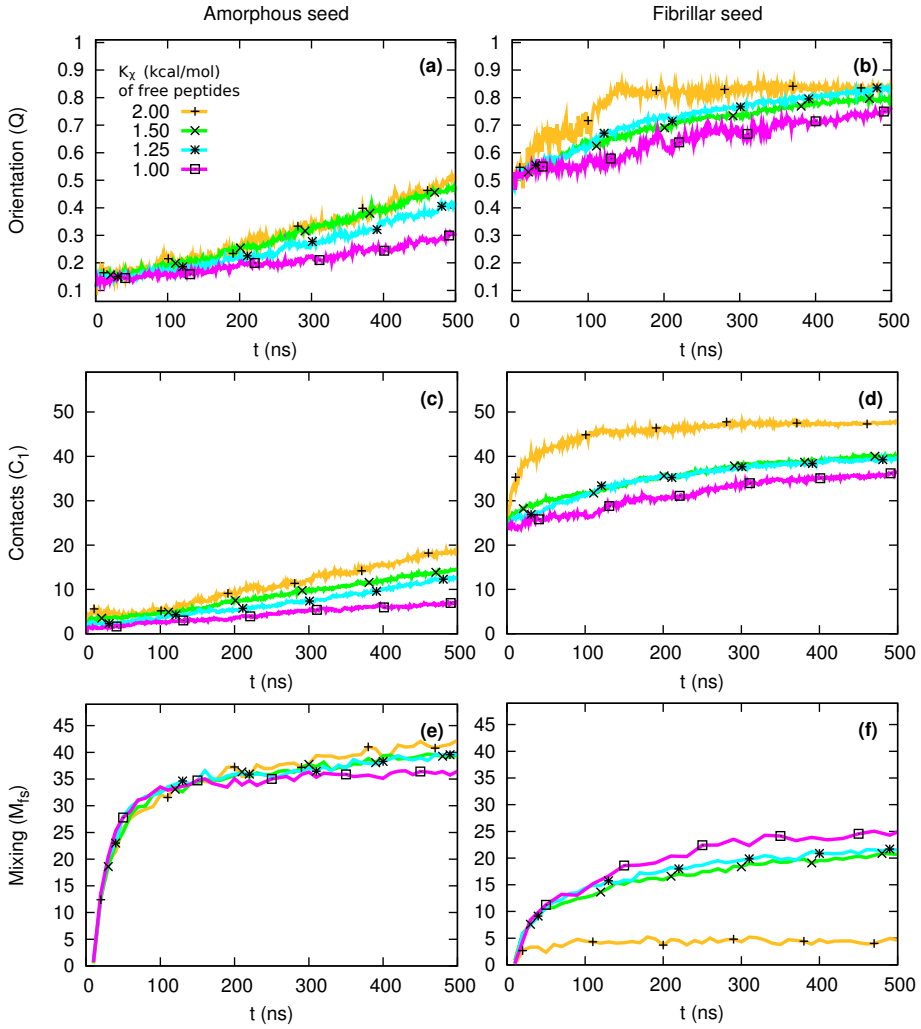

Figure 5.3: Plots of three order parameters *vs.* time, or the aggregation kinetics: (a-b) orientation parameter, (c-d) fibrillar contacts, and (e-f) nearest neighbor mixing (*cf.* a β-barrel seed, Fig. 5.4). Panels on the left have amorphous seeds, while panels on the right have fibrillar seeds. Data for varying free peptide chiral stiffness shown as colored lines. A small subset of these data are represented as black symbols to help distinguish the four sets in each panel by means other than color. The rate of increase of fibrillar order (measured by panels (a-d)) correlates with the chiral stiffness of either the seed or fibril, which is expected since we know that K_χ is a measure of the β-sheet propensity. Mixing anti-correlates with free peptide chiral stiffness for fibrillar seeds, but is not strongly affected by free peptide stiffness with an amorphous seed.

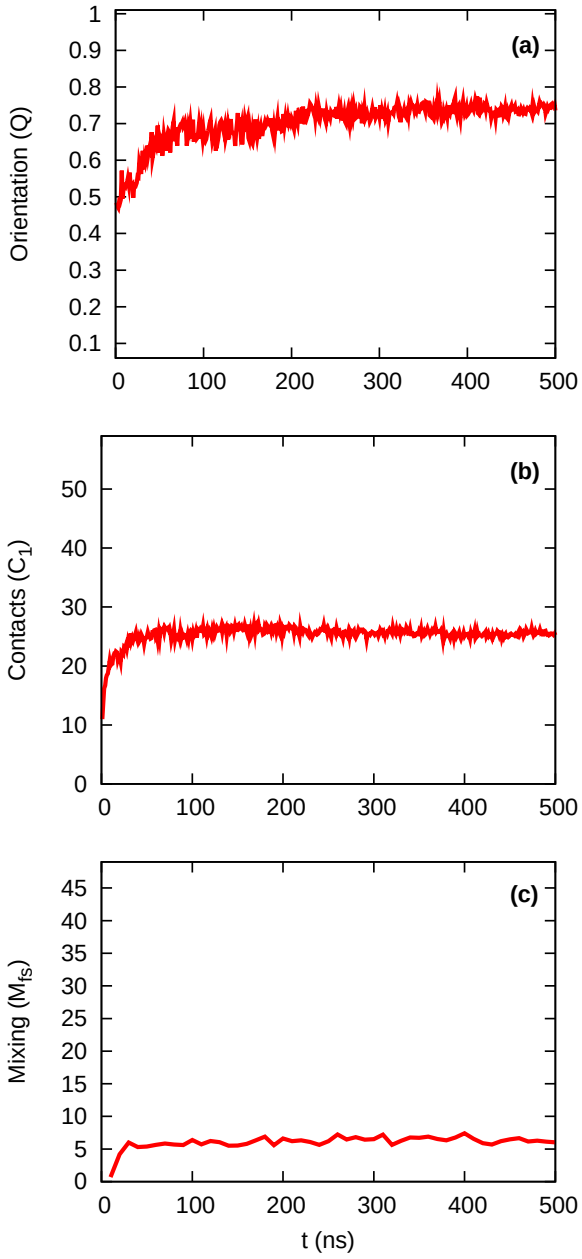

Figure 5.4: Plots of three order parameters *vs.* time for a β-barrel seed and rigid peptides ($K_\chi = 2$ kcal/mol): (a) orientation parameter, (b) fibrillar contacts, and (c) nearest neighbor mixing. Compare to Fig. 5.3. The similarity of this case to that of a fibrillar seed with rigid free peptides is due to them both using the same direct-lock mechanism.

tacts, and a minimal degree of mixing between seed and free peptides (Fig. 5.3 (b), (d), and (f)). In particular, the peptide orientation *vs.* time curve increases linearly (no lag phase) until it sharply saturates at its maximum orientation, corresponding to the free peptides locking onto the seed until all free peptides have done so. The same behavior was observed for rigid free peptides with a β-barrel seed (see Fig. 5.10), which also aggregates by the direct-lock mechanism. Orientation *vs.* time curves for other parameter sets are strikingly different, increasing smoothly without any noticeable transition.

In contrast to a fibrillar seed, a large amorphous seed initially absorbs free peptides into itself (Fig. 5.9 E), with any ordering in the merged amorphous aggregate necessarily subsequent to this (refer to Figs. 5.12-5.14). This results in a uniformly high degree of mixing between free and seed peptides for all values of free peptide chiral stiffness (Fig. 5.3 (e)). What changes when the free peptide chiral stiffness varies is the likelihood of β-sheet structures to form within the merged amorphous aggregate, with increasing likelihood for higher values of free peptide K_χ. However, we do not find such significant differences in pathways with an amorphous seed as a fibrillar seed (*i.e.*, with amorphous seeds, we do not see such dramatic mechanistic differences as exist between Figs. 5.6 D and 5.7 E).

In previous unseeded studies [58], we observed a distinct lag phase in the orientation order parameter for aggregation with all stiffnesses. As seen in Fig. 5.3 (a-b), the presence of a seed removes the lag phase, as seen experimentally [211–215]. For unseeded studies, plots of orientation *vs.* time are sigmoidal, switching at a turning point from concave up to concave down. With amorphous seeds, the seeding plots of orientation *vs.* time begin before this turning point; however, with fibrillar seeds, the orientation *vs.* time plots begin after this turning point, concave down (Fig. 5.3 (a-b)). Thus a fibrillar seed initializes the system at

a point farther along with respect to peptide orientation (a measure of long-range fibrillar order). Note that order parameters blind to fibrillar order, such as nearest neighbor mixing (Figs. 5.3 (e-f)), do not exhibit this particular qualitative difference between amorphous and fibrillar seeds.

5.3 Summary and Discussion

Our study of the pathways involved in seeded peptide aggregation focused on how aggregation pathways differ for amorphous and fibrillar seeds, and how the β-sheet propensity of the free unaggregated peptides affects the mechanisms of seeded aggregate growth. All parameter sets exhibit the following common steps during the initial stages of aggregation: the free peptides diffuse in the bulk and attach individually to the seed; the free peptides aggregate among themselves; the free peptide aggregates collide with the seed; and subsequently the aggregates merge and rearrange in a way dependent on the dihedral stiffness of both the free and seed peptides. In the bulk diffusion step, if the seed is fibrillar and the free peptides are flexible (*i.e.*, have a low β-sheet propensity), we observe the well-known dock-lock mechanism [209]. A flexible peptide docks onto the fibril, then diffuses, re-orients, straightens out into the N^* conformation [86], and locks on when it finds a suitable attachment point. An individual rigid peptide, on the other hand, is by default in a state that can immediately lock onto the fibril if aligned properly. If the seed is amorphous, rather than fibrillar, the seed simply absorbs free monomers.

The current model does not include explicit water molecules, although this could influence the four steps described above, in particular the merging step. The specific behavior is determined by the type of seed and the chiral flexibil-

ity of the free peptides. For a fibrillar seed and flexible free peptides, the free peptides form amorphous aggregates, which undergo a generalization of the dock-lock mechanism: unstructured *aggregates* dock onto the seed and then undergo structural reorganizations to align their constituents to the seed, similar to results from experiment [216] and simulation [217]. We further note that as part of the locking process, docking amorphous aggregates disrupt, or fray, the ends of the fibrillar seed, causing a dramatic mixing between free and seed peptides after the free peptides lock onto the fibril. Emergence of any fibrillar structures in the amorphous seed occurs during the rearrangement step. Fibrillar free peptide aggregates, on the other hand, behave analogously to N^* monomers, and attach to the outside of a seed fibril directly without structural rearrangement. In this case, peptides mix to a very low degree. Experimentally, the degree of mixing could in principle be tested by labeling either the seed or the free peptides, *e.g.*, through C13 carbonyl labeling of select residues, as in the isotope-edited IR work of Decatur and co-workers [218]. The most complex mechanisms are exhibited by free peptides of intermediate β-sheet propensity. What morphology they initially form influences the aggregate growth pathway taken.

In one particular system, a fibrillar seed with free peptides with a β-sheet propensity of $K_\chi = 1.25$ kcal/mol, we observe a unique mechanism of lateral growth at the end of a fibril, where parallel layers split apart into a "Y" and the arms fold back to form an "m" (Fig. 5.11 G→H).

We find that an aggregate seed is in some respects analogous to the solid surface from Chapters 3 and 4 as a template for peptide addition. Both cases have as primary adsorption mechanisms condensation-ordering and direct-locking to the template. While the final structures of adsorbed free peptide aggregates are similar, a fibrillar seed, unlike a solid surface, is itself affected by the free

peptides. On our solid surface, the bottom layer of bound peptides was always a fibril, and any bound disordered aggregate in the system lay necessarily on top of a fibrillar bottom layer. In contrast, since a fibrillar aggregate seed can be partially disrupted by an amorphous free aggregate, the two can bind to each other without the free peptides creating a fibrillar interface (rather a disordered interface is made in the seed by the free peptides). The order imposed by a highly symmetric solid surface simplifies the dynamics of aggregate growth considerably.

Coarse-grained models enable study of aggregation on time and length scales inaccessible to fully atomistic simulations and can be used to complement and help interpret experimental studies. They have been successful in elucidating the role of peptides' β-sheet propensity in the kinetic pathways of fibrillar growth [91, 219], showing that β-sheet propensity is negatively correlated with a heterogeneity of elongation pathways, and that it controls accessible growth mechanisms.

Our simulations help rationalize the different aggregate growth mechanisms proposed in the literature. While peptide aggregation is highly sequence-dependent [6, 18–21], the vastness of the space of sequences in comparison to the number of *accessible* aggregate morphologies suggests that a more universal property controls the mechanism of aggregate formation [6]. We find the peptide's β-sheet propensity to be a crucial determinant of mechanism in aggregate formation. For our model, we found that the rate free peptides combine with the seed was diffusion-limited since the rate was virtually unaffected by the type of aggregate seed and completely unaffected by the β-sheet propensity of free peptides (see Fig. 5.5). Experimentally, it is known that seeding removes the lag phase necessary to nucleate aggregate growth. Plots of various relevant order parameters confirm that the lag phase is absent compared to our previous simulations of unseeded aggregation [58].

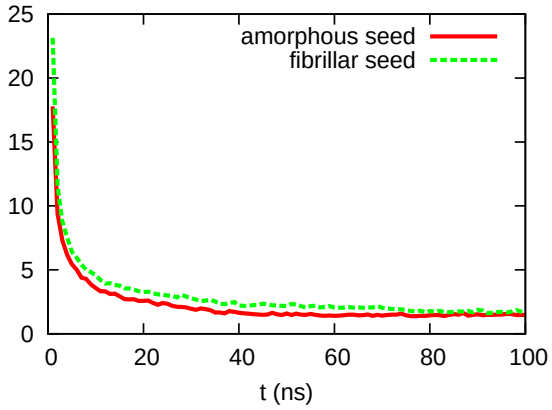

Figure 5.5: Average number of aggregates in the system *vs.* time. Measures the degree of free peptides docking to the seed by counting distinct aggregates (either amorphous or fibrillar). With our definition, a lone peptide is counted as a single aggregate. Thus the number of aggregates has a theoretical maximum value of the number of peptides in the system, and a minimum of 1 when the free peptides are fully docked to the seed. The tail from 100ns to 500ns is suppressed. Note that the number of aggregates counts aggregates of all types, so this measures the rate peptides clump together, or the docking rate, not the rate *ordered* fibrils form.

The kinetic process underlying peptide aggregate formation is extremely important from a biological perspective as different aggregate morphologies exhibit different levels of toxicity to the cell. It has been shown that cytotoxicity is considerably higher in energetically unstable oligomeric species than in mature fibrillar aggregates [35, 38–40]. Our simulations indicate that it is possible to sequester peptides with different degrees of β-sheet propensities from solution into fibrils provided that they are sufficiently close in sequence to co-aggregate. In particular, highly-flexible peptides that form unstable, amorphous aggregates with high hydrophobic exposure in the absence of a seed, may become incorporated into stable fibrillar aggregates when a fibrillar seed is present. Being less prone to interact with membranes, fibrillar aggregates are potentially less cytotoxic. It may be possible to control the type of aggregates peptides form by introducing

seeds of aggregate-compatible peptides with a differing β-sheet propensity into the system.

5.4 Pathway Diagrams

Here we show the morphology transitions observed for each system, with the most common transitions marked by thicker red arrows.

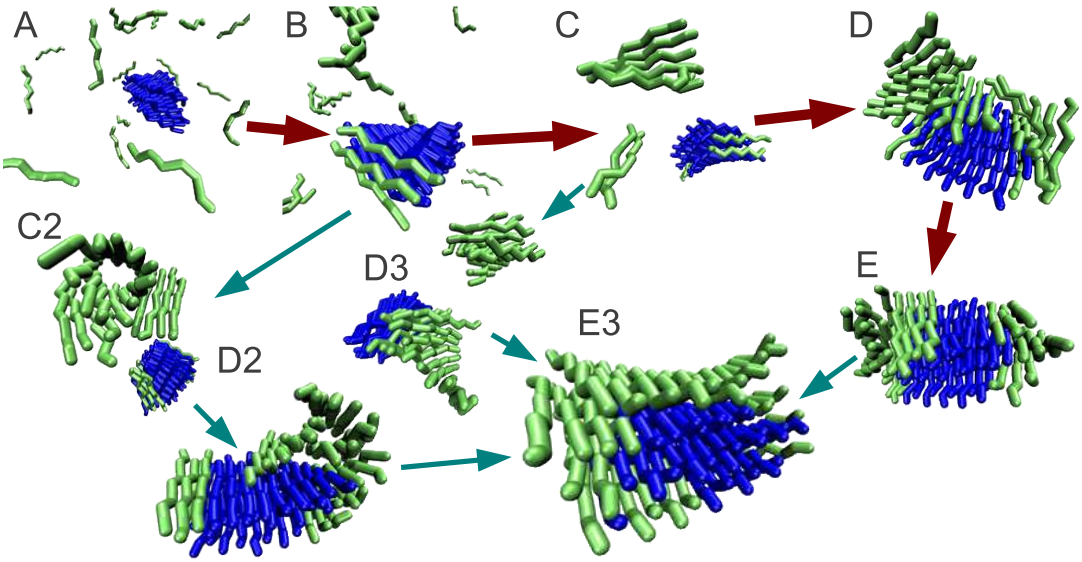

Figure 5.6: A fibrillar seed with rigid ($K_\chi = 2$ kcal/mol) free peptides. The morphologies are as follows: (A) the initial configuration; (B) the free peptides attach individually to the seed by a direct-lock mechanism; (C) the free peptides form fibrillar oligomers; (D) fibrils attach to the seed, but are imperfectly aligned; (E) most fibrils align to the seed, with a few peptides still misaligned; (D3) fibrils begin to attach directly to the seed, forming a larger fibril; (E3) attached fibrils shift to form a poorly-mixed quadruple-layer; (C2) free peptides form a β-barrel structure in the bulk; and (D2) the free β-barrel attaches to the seed, eventually unrolling to form a new layer on the fibrillar seed (state E3).

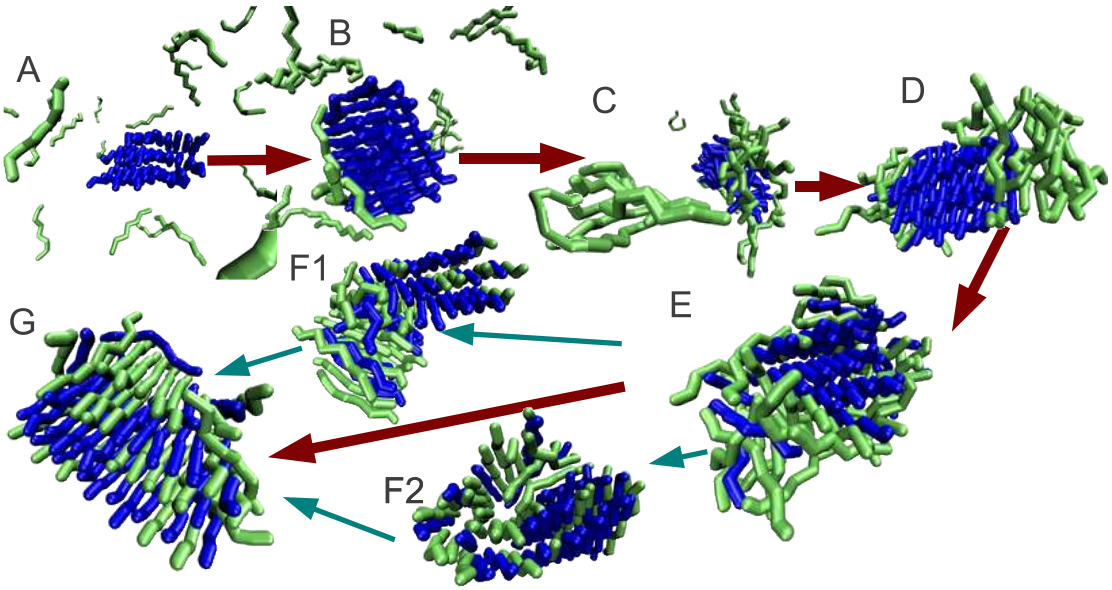

Figure 5.7: A fibrillar seed with flexible ($K_\chi = 1$ kcal/mol) free peptides. The morphologies are as follows: (A) the initial configuration; (B) the free peptides attach individually to the seed by a dock-lock mechanism; (C) free peptides form amorphous aggregates; (D) free aggregates attach to the seed; (E) the amorphous aggregate frays the seed and disrupts its fibrillar structure; (F1) an uneven fibrillar attachment forms within the combined fibril; (F2) a β-barrel structure emerges from the combined fibril; and (G) peptides even out to form a multi-layered fibril.

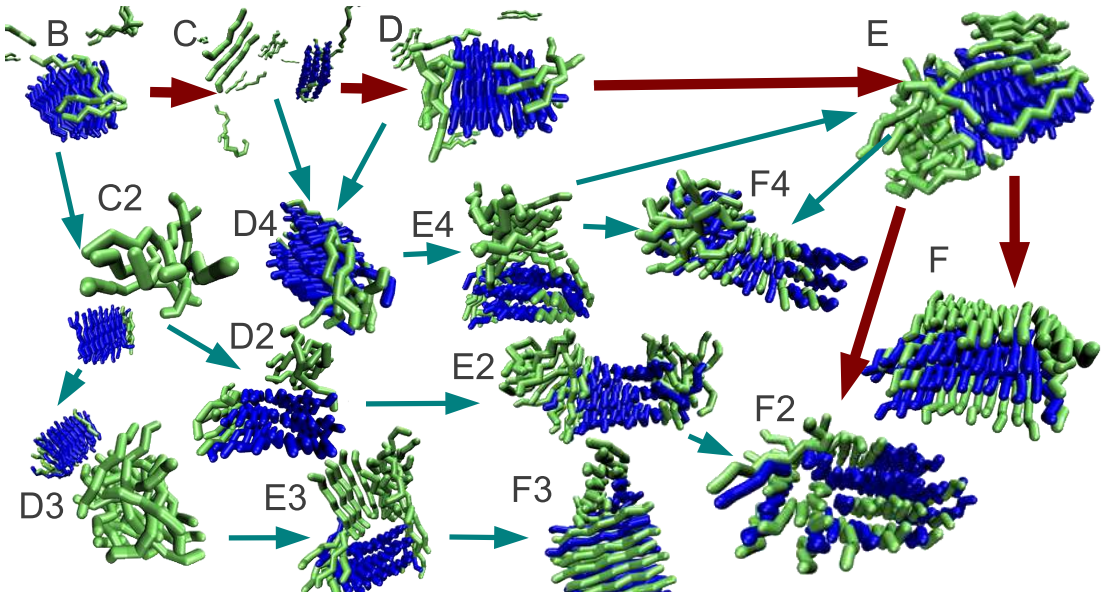

Figure 5.8: A fibrillar seed with free peptides of intermediate stiffness (K_χ = 1.50 kcal/mol). The morphologies are as follows: (B) the free peptides attach individually to the seed (typically through a dock-lock mechanism, though direct-lock is also possible); (C) the free peptides form small fibrils in the bulk; (D) the free oligomers attach to the seed; (E) all small fibrils have attached, but with mixed orientations; (F) a multi-layered aggregate forms with free peptides mostly on the top/bottom/ends, and not well-mixed; (F2) a β-barrel structure forms on the fibril; (D4) peptides continue to attach to the seed individually while smaller fibrils attach together to form medium-sized semi-fibrillar aggregates; (E4) the semi-fibrillar aggregates attach to the seed; (F4) a metastable amorphous blob forms on the combined aggregate; (C2) free peptides form disordered aggregates; (D2) disordered aggregates attach to the seed; (E2) free peptides form tangled masses at the ends of the seed fibril; (D3) a large amorphous aggregate forms from smaller ones in bulk; (E3) the free peptide aggregate becomes semi-fibrillar as it attaches to the seed; (F3) a layer-plus-β-barrel structure forms.

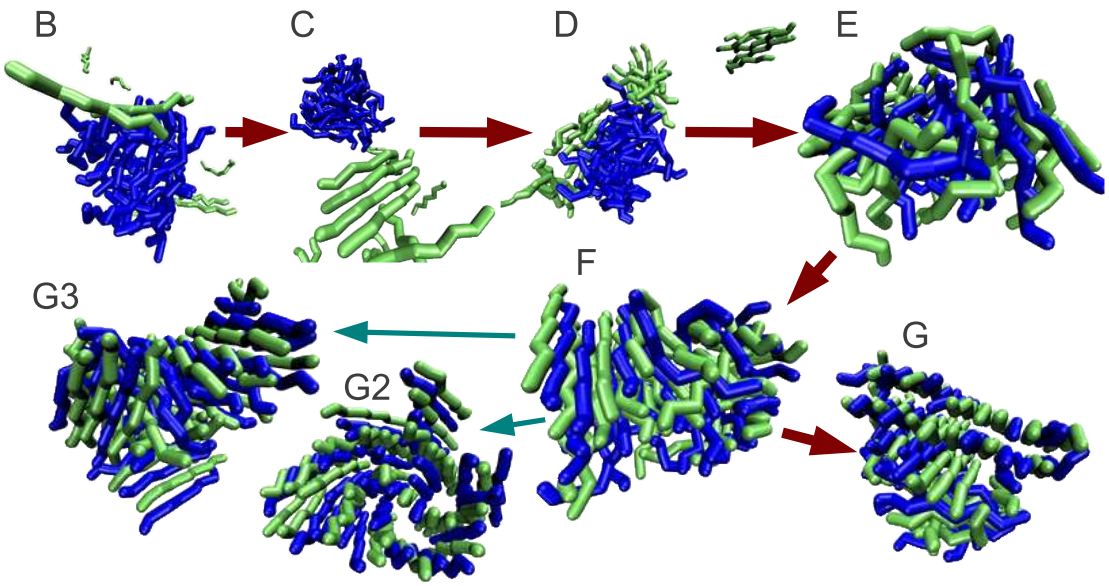

Figure 5.9: An amorphous seed with rigid ($K_\chi = 2$ kcal/mol) free peptides. The morphologies are as follows: (B) the free peptides attach individually to the seed; (C) the free peptides form small fibrils; (D) the free aggregates attach onto the seed; (E) the free peptides quickly embed themselves into the amorphous seed; (F) the free peptides begin to organize into fibrils, causing seed peptides to do the same; (G) a well-mixed multi-layer fibril forms, though amorphous structures are still present; (G2) β-barrel structures begin to form in the combined aggregate; (G3) the combined fibrillar aggregate contorts.

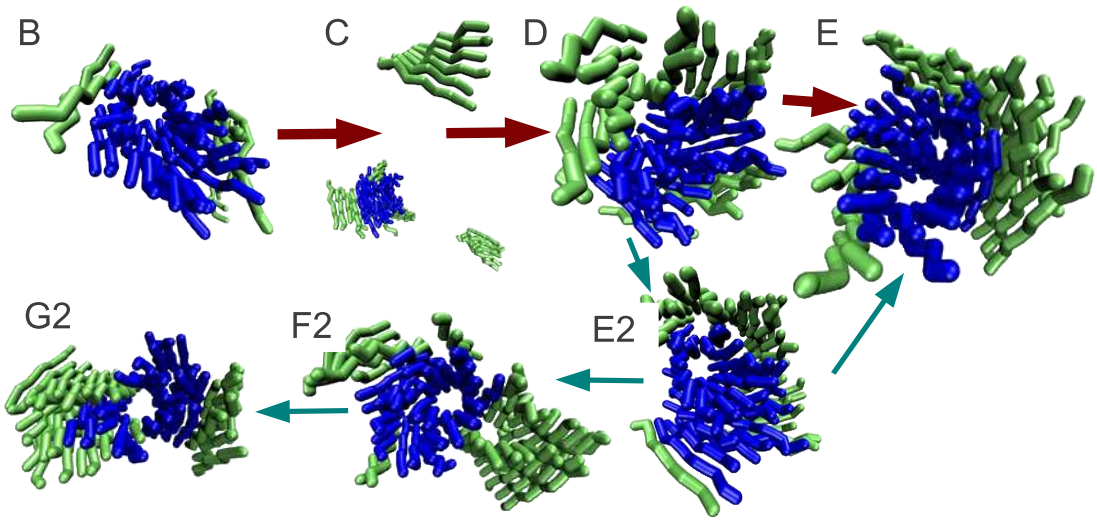

Figure 5.10: A β-barrel seed with rigid ($K_\chi = 2$ kcal/mol) free peptides. The morphologies are as follows: (B) the free peptides attach individually to the seed by a direct-lock mechanism; (C) the free peptides form fibrillar oligomers; (D) fibrils attach to the β-barrel seed with varying alignments; (E) most fibrils align to the seed, forming a new layer on the outside of the β-barrel; (E2) the free peptides begin to form additional β-barrel structures with the seed; (F2) additional β-barrel structures collapse into double layers; and (G2) the original β-barrel seed partially disrupted to form a multi-layered fibril with the free peptides, and some free peptides form an additional fibrillar layer on the outside of the β-barrel.

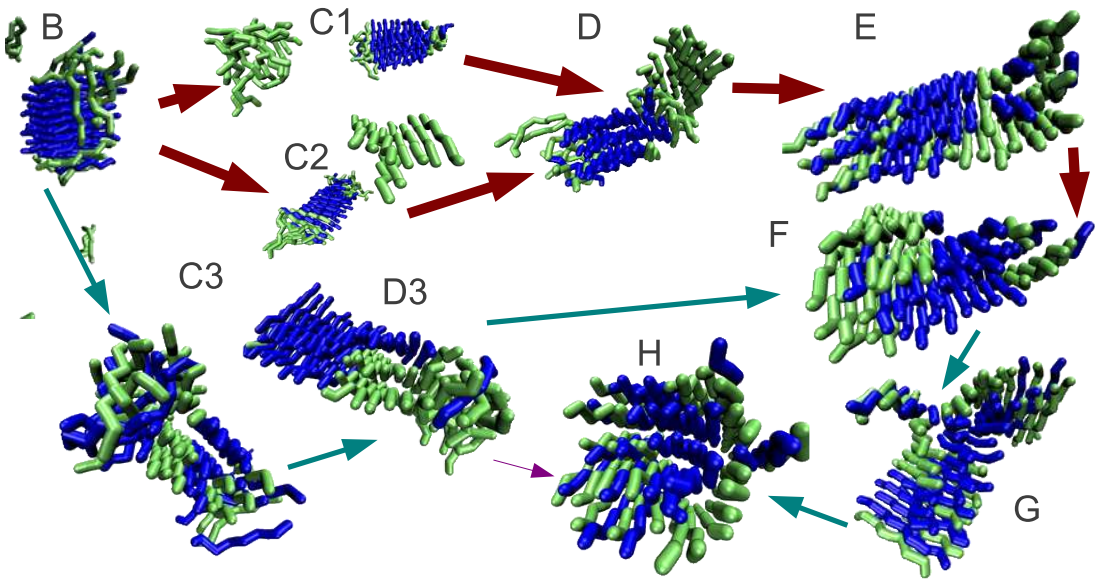

Figure 5.11: A fibrillar seed with free peptides of intermediate stiffness (K_χ = 1.25 kcal/mol). The morphologies are as follows: (B) the free peptides attach individually to the seed through a dock-lock mechanism; (C1) the free peptides form small amorphous aggregates in the bulk; (C2) the free peptides form a small fibrillar aggregates in the bulk; (D) the free oligomers attach to the seed; (E) the combined aggregate forms a moderately mixed multi-layered fibril; (F) fibrillar layers shift to form higher layers; (G) fibrillar layers split apart and fold back; (H) the combined aggregate forms a reticulated fibril; (C3) attached free peptides fray the fibrillar seed; and (D3) the combined aggregate forms a multi-layered fibril with amorphous portion at the end.

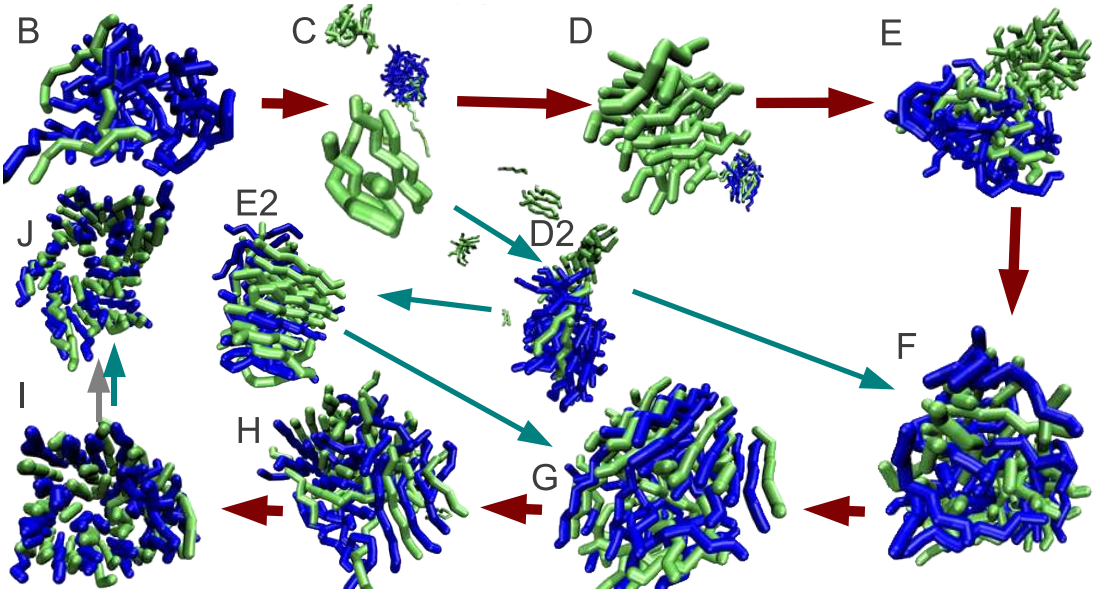

Figure 5.12: An amorphous seed with free peptides of intermediate stiffness (K_χ = 1.50 kcal/mol). The morphologies are as follows: (B) the free peptides attach individually to the seed; (C) the free peptides form partially-ordered oligomers in the bulk; (D) the free peptide oligomers combine to form a larger, partially-ordered aggregate; (E) a large free aggregate attaches to the seed; (F) the free peptides absorbed into seed; (G) the combined aggregate begins to order; (H) significant fibrillar structures become visible in the combined aggregate; (I) a β-barrel begins to form out of fibrillar structures; (J) a significant β-barrel forms; (D2) the smaller free peptide oligomers attach to the seed; and (E2) the seed begins to break down the fibrillar oligomers.

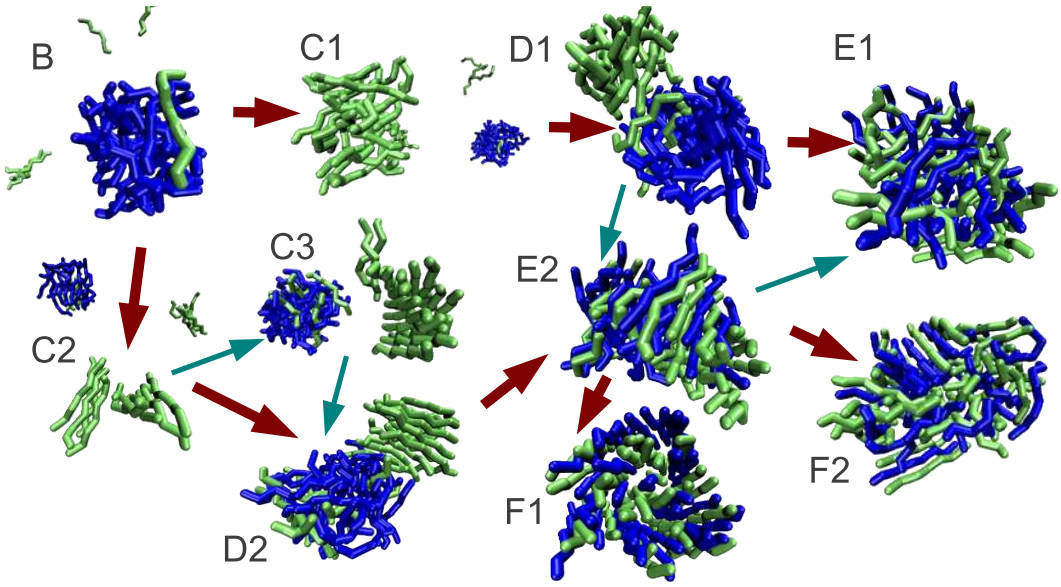

Figure 5.13: An amorphous seed with free peptides of intermediate stiffness (K_χ = 1.25 kcal/mol). The morphologies are as follows: (B) the free peptides attach individually to the seed; (C1) the free peptides form large disordered aggregates in the bulk; (D1) the free peptide aggregates attach to the seed; (E1) the free peptides are absorbed into the amorphous aggregate; (C2) the free peptides form fibrillar oligomers in the bulk; (C3) the free peptides form multi-layered fibrils; (D2) the free peptide fibrils attach to the seed; (E2) the free peptides and seed merge with considerable fibrillar order; (F1) system forms a β-barrel structure with β-sheet layers on the outside; and (F2) a tangled, semi-fibrillar combined aggregate forms.

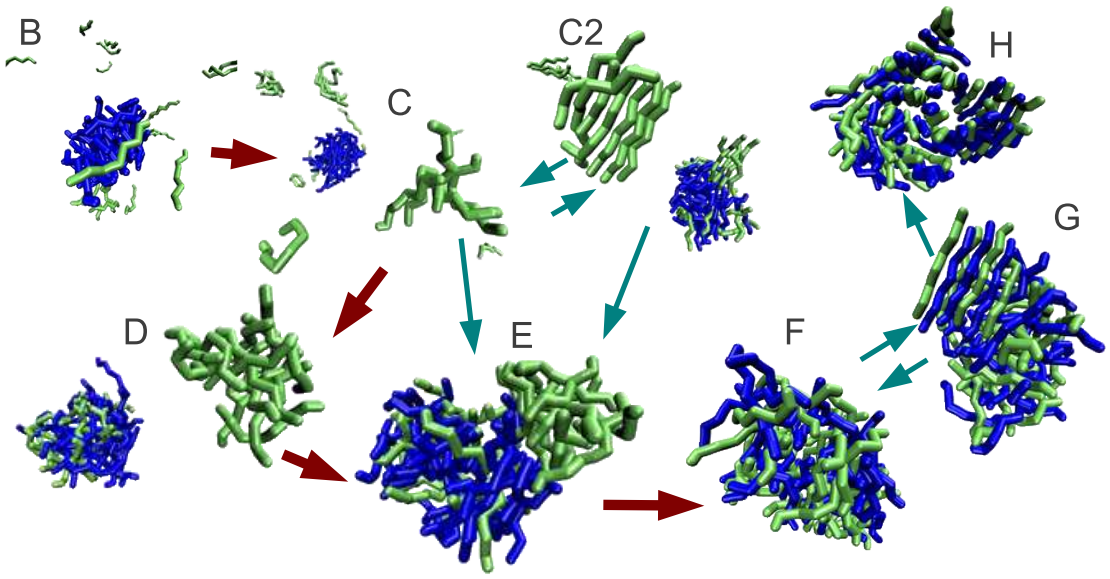

Figure 5.14: An amorphous seed with flexible free peptides ($K_\chi = 1.00$ kcal/mol). The morphologies are as follows: (B) the free peptides attach individually to the seed; (C) the free peptides form small disordered aggregates in the bulk; (C2) the free aggregates adopt a β-sheet structure; (D) the free peptide aggregates combine to form a larger amorphous aggregate; (E) the free peptide amorphous aggregate attaches to the seed; (F) the free aggregate and seed combine into a single disordered aggregate; (G) some fibrillar structure begins to emerge; and (H) the merged aggregate begins to adopt a partially-β-barrel structure.

Chapter 6

Kinetics of Peptide Aggregation on a Membrane

The aggregation of peptides on a lipid bilayer is studied using coarse-grained molecular dynamics in implicit solvent. We look at how the peptide aggregates and membrane surface mutually affect each other's structure and kinetics. The ability of proteins to aggregate on surfaces has been reported in several experimental studies. Proteins aggregate on both solid surfaces (such as nanoparticles, teflon, graphite, and mica) [163, 181, 184, 220] and biologically-inspired soft surfaces (lipid vesicles and lipid bilayers) [54, 221–226]. Interestingly, not only did aggregates form on surfaces at concentrations where bulk aggregation did not occur, but the mechanism of fibril formation (when compared to high concentration bulk aggregation) could differ. The degree of aggregation and the morphology of the aggregates depend critically on both protein sequence and surface characteristics [220, 227]. For instance, the Alzheimer Amyloid-β peptide (Aβ) formed twisted amyloid fibrils in the bulk, 5 nm high linear aggregates on hydrophilic mica, and 1 nm high sheets on hydrophobic graphite [184].

The aggregation of proteins on membranes is a particularly intriguing process [54, 125]. Membranes appear to recruit proteins and promote aggregation, but this very process can ultimately lead to membrane deformation or leakage. The ensuing cell death may be the basis of neurodegeneration observed in brain-related amyloid diseases. Proteins can interact with membranes in a variety of ways (electrostatic binding, non-specific adsorption, anchoring, or partial insertion), and different mechanisms of membrane damage have been proposed [228]. The first involves the embedding of monomers or small oligomers into membranes, creating gateless pores that leak out vital ions [229, 230]. This process has been observed most notably in the case of Aβ. The second mechanism involves the direct fibrillization of proteins on the membrane surface [136, 231, 232], which can damage the membrane [233], either through a physical distortion of the bilayer, or through a detergent effect in which growing aggregates recruit lipids, leading to membrane permeation. Fibrillization on the membrane can be initiated by a peptide or small oligomer binding to the membrane. An example of this is α-synuclein, which can bind to lipid head groups, thereby exposing its hydrophobic residues to solution for further aggregation [234]. The A53T α-synuclein mutant, on the other hand, inserts deeply into the membrane, burying its hydrophobic residues and preventing fibril assembly. Fibril growth on vesicles, and ensuing damage has been reported in TEM studies of hIAPP, in which large unimolecular vesicles (LUVs) were seen to distort when fibrils grew on the surface [136]. The vesicles remained intact when the non-amyloidogenic mIAPP was placed in solution with the vesicles. A mechanism was proposed in which the monomers of hIAPP adsorbed on, or partially inserted into, the surface. Interactions with free monomers or small oligomers in solution promoted aggregation on the surface. It was suggested that aggregation was favored by the increase in local peptide

concentration, and possibly aided by structural rearrangements of the peptides on the surface. In a similar vein, distortion of liposomes was observed in cryo-EM images in the presence of β2-microglobulin fibrils [232]. We note that the fibril and pore formation processes are not mutually exclusive. Some proteins, such as hIAPP, have been reported to form pores as well as damage membranes through fibrillization.

Simulations are a very useful complement to experimental studies in that they provide detailed information about the mechanism of protein adsorption, insertion, and aggregation on membranes. A range of simulations have been performed in recent years, using atomistic representations of proteins with explicit or implicit membrane surfaces, MARTINI models, as well as more coarse-grained models [133, 187, 193, 196, 198, 235–250].

Atomistic simulations provide the most detailed information about protein-membrane interactions, but because of high computational cost, they have been restricted to the study of monomeric or small oligomeric systems. Coarse-grained models, on the other hand, allow the study of much larger systems, over longer time scales [48, 60, 251, 252]. Here we use our intermediate resolution coarse-grained peptide model (Chapter 2). The mechanism of assembly into fibrils depended on the β-sheet propensity of the peptides, with low β-sheet propensity peptides forming amorphous aggregates, mid β-sheet propensity peptides forming fibrils via unstructured oligomer intermediates, and high β-sheet propensity peptides aggregating directly through ordered β-rich oligomers. Investigations of the assembly of these peptides on a solid surface (Chapters 3–5) showed that the solid surface gave a significant bias to the formation of β-sheet fibrillar aggregates.

In this chapter, we turn to aggregation on a lipid bilayer, a fluid surface of particular biological relevance. Our membrane model consists of five beads per

lipid, comprising a hydrophilic head, an interfacial bead, and a three-bead hydrophobic tail (see Chapter 2.2). The lipids spontaneously assemble into a bilayer with fluid and elastic properties consistent with experimental values. We contrast the mechanism of fibrillization on a solid surface to fibril formation on a membrane surface, and highlight how the fluid nature of the membrane leads to new fibril morphologies, and how these aggregates in turn affect the fluid/elastic properties of the membrane, including the experimentally relevant bending modulus [221, 231].

6.1 Methods

6.1.1 Simulations

We conducted two sets of simulations: the first to study the kinetics of peptide aggregation on the membrane, and the second to study the effects of bound peptide aggregates on the membrane's elastic properties. In both sets Langevin dynamics held the temperature at $0.85E_0$, the temperature for which the membrane model was optimized. Recall from Chapter 2.2 that we use reduced units where $\sigma =$ 7.5Å and $E_0 = 0.6573$ kcal/mol. We use a time scale unit τ, corresponding to 3ps of coarse-grained simulation time. Note that dynamics run faster in coarse-grained time than they would in an all atom system with higher friction [253]. We use a time step of 0.005τ.

Aggregation Kinetics on a Membrane

In the first simulation set we used six combinations of parameters for peptide stiffness (flexible to stiff) and hydrophilic surface attraction (weak to strong): $K_\chi = 1.52$ or 3.04 E_0 and $\epsilon = 1.29, 1.52$, or 3.04 E_0. For each parameter set, we ran 64 simulations. Initial conditions have 35 peptides distributed randomly in the bulk above a membrane in a state randomly sampled from its fluctuations about equilibrium. Each lipid monolayer has 324 lipids. The system is contained in a box that is $(18.24\sigma)^2$ in the plane of the membrane, and 15.73σ high. Since the "reverse" side of the membrane is repulsive to the peptides and the average head-to-head membrane thickness is roughly 9σ, this gives an effective range of 7σ in the z dimension for the peptides to explore, an equivalent space to our previous work on a solid surface (Chapters 3–5). Note that we have conducted simulations in both the constant volume and zero surface tension ensemble and do not find

differences in the dominant aggregation kinetics.

We ran each of these simulations for a time of $275 \cdot 10^3\tau$, observing the kinetics of peptide aggregation and binding to the membrane surface.

Effect of Peptide Aggregates on Membrane Elastic Properties

For our second simulation set we analyzed the effect of membrane-bound fibrils on the elastic properties of the lipid bilayer. The membrane-peptide system was held at zero average surface tension. We initialized the system with 9 fibrillar peptide aggregates formed on each side of the membrane (a total of 18 fibrils). We use a strong surface attraction ($\epsilon = 3.04\ E_0$) and stiff peptides ($K_\chi = 3.04\ E_0$). For this section, our analysis assumes a symmetry between the top and bottom membrane leaflet. Peptides in different fibrils experienced repulsive potentials so that the fibrils spread out across the membrane instead of merging. This gives homogeneity across the surface. We looked at three such systems, where the fibrils were 4, 8, and 16 peptides in length. Thus the systems contained 72, 144, and 288 peptides in total. Each of these systems contained a bilayer comprising 3200 lipids. For comparison, we conducted an identical simulation containing only the lipid bilayer and no peptides. We identify these four systems with the number of peptides per fibril: 0, 4, 8, and 16, respectively making up a 0, 2.5, 5.0, and 10.0% area fraction of the membrane. Each system had 6 runs, each run $500 \cdot 10^3\tau$, with a $170 \cdot 10^3\tau$ equilibration time before each run.

6.1.2 Order Parameters for Peptides and Membrane

For our analysis we are concerned with three order parameters involving the peptides. These parameters are also used in Chapters 3 and 4.

We define the peptide height (z) as the difference between the mean z coordinate of all the peptides' hydrophilic residues and the mean z coordinate of the upper leaflet's head groups at a given time. It is a measure of how unbound the peptides are from the membrane surface.

The number of fibrillar contacts (C_1) is a measure of the degree to which peptides form fibrils. For each pair of adjacent peptides where no X interaction center on one peptide is farther than 0.47σ from an X interaction center on the other, one contact is counted. That is, it counts the pairs of peptides that are connected in the same fibril.

The peptide orientation (Q) is a measure of peptide alignment. It is normalized to 1 when all peptides are in a parallel (or anti-parallel) alignment, and equals 0 when their orientations are uncorrelated. See Eq. 3.1 for the functional form of Q.

We consider the same set of membrane properties introduced in prior work [148, 149], which give a description of both overall membrane shape and orientation of the lipids within the membrane. These properties are discussed and theoretically motivated in other work [148]; the presentation here is limited to defining the properties that are reported later in this chapter. Membrane shape is quantified by extracting the height fields of the two monolayers, $h^{(1)}(x, y)$ and $h^{(2)}(x, y)$, and lipid orientation is quantified by extracting the head-to-tail director vector fields of the two monolayers, $\mathbb{n}^{(1)}$ and $\mathbb{n}^{(2)}$ as diagrammed in Fig. 6.1. In previous work [148, 149] Watson et al. demonstrated that the theoretical predictions for *homogeneous* lipid bilayers are considerably simplified by looking at linear combinations of these observables and focusing only on the xy components of the lipid directors. Although we have few theoretical predictions for the behavior of the inhomogeneous peptide-lipid systems studied here, we retain the

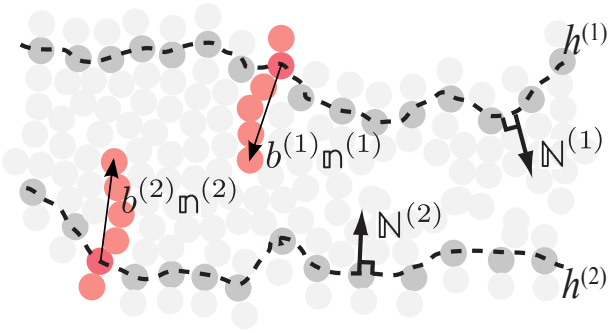

Figure 6.1: A cartoon depicting the quantities directly extracted from simulation to obtain the membrane height (h), thickness (t), and lipid tilt vectors ($\bar{\boldsymbol{p}}$, $\hat{\boldsymbol{p}}$) discussed in the text. The simulation box is oriented such that the lipid bilayer spans the xy plane. The monolayer height fields $h^{(1,2)}(x, y)$ (dashed lines) describe the shape of the two leaflets as defined by the positions of the lipid interface beads (dark gray circles). The monolayer director vector fields $\mathbb{n}^{(1,2)}(x, y)$ are unit vectors pointing from the interface bead to terminal tail bead along the same lipid (shown in red); the lipid lengths $b^{(1,2)}(x, y)$ are the distance associated with this vector if it were not normalized. $\mathbb{N}^{(1,2)}(x, y)$ are the unit vector fields normal to the monolayer height fields. These fields are extracted from simulation data that involves unevenly spaced discrete points in the xy plane (i.e., the xy coordinates of the interface beads) via a real-space grid procedure presented in detail in Appendix C of previous work [148].

combinations introduced previously in order to facilitate comparison to control simulations involving only lipids.

We retain only the xy components of the 3D vectors defined in Fig. 6.1, $\mathbb{n}^{(1,2)}(x, y)$ and $\mathbb{N}^{(1,2)}(x, y)$, and write these 2D projected vectors as $\boldsymbol{n}^{(1,2)}(x, y)$ and $\boldsymbol{N}^{(1,2)}(x, y)$, respectively. The monolayer tilt vectors, which quantify lipid orientation relative to the local surface normal, are defined as

$$\boldsymbol{p}^{(1,2)}(x, y) = \boldsymbol{n}^{(1,2)}(x, y) - \boldsymbol{N}^{(1,2)}(x, y). \tag{6.1}$$

The quantities presented in the results section include the second moments of the

Fourier-space versions of the following fields

$$h(x,y) = \frac{h^{(1)}(x,y) + h^{(2)}(x,y)}{2} \tag{6.2}$$

$$t(x,y) = \frac{h^{(1)}(x,y) - h^{(2)}(x,y) - 2t_0}{2} \tag{6.3}$$

$$\bar{\boldsymbol{p}}(x,y) = \frac{\boldsymbol{p}^{(1)}(x,y) + \boldsymbol{p}^{(2)}(x,y)}{2} \tag{6.4}$$

$$\hat{\boldsymbol{p}}(x,y) = \frac{\boldsymbol{p}^{(1)}(x,y) - \boldsymbol{p}^{(2)}(x,y)}{2} \tag{6.5}$$

These four quantities represent the overall bilayer shape (h), half bilayer thickness (t), and the symmetric and antisymmetric contributions of lipid tilting across the two leaflets ($\bar{\boldsymbol{p}}$, $\hat{\boldsymbol{p}}$). Note that the thickness is measured relative to the average thickness, t_0, so that this quantity, like the other membrane properties, has zero mean.

6.2 Results

6.3 Aggregation on a Fluid Membrane Induces Different Structures than on a Solid Surfacee

Constant temperature molecular dynamics simulations of initially disassembled peptides in the presence of the membrane were performed as described in the methods section. Simulations involved peptides with different backbone stiffnesses K_χ (β-sheet propensities) and with different interaction strengths ϵ between hydrophilic beads and membrane head groups. Both the aggregation pathways and the structures of the aggregates were monitored.

To describe aggregate structures we adopt a notation of a letter and a number, the letter to describe the aggregate type and a number to indicate how it is bound to the surface. The letter convention is: P = individual, unaggregated peptides; A = amorphous aggregates; F = fibrillar aggregates; and B = β-barrel aggregates. Subscripts are: 0 = in the bulk; 1 = bound directly to the membrane; 2 = bound onto a fibrillar bottom layer; and generally $n + 1$ = bound to an n structure. Images of these structures are shown in Fig. 6.2.

Fig. 6.2 depicts observed structures of peptides aggregating on a lipid membrane and marks the pathways where the peptides may transition from one structure to another. Thicker, colored arrows denote pathways which are characteristic of (but not exclusive to) a flexible peptide backbone, a stiff peptide backbone, or a high surface attraction. A high surface attraction trumps the effect of peptide backbone stiffness. Fig. 6.3 shows the probability of observing each pathway in

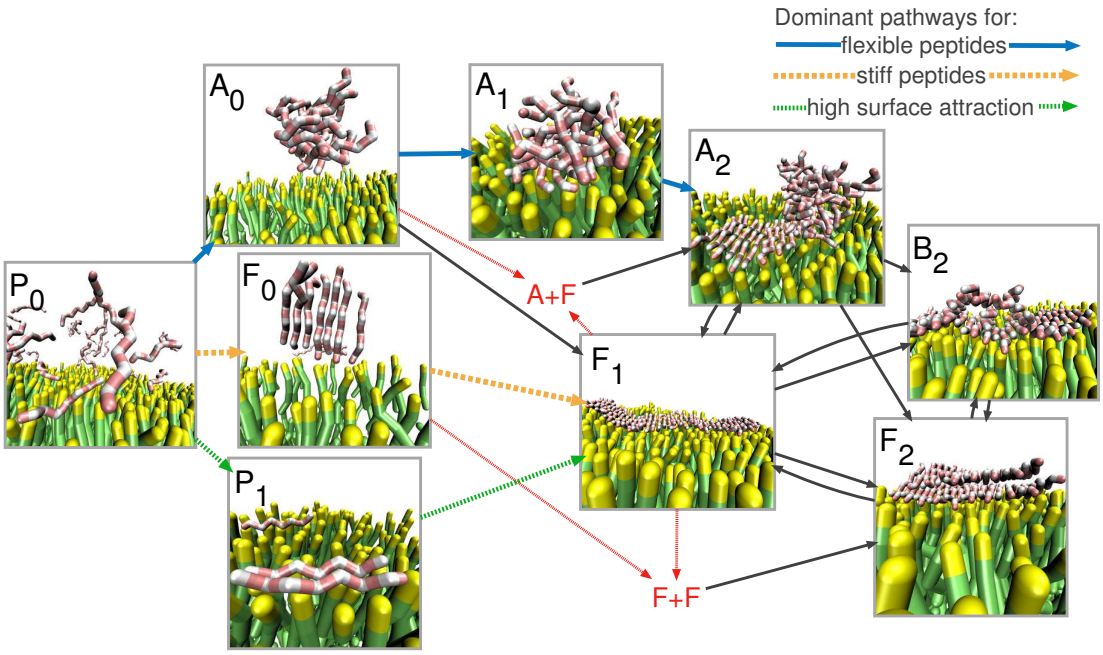

Figure 6.2: A map of the dominant kinetic pathways. Naming convention: P = individual, unaggregated peptides; A = amorphous aggregates; F = fibrillar aggregates; and B = β-barrel aggregates. Subscripts: 0 = in the bulk; 1 = bound directly to the membrane; 2 = bound onto a fibrillar bottom layer. A+F occurs when an A_0 structure lands on an F_1 to form an A_2; F+F occurs when an F_0 structure lands on an F_1 to form an F_2. Pathways characteristic of stiff or flexible peptides, or of strong surface attractions are marked in the diagram's legend.

Fig. 6.2 averaged over 64 simulations, while Fig. 6.4 shows the probability of a particular structure being present at the end of the simulation ($t = 275 \cdot 10^3 \tau$).

Earlier, in Chapters 3 and 4, we studied the aggregation of these peptides in the bulk and in the presence of a solid surface. The most flexible peptide ($K_\chi = 1.52E_0$) formed primarily amorphous aggregates in the bulk, while the more rigid peptide ($K_\chi = 13.04E_0$) formed multi-layered fibrils. The presence of a solid surface dramatically altered the conformations of the aggregates, particularly in the case of the more flexible peptides, favoring the formation of β-sheet fibrils

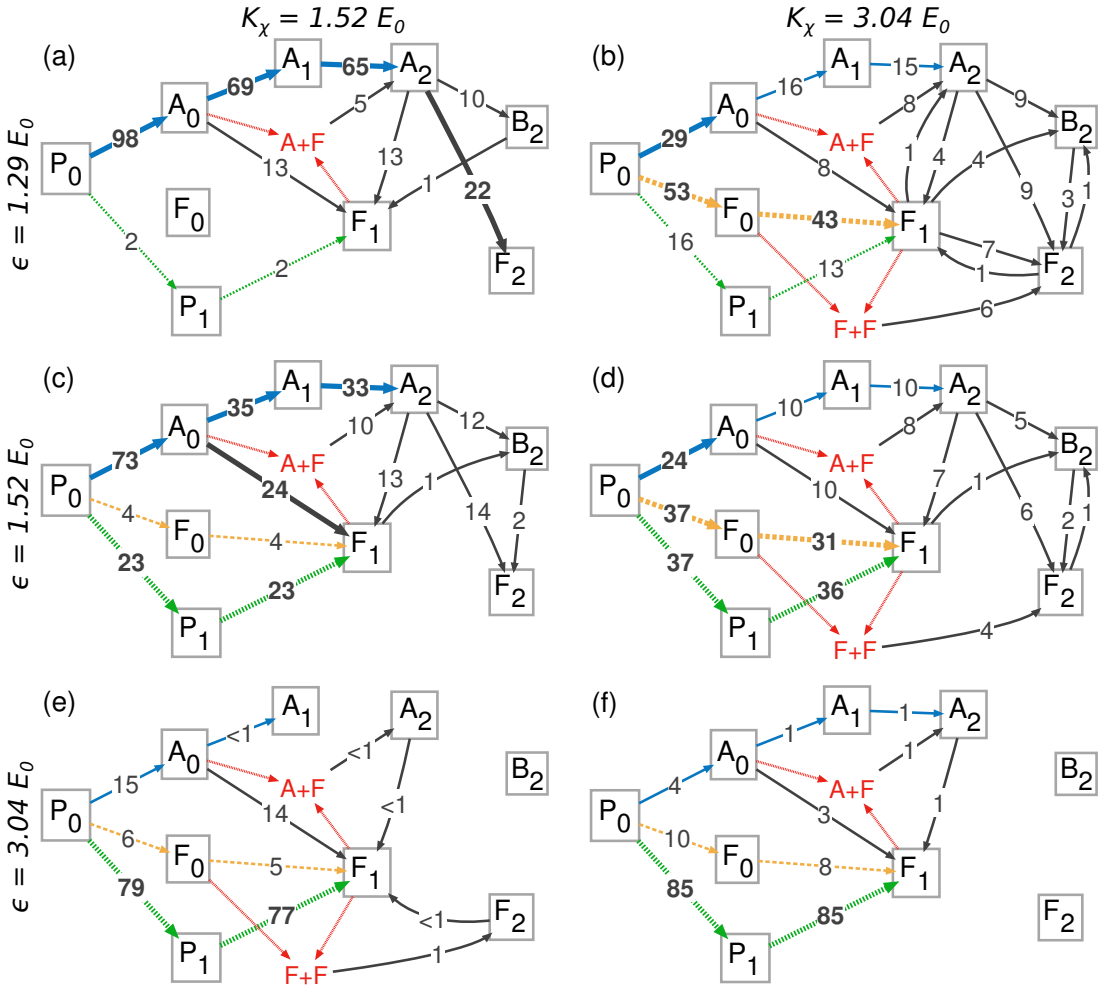

Figure 6.3: The probability (out of 100) of observing each transition during the course of a simulation, weighted by the number of peptides involved in the transition. Compare to Fig. 6.2. The probabilities are averaged over all simulations at the given values of K_χ and ϵ. The left column is for flexible dihedrals ($K_\chi = 1.52E_0$), and the right column is for rigid dihedrals ($K_\chi = 3.04E_0$). The rows are, descending, $\epsilon = 1.29, 1.52$, and 3.04 E_0 (weak to strong attraction). Dominant pathways for each system have been bolded.

on the surface. The membrane studied here has an equally important effect on the formation of aggregates.

Compared to peptide aggregation on a solid surface, aggregation of our pep-

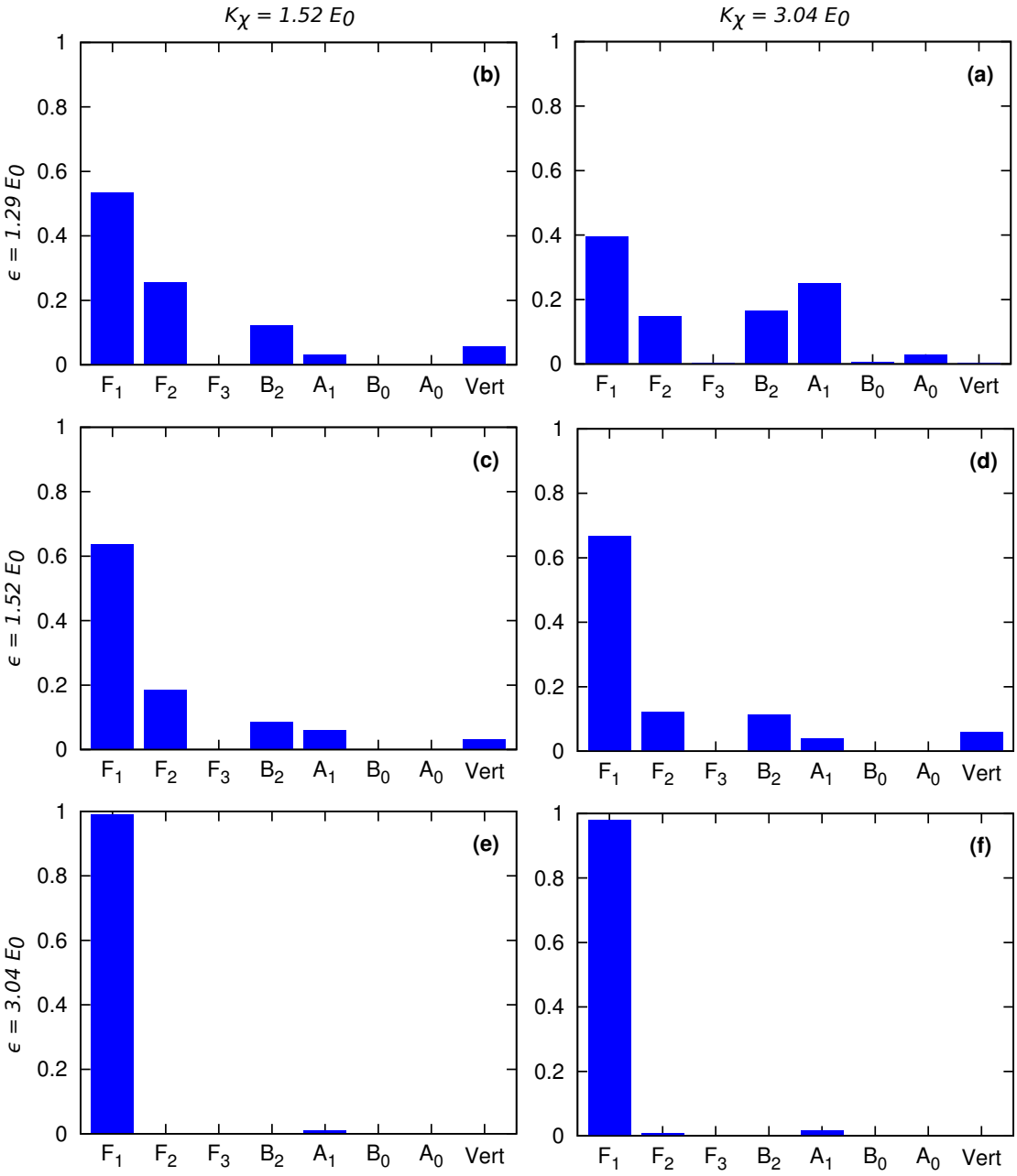

Figure 6.4: Probability of observing a given structure at the end of a kinetic simulation, weighted by the number of peptides composing the structure. The probability is averaged over all simulations. Structures are defined in Fig. 6.2, except for "Vert", which refers to a small, vertical fibril orthogonal to the bound fibril (see Fig. 6.5 (a)). F_3 is a bound triple-layer.

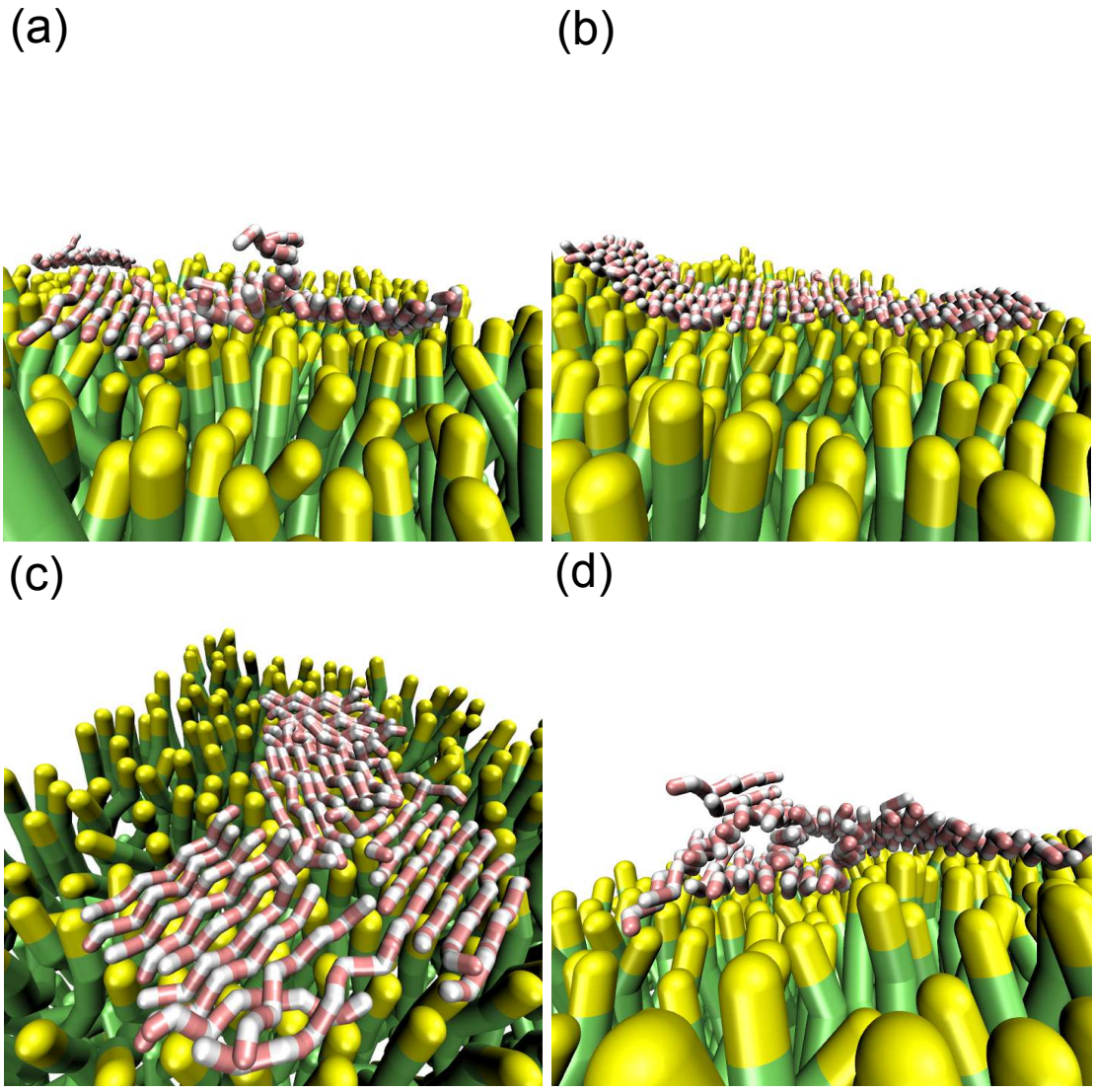

Figure 6.5: Additional structures observed in the simulations. Panel (a) depicts a vertical fibril attached to an F_1 bound fibril, but orthogonal to it. Panel (b) depicts the undulations that the membrane induces in an F_1 fibril. Panel (c) depicts the frequent way F_1 fibrils do not align on the membrane, but instead jam together. Panel (d) depics a β-barrel aggregate bound to the surface, a morphology found to be significantly more common to an undulating membrane than a solid surface.

tide model on a lipid membrane exhibits a number of similarities and differences.

Starting with similarities, the initial deposition of aggregates onto the membrane is highly analogous to the initial deposition onto a solid surface. For low to

moderate surface attraction, the pathway is primarily determined by the peptide backbone stiffness. Stiff peptides readily form fibrils in the bulk and deposit directly as a single layer onto the surface; flexible peptides form disordered oligomers that land on the surface while the peptides closest to the surface spontaneously rearrange into a fibril via a nucleation mechanism. For a strong surface attraction, peptides are not given time to aggregate, instead depositing immediately onto the surface, where they diffuse and come into contact with other deposited peptides and begin to form a fibrillar layer. In this case, the membrane actively remodels the structure of each flexible peptide individually from its monomeric bent shape to an extended aggregate-prone conformation, sometimes referred to as an N^* conformation [59], on the surface. This pathway for a strong surface attraction in particular is essentially identical to the pathway on a solid surface ($P_0 \rightarrow P_1 \rightarrow F_1$, seen in Fig. 6.3 (e) and (f)).

Another similarity is the general bias of strong surface attraction to structures maximizing contact between the peptides and the lipid head groups (namely F_1 structures), as seen in Fig. 6.4. Structures more weakly bound to the surface (in this case A_2, B_2, and F_2) appear predominantly in low and moderate surface attractions.

The most significant difference we observe is in the allowed/disallowed structures on a lipid membrane compared to a solid surface. For example, the β-barrel on the membrane (B_2) replaces the triple-layered fibril on the solid surface (F_3) as the primary weakly bound β-sheet structure (Fig. 6.5 (d)). The rarity of F_3 structures on the membrane is partly a result of the fact that the lipid head groups interact with the hydrophilic residues of the peptide, while the solid surface previously considered interacted with the hydrophobic peptide beads. This means that on the membrane the third layer is formed by hydrophilic-hydrophilic

contacts instead of the stronger hydrophobic-hydrophobic contacts on the solid surface. However, the prevalence of β-barrel structures on a fluid membrane and their scarcity on a solid surface suggest that it is the membrane itself which encourages β-barrel structures. Instead of stacking into even, flat layers, membrane undulations kick the peptides up, turning upper layers into β-barrels. Note that β-barrels form *after* landing on the membrane, not in the bulk. Our simulations cannot unambiguously determine if these structures are present in equilibrium, but they are at the very least a long-lived kinetically trapped state.

The vertical mini-fibril is a structure uniquely observed on the membrane, seen in Fig. 6.5 (a), which also results from membrane undulations kicking up peptides from a fibril. We can clearly see the bottom layer of this fibril conforming to these undulations in (a) and (b).

A peculiarity of aggregation on solid surfaces discussed in Chapter 4 is the alignment of the bound fibrils to directions determined by the crystallographic symmetry of the surface, also seen experimentally [181]. In this section, using a lipid membrane, the surface is fluid and therefore has no crystallographic symmetry, and no preferred directions of fibril formation. Thus while on the solid surface fibrils quickly aligned and merged, on the membrane they do not. Instead, they tend to squeeze together without aligning, as in Fig. 6.5 (c). These sort of jams did not appear on the solid surface.

6.4 Cooperativity of Peptide Binding and Aggregation Seen on Solid Surface Absent in the Presence of a Membrane

For aggregation on a membrane, an analysis of the equilibration of height, fibrillar contacts, and orientation over time shows behavior distinct from aggregation on a solid surface.

On the solid surface, order parameters associated with fibrillar aggregation and order parameters associated with peptide binding equilibrated at the same rate at the highest surface attraction with stiff peptides (5000τ relaxation time). This is not the case with the membrane. Peptide binding (z) has a 6300τ decay time for this system, but the number of fibrillar contacts (C_0) has a 17000τ decay time, and the orientation (Q) a 35000τ decay time.

Thus the cooperativity between fibril formation and aggregate binding, observed for on a solid surface, is not exhibited on the membrane. The trend of convergence of time scales is still present, though not to such a degree. At the lowest energy parameter set (weakly attractive surface with flexible peptides) orientation relaxation takes roughly 500% longer than binding, while at the highest energy parameter set (strongly attractive surface with stiff peptides) the increase is reduced to 450%, which is not a dramatic reduction. It is interesting that for the highest energy parameter set this discrepancy between a fluid membrane and a solid surface exists despite the final state (F_1) and the pathway the aggregates take to reach it (P_0-P_1-F_1) being qualitatively identical.

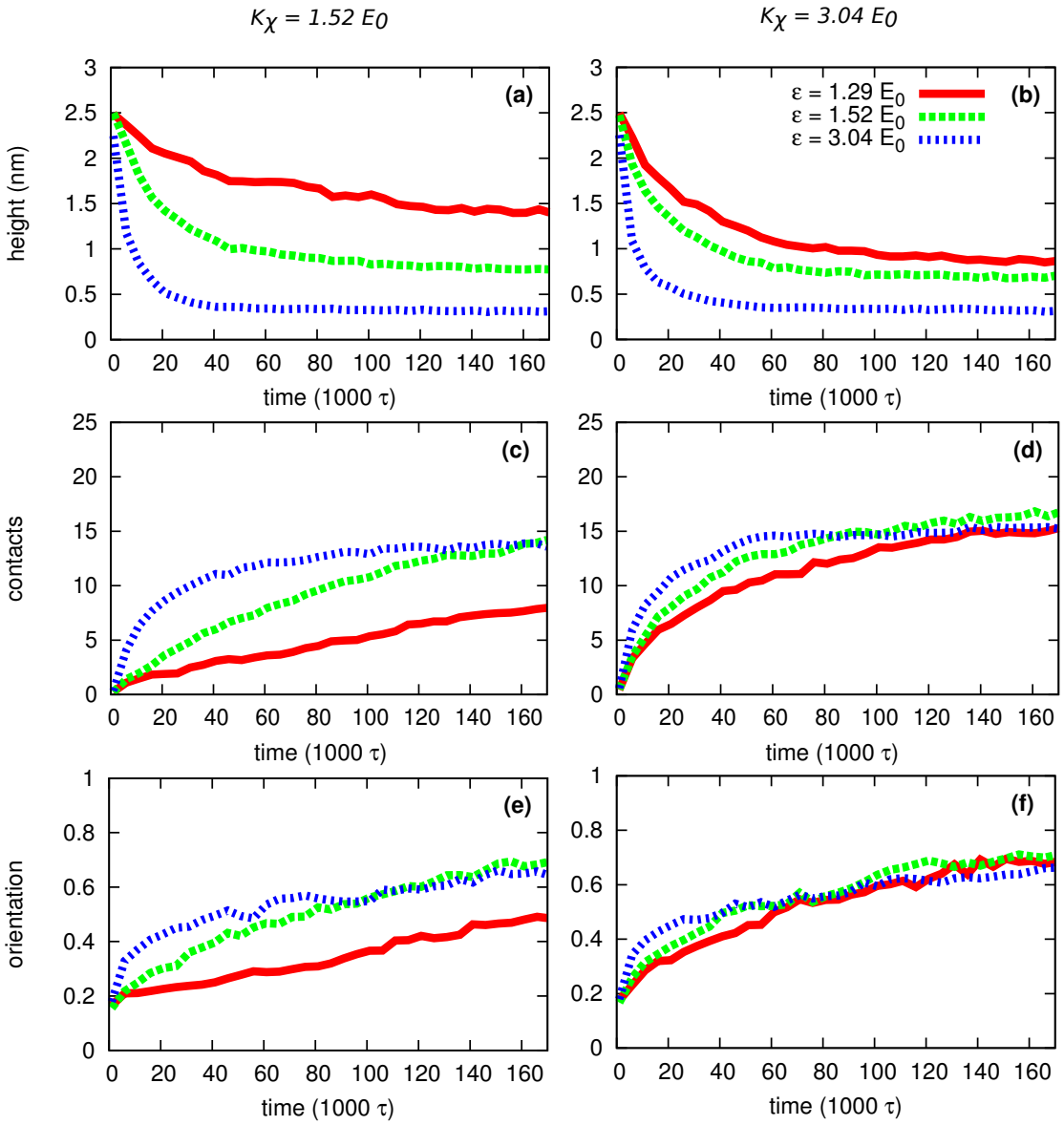

Figure 6.6: Depicts three aggregation order parameters (see methods section) versus time. The three data sets in each panel represent varying surface attractions. A legend for all panels is shown in panel (b). The left column is for flexible dihedrals ($K_\chi = 1.52E_0$), and the right column is for rigid dihedrals ($K_\chi = 3.04E_0$). The rows represent the different order parameters: height (z), contacts (C_1), and orientation (Q).

There are two reasons why on a fluid membrane fibrillar alignment is much slower than binding. First, the diffusion time scale is a bottleneck for fibrillar alignment. This was not the case on a solid surface: the ordered pattern of the surface enforced fibrillar alignment, speeding this process drastically. Second, membrane fluctuations disrupt fibrillar structures, so they take longer to form.

At lower surface attraction on a solid surface, the difference in orientation relaxation rate for stiff and flexible peptides is small. On a membrane, however, increasing the stiffness considerably decreases the relaxation time from 338000τ to 84000τ. Similarly, the binding relaxation time is decreased from 56000τ to 30000τ and the fibrillar contact formation time from 235000τ to 54000τ. This is consistent with the general trend that on a fluid membrane the surface attraction is far less dominant in determining pathway than on a solid surface. As expected, systems with a higher β-sheet propensity from fibrillar structures faster, and bind more quickly to the membrane.

It is interesting to observe that a decrease in the time scale of fibrillar contact formation does not necessarily result in a greater number of fibrillar contacts at the end of the simulation (see Fig. 6.6 (d)). At high surface attractions the fluid membrane is more prone to "jams" (Fig. 6.5 (c)), whereas a solid surface guides the fibrils to form along lines of crystal symmetry, maximizing the number of fibrillar contacts. At a lower surface attraction, though the contacts form more slowly, peptides have a greater chance to aggregate in the bulk before reaching the surface, which maximizes fibril size.

6.5 Peptide Aggregates Damp Thermal Membrane Fluctuations and Slightly Increase Membrane Bending Rigidity

A suggested mechanism of cell death resulting from aggregation is a deformation of the membrane by the growing aggregates. Indeed, TEM and Cryo-EM studies show significant distortion of vesicles when fibrils grow on their surfaces. It is also known that amyloid formation (but not single Aβ monomers) lowers membrane fluidity [226], and a computational study showed that even a single Aβ monomer perturbed lipid ordering [235].

Here, we examine how small fibrillar aggregates can affect membrane material properties and long-wavelength fluctuations. We performed simulations, as described in the methods section, in which we bound 18 (or zero) fibrillar peptide aggregates distributed over both sides of a 3200-lipid membrane. We used three such systems with different fibril sizes: 4, 8, or 16 peptides, respectively taking up 2.5, 5.0, and 10.0% of the membrane area.

The most visible effect the fibrils have on the membrane is on lipid packing, as shown in Fig. 6.7. Fibrils cause the lipids directly under them to align into a regular lattice structure. This packing is driven by the attraction between hydrophilic residues and lipid head groups; the close-packing of the lipid head groups maximizes the number of lipids under the fibrils. Lipids beneath a fibril pack at a 60% higher density than they do in the free membrane. This effect is analogous to what was seen in Chapter 4 involving fibrils on a solid surface, where fibrils locked in a particular orientation relative to the crystal symmetry. In the membrane case, the fibrils force the surface into this optimal packing rather than

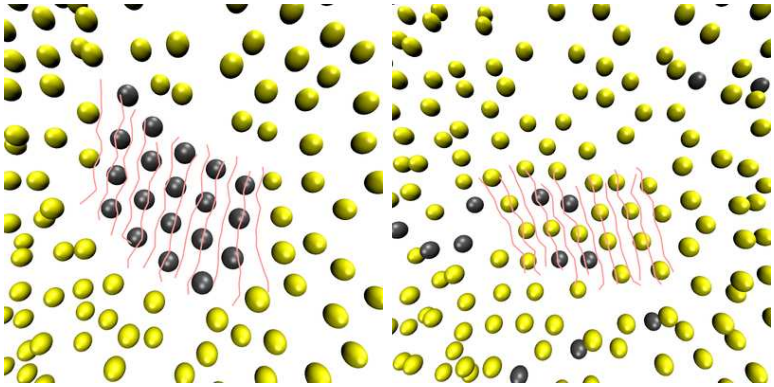

Figure 6.7: Local ordering of membrane head groups under a bound fibril. The original ordered head groups are colored black in the left panel, and the right panel shows the positions of these head groups at a time $24 \cdot 10^3 \tau$ later. Note that the right panel displays similar head group ordering as in the left, but the ordered lipids have exchanged with lipids from the surrounding disordered phase.

the surface reorienting the fibrils. On the membrane, this lattice structure quickly deteriorates away from the fibrils and does not seed a global phase transition of the bilayer (at least for the coverages and temperatures we have studied). These results are consistent with experimental evidence suggesting that amyloid proteins enhance lipid packing [231].

It is worth mentioning that although the lipids beneath fibrils temporarily adopt an ordered structure, these lipids rapidly exchange with those in the fluid phase. This exchange occurs on a time scale on the order of $10 \cdot 10^3 \tau$ (see Fig. 6.7). A weak effective attraction of fibrils through the bilayer is revealed by studying positional correlations across the two leaflets. For the system with the highest fibril coverage (10% coverage, with 16-peptide fibrils), the positional overlap of peptides between the top and bottom leaflets is statistically 3 times higher than expected for randomly distributed coverage (3% of the membrane area is sandwiched between fibrils in the top and bottom leaflets as opposed to the 1% expected if the two leaflets were completely independent). Since the peptides can not directly interact

across the bilayer, the interaction is lipid-mediated and is presumably related to the increased lipid packing density under the fibrils.

As introduced in the methods section, we have analyzed fluctuations in bilayer shape (h), bilayer thickness (t), and the lipid tilting ($\boldsymbol{p}$). These real-space fields are functions of the xy position on the membrane, but we employ a Fourier analysis because of the periodic geometry and translational invariance of the system. Further, theoretical predictions and a detailed simulation analysis exist [148] for the Fourier variables in the case of a homogeneous lipid bilayer (devoid of any fibrils) and it seems natural to adopt this convention here for comparison purposes. We use the following Fourier convention for an arbitrary function $g(x, y)$:

$$\begin{aligned} g_{\boldsymbol{q}} &= \frac{1}{L}\int_{L^2} g(x,y)e^{-i\boldsymbol{q}\cdot\boldsymbol{r}}dxdy \\ g(x,y) &= \frac{1}{L}\sum_{\boldsymbol{q}} g_{\boldsymbol{q}}e^{i\boldsymbol{q}\cdot\boldsymbol{r}} \end{aligned} \tag{6.6}$$

with allowed $\boldsymbol{q}$ vectors $\boldsymbol{q} = 2\pi(n, m)/L$, where n and m are integers. The simulation box size is $L \times L$ and the integral in Eq. 6.6 covers the entire box. Fig. 6.8 displays the power spectra of the various membrane order parameters. The vector fields $\bar{\boldsymbol{p}}$ and $\hat{\boldsymbol{p}}$ have been decomposed into their longitudinal ($\parallel$, curl free) and transverse ($\perp$, divergence free) components.

Inspection of the plots of Fig. 6.8 reveals that the fibrils affect membrane behavior. The most visible effect is seen in the thickness fluctuations, where the fluctuations decrease with increasing fibril coverage. This is consistent with the fibril-induced lipid ordering and condensation seen in Fig. 6.7. The solid-like regions beneath the fibrils would be expected to exhibit a higher compressibility modulus than the surrounding regions and this would damp fluctuations in the area/lipid, and (via lipid volume incompressibility) reduce the fluctuations

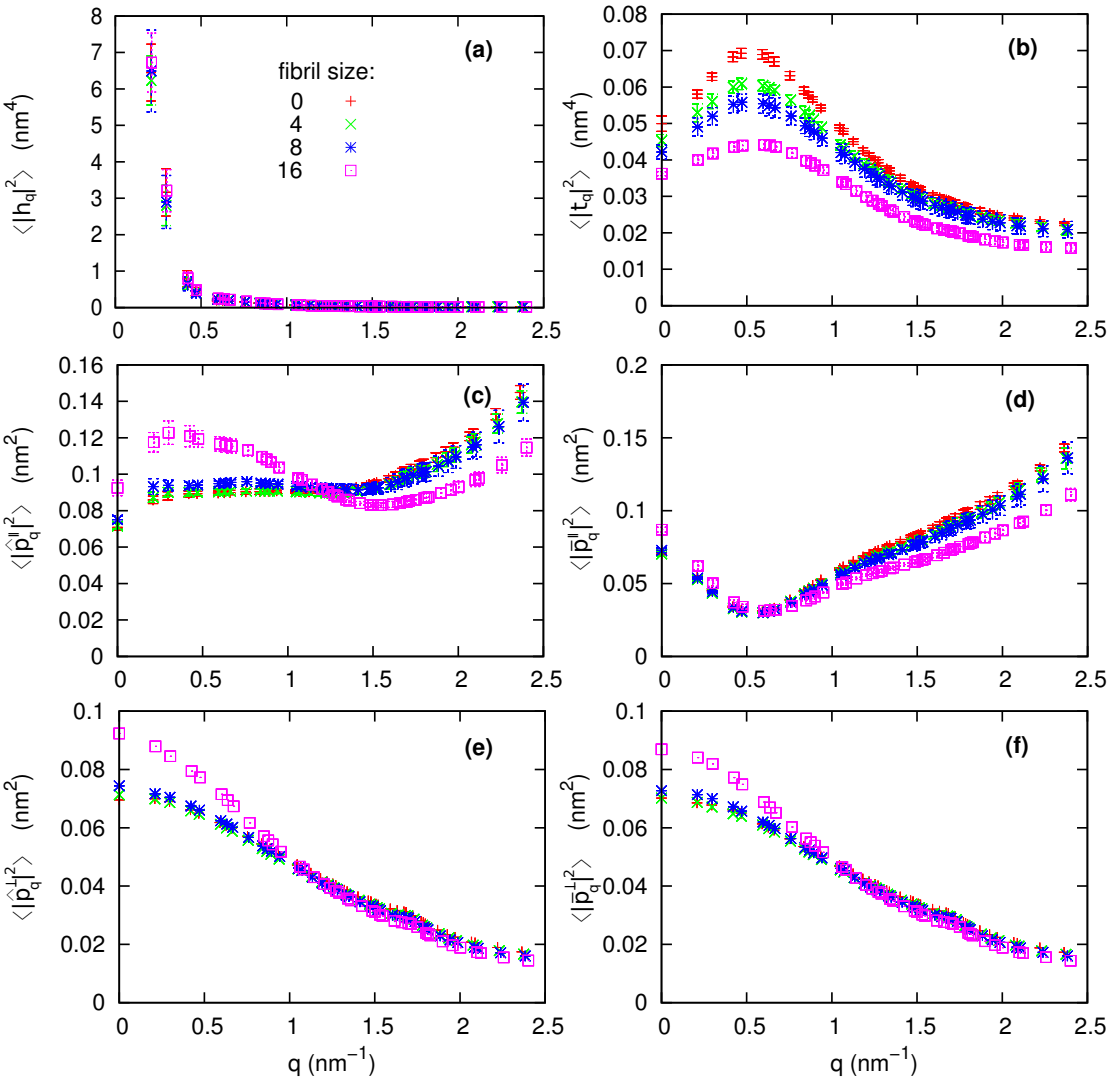

Figure 6.8: Power spectra for membrane observables as a function of the wavenumber, q. "Fibril coverage" indicates what fraction of the membrane area the fibrils occupy. Panel (a) depicts fluctuations in the membrane height, or undulations; (b) depicts the thickness, or peristaltic modes; (c)-(f) depict the four components of fluctuations lipid tilting (see methods section). Error bars for (e)-(f) are smaller than the symbols and are not explicitly indicated.

in bilayer thickness, just as our results suggest. The bilayer area compressibility modulus (as measured via area fluctuations of the simulation box [254]) increases approximately linearly with fibril area fraction: from $k_a = 17 \cdot 10^{-20} J/\text{nm}^2$ for

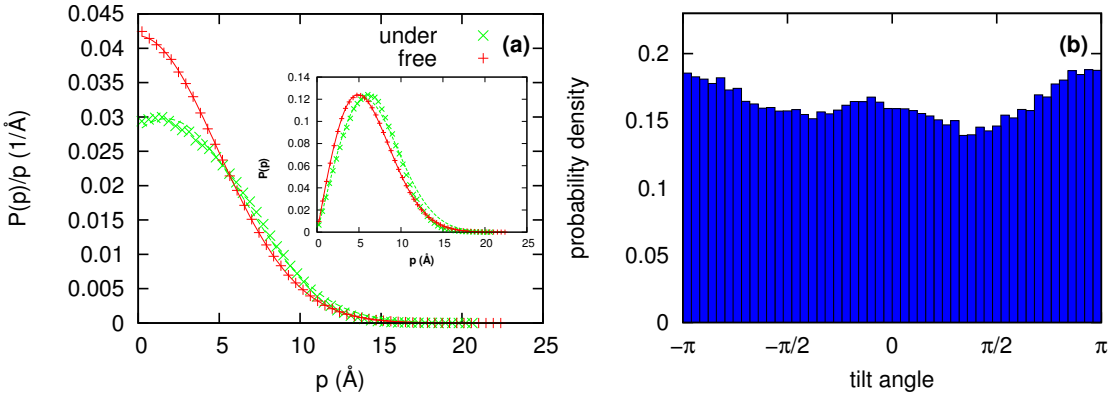

Figure 6.9: Panel (a) shows the probability density of lipid tilt magnitude, contrasting lipid tilt underneath the fibrils and the free lipid tilt in the bulk membrane. In the bulk membrane, this looks like $P(p) \propto p\exp(-cp^2)$, and underneath the fibrils $P(p) \propto p\exp(-c'(p-p_0)^2)$. We have determined $c = 0.0208\text{Å}^{-2}$, $c' = 0.0222\text{Å}^2$, and $p_0 = 1.7\text{Å}$. $P(p)$ is inset. Panel (b) depicts the orientation probability density of the angle a lipid tilt makes with its nearest peptide for all lipids underneath fibrils. The tilt angle is measured clockwise, looking into the membrane, with the peptide axis at 0.

the free membrane [148] to $k_a = 29 \cdot 10^{-20} J/\text{nm}^2$ at 10% coverage. On similar grounds, one might have naively expected the fluctuations in lipid tilt to decrease with increasing fibril coverage, however just the opposite trend is seen. In an effort to understand this effect, we analyzed the lipid tilt in real space and identified a correlation between lipid tilt and fibril position. The average length of the monolayer tilt vector $|\boldsymbol{p}^{(1,2)}|$ was found to be 6.5Å for fibril associated lipids, which is longer than that for non-associated lipids (6.1Å) by 6%. However, the fluctuations in tilt were found to be 6% smaller in regions beneath the fibrils than away from the fibrils. Further, the probability distribution for tilt magnitude is well approximated by assuming a harmonic potential energy function, with preferred orientation normal to the bilayer plane away from the fibrils and preferred orientation offset from normal under the fibrils (Fig. 6.9 (a)). The energetic cost for excursion from the preferred tilt magnitude is higher for the fibril associated

lipids than non-associated lipids. This data suggests that lipids underneath the fibrils have a tendency to align with each other in an orientation tilted away from the surface normal. The bias for a specific tilt direction relative to the fibril axis is slight (Fig. 6.9 (b)), but there is a small tendency for the lipids to align with the peptide axis, i.e., perpendicular to the axis of the fibril. We thus interpret the enhanced long-wavelength fluctuations of the tilt variables in Fig. 6.8 as resulting from the spatially varying local preferred tilt direction imposed by the fibrils. The short wavelength tilt fluctuations of the fibrillar systems are actually slightly diminished relative to the lipid-only case, which agrees with the observation that the local fluctuations in lipid tilt are reduced under the fibrils as the lipids locally align.

The preceding paragraph suggests that the physics associated with lipid tilting in the fibril-decorated case is qualitatively different from that for a homogeneous lipid system. It would be ill advised to attempt to interpret our tilt results within the theoretical framework of the free membrane [148], which presumes a homogeneous membrane surface. It may, however, be worthwhile to interpret the undulation data within this theory; over sufficiently long length-scales one would imagine that the membrane is behaving as a homogeneous sheet with effective elastic properties. Membrane height fluctuations are related to the membrane bending modulus, K_c [255, 256], as $q \to 0$ by the relation $\langle |h_{\mathbf{q}}|^2 \rangle \to k_B T / K_c q^4$, which provides a good fit to the long wavelength modes of our simulations over all considered fibril coverages. However, our $\langle |h_{\mathbf{q}}|^2 \rangle$ data shows no effect of fibrils on the low q modes of the membrane within the statistical uncertainty of the simulations. The implication is that the fibrils have a negligible effect on the bending rigidity of the composite membrane. This conclusion is consistent with the prediction for the expected effective bending modulus for a membrane with

area fraction ϕ of regions of enhanced rigidity [257, 258]:

$$\frac{1}{K_{Ceff}} = \frac{1-\phi}{K_C} + \frac{\phi}{K_{Cfib}}, \tag{6.7}$$

where K_C represents the bending modulus for a homogeneous lipid sheet, K_{Cfib} the bending modulus for the fibril covered regions and K_{Ceff} the effective bending modulus for the fibril-decorated sheet. Prior analyses of our lipid model suggest $K_C \sim 35 \cdot 10^{-20}$ J [148–150]. In the limiting case scenario involving absolutely rigid fibrillar regions ($K_{Cfib} = \infty$) at 10% coverage, Eq. 6.7 would predict $K_{Ceff} = 39 \cdot 10^{-20}$ J, which would be very difficult to distinguish from a bare membrane using the thermal fluctuation approach. At smaller area fractions and/or for less rigid fibrillar regions the effect is even smaller. Using the local bending rigidity analysis technique of Khelashvili et. al. [259], we were able to estimate $K_C = 32 \cdot 10^{-20}$ J and $K_{Cfib} = 45 \cdot 10^{-20}$ J, which leads to $K_{eff} = 33 \cdot 10^{-20}$ J at 10% fibril coverage. Such a small change in bending rigidity is not expected to be observable in the undulation spectrum. So, despite the fact that fibrillar regions exhibit bending stiffness $\sim 50\%$ higher than that of the surrounding membrane, the relatively low fibril coverage leads to bending behavior that is largely unchanged from that of a homogeneous lipid bilayer. Note that while Eq. 6.7 predicts that systems with a higher fibril coverage would potentially increase K_{eff} to the point of observing measurable differences, higher coverages were observed to promote aggregation of the fibrils, breaking the isotropy of the system and rendering Eq. 6.7 (and the entire homogeneous elastic theory) invalid.

6.6 Summary and Discussion

Membranes have essential roles *in vivo*, from holding cytoplasmic material in the cell interior to active roles in ion transport and cell signalling. Maintaining the integrity of the lipid bilayer is crucial for cell viability, however, membrane surfaces can act as catalysts for protein and peptide aggregation [260], a process that can potentially damage the membrane. Protein aggregates have been reported to affect cell membrane structure via peptide insertion and pore formation, or by mechanical deformation from fibril growth at the membrane surface. A wide range of proteins (including α-synuclein [261], the Alzheimer Aβ peptide [53], IAPP [52], and lysozyme [231]) bind to and fibrillize on several model lipid bilayer systems, including membranes composed of anionic phospholipids, mixed-membranes involving neutral and zwitterionic lipids, as well as on membranes involving lipid rafts of cholesterol and sphingomyelin [52, 53, 262]. The degree of fibrillization is specified by peptide sequence and bilayer composition [227].

In this chapter, we investigated the aggregation of peptides on the surface of a lipid bilayer using coarse-grained models. We analyzed the pathways and aggregate structures as a function of peptide backbone rigidity (a measure of β-sheet propensity), and as a function of interaction strength between the peptide and the lipid head groups. The latter parameter was modulated to mimic the variable membrane-peptide interaction strengths observed experimentally, a factor of the nature of the head groups and membrane composition [154, 155]. We focused here on peptide-membrane parameters that led to fibrillization on the surface, rather than insertion of the peptide into the lipid bilayer. This type of fibrillization has been observed for certain lipid compositions, e.g., for lysozyme which interacts primarily with the polar region of the membrane and does not

easily penetrate into the membrane's hydrophobic core [231, 263].

Our simulations showed that the peptides aggregated readily on the surface, and that the surface induced formation of β-sheet structure. For both flexible and rigid peptides, the membrane draws them to the surface, increasing their local concentration (spatial crowding or confinement), and favoring inter-peptide interactions. Once bound, the peptides diffuse on the surface to form larger aggregates. We observe oligomers diffusing on the surface and coming together, as well as (for high surface attraction) monomers diffusing and adding at the end of a growing fibril. The last scenario is reminiscent of recent experimental work on the Amyloid-β peptide on PEGs and on supported bilayers, showing through single molecule fluorescence the addition of monomeric peptides to fibril ends. These studies indicated fibril growth required mobile peptides, and that fibril formation was hampered on highly attractive surfaces that bound too strongly to the peptides and reduced their diffusivity [221, 224]. An important result from our simulations is that peptides that formed only amorphous aggregates in the bulk were able to form ordered β-sheet structure on the membrane surface. This highlights the importance of considering cellular factors when studying aggregation. Indeed, the flexible peptides in a dilute *in vitro* context would be labelled as non-amyloidogenic, but become amyloidogenic in an *in vivo* milieu with membranes present. Since aggregation morphology is linked to toxicity, this distinction becomes important, particularly in the design of structure-specific aggregation inhibitors.

We contrasted the aggregation pathways to those observed in binding to a solid, rather than fluid, surface. Our findings show several key similarities and differences between binding to a membrane and a solid surface, as summarized below.

Similarities were found in the pathway trends for aggregation. As in the solid surface case, increasing the peptide-surface attraction strongly favors the individual direct-deposition of peptides onto the surface, giving rise to single-layered fibrillar aggregates. In the case of high surface attraction, the flexible, bent-shaped monomers individually remodeled on the surface to adopt β-strand (aggregate-prone N*) conformations, while in the case of mid-surface attraction, the amorphous oligomers bind to the surface and use it as a template to rearrange into β-sheet structures.

However, we observe several key differences on the membrane. Our simulations show that membrane oscillations have several unique effects on bound aggregates, such as reversibility of kinetics, whereas on a solid surface the dynamics of structure transitions exhibited far less mobility. While undulations of a fluid membrane kick bound fibrils up to form β-barrels, a solid surface favors structures aligned in its plane, maintaining a much stronger correlation between layers, up to quadruple-layered fibrils, which are never seen on our membrane model.

A significant difference between a membrane and a crystal surface is that the latter is anisotropic, having preferred directions related to its crystallographic symmetry. The orientation of bound fibrils aligns to these directions. This results in all the peptides in the system assembling into a single long fibril. A membrane surface is isotropic in thermal average. Thus peptides forming on the membrane have no preferred direction, and therefore, on the time scales we have simulated, we see several fibrils in random orientations jammed together rather than a single fibril with one orientation. On a solid surface, the direct-deposition mechanism was associated with the cooperativity of peptides binding to the surface, aggregating, and aligning into a fibril. The time scales of these three mechanisms converged for the direct-deposition pathway. On our fluid membrane this cooperativity is

not observed, instead, aggregation and alignment mechanisms are bottlenecked by slower spatial and angular diffusion of the membrane-bound peptides.

Finally, we find that while the fluid membrane affects the formation of aggregate structures, the resulting rigid fibril structure in turn influences membrane structure and properties. In fibril-associated regions of the membrane, the bending modulus is locally increased by about fifty percent compared to unassociated regions. Thus a fibril-coated membrane will have a slightly higher resistance to a nonzero curvature. Peristaltic modes (fluctuations in membrane thickness) are markedly damped by fibrils, a damping that increases as larger fibrils are placed on the membrane. We find that lipid tilt fluctuations are also damped by the presence of fibrils, as lipids adopt a preferred non-zero tilt in the vicinity of fibrils. However, the effect of this local tilt ordering over long wavelengths is to enhance tilt fluctuations as the fibrils and associated tilted lipids undergo translational and rotational diffusion. Lipids under the fibrils close-pack into a hexagonal lattice to maximize the number of attractive interactions between lipid head groups and peptide hydrophilic residues. Overall, the fluid membrane results in slightly less ordered peptide aggregate structures and an enhanced mobility of structure transitions in comparison with aggregation on a crystal surface. In contrast, ordered fibrils that form on the membrane yield a modest increase to the bilayer's structural order and generally damp its dynamics on a local length scale.

Chapter 7

Conclusions

For this work, we have analyzed how the presence of various surfaces modulates peptide aggregation using a coarse-grained phenomenological model. We contrast aggregation pathways and morphologies on different template surfaces to behavior in bulk solution [7, 57, 58]. Our coarse-grained peptide model uses three beads per residue, one for the side chain and two for the backbone. In the bulk it exhibits two principal fibril growth mechanisms: a direct templating of peptides onto the growing fibril and a condensation-ordering mechanism where fibrils spontaneously order from disordered oligomers (Fig. 1.5 top panel). Peptides bury their hydrophobic residues by forming multi-layered fibrils in a characteristic interdigitated steric zipper pattern (Figs. 1.4 and 1.6).

Aggregation in vivo occurs in the complex cellular environment, known as the cellular milieu. However, most computational studies of the process are conducted in bulk solution to reduce complexity. In this work, we have endeavored to understand the effect of various templates, both biomolecular and solid materials, on peptide aggregation. The interplay between membranes and aggregates is crucially relevant in light of its association with amyloid diseases such as Alzheimer's

and Parkinson's disease. The potential cytotoxicity of membrane-bound fibrils is not fully understood, although the damage an unstructured oligomer can do to a membrane is better known [35, 38–40]. For fluid templates, we have studied the effect of bound aggregates on the structure and mechanical properties of the surface.

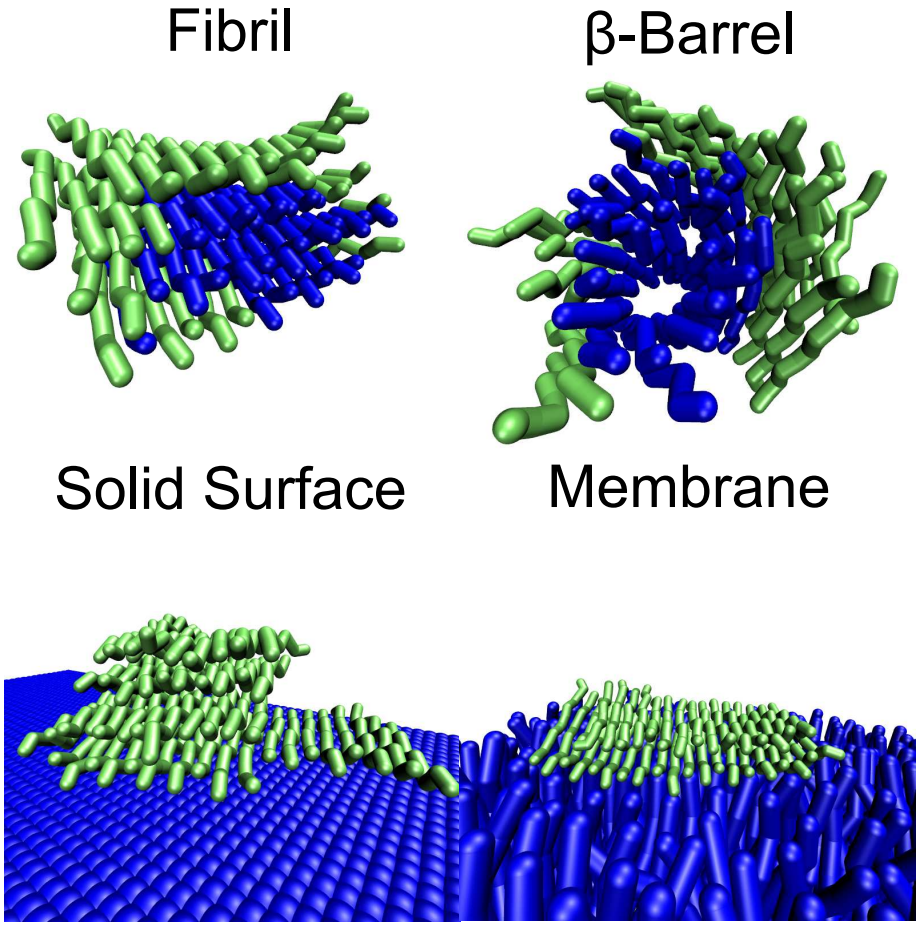

Figure 7.1: Shows how various surfaces act as a template for fibril formation. Surfaces, shown in dark blue, include a three-layered fibril, a β-barrel aggregate, a crystalline surface, and a lipid bilayer.

Our results show that surfaces with a high degree of structural order and rigidity drive formation of ordered fibrillar aggregate morphologies by acting as templates on which the fibrils can adsorb. Images of such surface templating are

shown in Fig. 7.1. The effectiveness of a surface as a template depends on several factors. A solid surface is an excellent template due to its flatness and rigidity. The fluidity of templates such as a membrane or fibrillar seed inhibits the kinetics of fibrillization when compared to a solid surface. In particular, the undulations of a fluid membrane were found to prevent the formation of four-layered fibrils, instead generating non-horizontal β-sheet structures, such as β-barrels (Fig. 6.5 (a) and (d)).

Additionally, the in-plane fluidity of the membrane leaves no preferred directions for fibril orientation. In contrast, a solid surface grows fibrils along its lines of crystallographic symmetry [181]. This reduces the time scale for fibril rotational diffusion and results in the convergence of the time scales for peptide-surface binding, peptide alignment, and fibril growth in the limit of a highly attractive surface. This cooperativity of the binding and aggregation kinetics is a key feature of solid surfaces, and is not observed in fluid membranes where the diffusion time of fibrils on the surface bottlenecks fibril growth. This results in the frequent lack of fibril alignment, as seen in Fig. 6.5 (c).

However, it should be noted that compared to aggregation in the bulk, all surfaces we simulated enhanced the formation of ordered fibrils, with the solid surface giving the strongest bias. The exception to this is the amorphous seed aggregate from Chapter 5, although this is not truly a surface, since the peptides absorbed into, rather than adsorbed on, the amorphous seed.

For fluid surfaces, peptide adsorption alters the kinetics of the template as well. This is seen most dramatically when amorphous-prone aggregates bind to a fibrillar seed (Fig. 5.7). A bound amorphous aggregate pulls seed peptides away from the fibril and into itself. However, once the concentration of fibril-prone seed peptides is sufficiently high in the amorphous aggregate, the ordered β-sheet

structure reasserts itself, suggesting that cytotoxic amorphous-prone aggregates can be sequestered into an ordered fibril if they come in contact with an aggregate-compatible fibril.

Further effects of aggregates on the template surface are demonstrated in Chapter 6.5. Fibrils, to a modest extent, damp membrane undulations underneath the fibrils, locally increasing the membrane's bending modulus. Fluctuations in lipid tilt are also locally damped as the tilt vectors slightly align in the direction of the peptides. The most significant effect on the membrane is the in-plane ordering of lipids. Lipids underneath fibrils locally adopt a hexagonal close-packing to maximize the attractive interactions between the lipid head groups and the peptides. This phenomenon is complementary to what is observed on a solid surface, where the surface reorients fibrils for optimal packing between surface beads and peptide side chains.

We find in general that when an aggregate adsorbs onto a surface, there is a transfer of order from the more ordered object to the less ordered one. For example, a highly ordered surface induces the aggregates to become more ordered, and a fluid surface becomes more ordered when in contact with an ordered fibril. Regardless, a template with a high enough surface tension to maintain a two dimensional binding interface increases the effective β-sheet propensity of adsorbed aggregates. However, the effects we observe of bound fibrils on a membrane are generally local to the fibril's position, suggesting that the presence of fibrils on a membrane surface in equilibrium would not cause a global disruption of the bilayer.

Appendix A

Hydrophobic Collapse of a Homopolymer

In this section, we discuss related work we have done in collaboration with Valeria Molinero and Bin Song at the University of Utah. It addresses one necessary shortcoming of our work in other chapters, namely, our use of an implicit solvent model with Langevin dynamics. As mentioned in Chapter 2.3, the process of fibrillization occurs in a system where peptides are separated by considerable volume; in other words, the system consists mostly of solvent. Since the computational cost of filling the volume with explicit water molecules is prohibitive, we turned to Langevin implicit solvent, which scales linearly with the number of peptide atoms instead of quadratically with the solvent volume.

A question that arises from this, however, is how well does implicit solvent capture the hydrophobic effect? To answer this, we conducted a study contrasting our implicit water model with an explicit coarse-grained water model and another popular implicit water force field known as a desolvation potential [264]. The system under consideration is the hydrophobic collapse of a poly-alkane chain.

A.1 Methods

A.1.1 Polymer Model

We study two types of poly-alkane chains. The first is representative of methane (denoted throughout as M). We employ a Lennard-Jones potential between methane beads, with $\epsilon = 0.34$ kcal/mol and $\sigma = 4.08$Å. The second is a generic model of a less hydrophobic polymer, referred to as the "neutral" polymer (denoted N). Its Lennard-Jones potential has $\epsilon = 0.091$ kcal/mol and $\sigma = 3.95$Å. The pair potentials between alkane beads are depicted by the solid red curves of Fig. A.1.

The interaction between alkane beads and water molecules is likewise represented by a Lennard-Jones potential. For the methane model, $\epsilon = 0.24$ kcal/mol and $\sigma = 4.05$Å; for the neutral model, $\epsilon = 0.10$ kcal/mol and $\sigma = 3.17$Å.

Bond potentials are harmonic ($V = \frac{1}{2}k_b(r - r_0)^2$). For methane polymers, the spring constant is $k_b = 20$ kcal/mol Å^{-2} and the equilibrium bond distance is $r_0 = 2$Å. For N polymers, $k_b = 60$ kcal/mol Å^{-2} and $r_0 = 1.54$Å.

The angles are constrained by a harmonic angle potential ($V = \frac{1}{2}k_\theta(\theta - \theta_0)^2$). In the methane model, $k_\theta = 20$ kcal/mol rad^{-2} and $\theta_0 = 109°$. In the neutral model, $k_\theta = 124.2$ kcal/mol rad^{-2} and $\theta_0 = 114°$.

For the neutral (N) polymers, we set out to mimic the TraPPE potential [265] of poly-hydrocarbon chains. Thus we impose angle and dihedral potentials for N polymers, with the 1–4 pair interaction turned off. The methane (M) system has a higher hydrophobicity than the N polymers. We did not include a dihedral potential for methane polymers, and 1–4 pair interactions are enabled. The dihedral potential for N polymers is: $V = \frac{1}{2}K_1\cos(\phi) + \frac{1}{2}K_2\cos(2\phi) + \frac{1}{2}K_3\cos(3\phi)$, where $K_1 = 1.41$ kcal/mol, $K_2 = 0.27$ kcal/mol, and $K_3 = 3.14$ kcal/mol.

A.1.2 Explicit CG Water Model

The explicit water model we use is known as the mW model, developed by Molinero and Moore [266]. It is a single bead model with no hydrogens or electrostatic interactions, but is capable of capturing the tetrahedral arrangement of water molecules through short-range anisotropic potentials with two- and three-body terms. This water model has been shown to reproduce experimental data pertaining to a number of water-mediated processes, including methane hydration (unpublished result) and methane-pair association [267]. The mW model's ability to capture the essential elements of the hydrophobic effect is due in large part to its accurate representation of water structure (namely density, radial, and angular distribution functions). For a more detailed description of the interaction, see reference [266].

A.1.3 Implicit Desolvation Potential

We use Langevin dynamics to capture the thermal motions and viscosity from the solvent. We compute the pair potential between two CG alkane particles by simulating the pair in explicit mW water. The implicit water potential is computed from the explicit water free energy of separation of the two particles (subtracting off the entropy proportional to the separation to avoid double counting). This implicitly accounts for the energetic and entropic contributions of solution to the separation between a pair of alkanes. A qualitative feature of this potential is the solvent separation minima. Two particles experience a global minimum at close separation, a second minimum when they are separated by a distance of one water molecule (the first solvent separated pair), and so forth. See the green curve of Fig. A.1. The pair interaction is computed as a tabulated potential rather than a

functional form

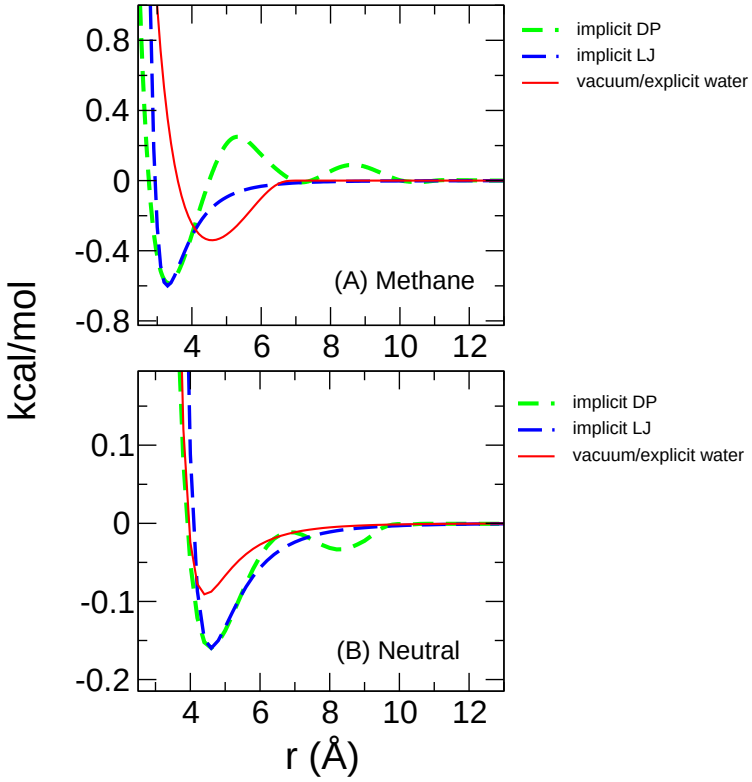

Figure A.1: Shows the pair potentials for (A) methane polymers and (B) neutral polymers. Implicit DP is the implicit water desolvation potential obtained by the free energy of separation computed for the system in explicit water (using the vacuum/explicit water potential), and Implicit LJ is the implicit water potential corresponding to the primary well of the desolvation potential.

A.1.4 Implicit Lennard-Jones Potential

Finally, we ignore the solvent separated minima of the desolvation potential and fit the primary well to a Lennard-Jones interaction. For the methane model, we found $\epsilon = 0.60$ kcal/mol and $\sigma = 4.08$Å; for the neutral model, $\epsilon = 0.16$ kcal/mol and $\sigma = 2.93\mathring{A}$. These interactions are shown as blue curves in Fig. A.1.

A.1.5 Simulations

For the methane system, we ran simulations for polymer lengths of 10, 20, 30, 40, 50, and 60 beads using four different models: explicit mW water, a desolvation potential, a Lennard-Jones approximation to the primary well, and vacuum simulations (explicit water modulo water). We also conducted simulations of poly-N chains of 20, 30, and 60 beads with the same solvent models.

The temperature for all systems was set at $300K$, using a Nose-Hoover thermostat for the explicit water system, and Langevin dynamics for the implicit water systems and vacuum simulations. We used a time step of 10fs.

We employed umbrella sampling with respect to the radius of gyration to efficiently sample high free energy barriers. We conducted approximately 5 umbrella samples per system in addition to an unbiased run. Each simulation was 400ns. The spring constant on the umbrella samples was 1 kcal/mol.

Note that we conducted umbrella sampling for all systems except for chain lengths 20, 40, and 50 of the explicit water model for the methane system. These exceptions were a single unbiased 400ns run, used only for the computation of $\langle R_g \rangle$ and not for computation of the free energy, which would require more sampling.

A.2 Results

In this section we compare the free energy of alkane chains in mW water, vacuum, and implicit water.

A.2.1 Neutral Polymers

Fig. A.2 shows the free energy of collapse of the N system in explicit water, with the desolvation potential, with a Lennard-Jones potential, and in vacuum. The three polymers are 20, 30, and 60 peptides long. The most striking feature is the similarity between explicit water and vacuum simulations, in contrast to the deviations between implicit and explicit water results. Fig. A.2 also shows that as the length of the polymer increases, N polymers both in vacuum and explicit water become increasingly stable in the collapsed state. Solvation of 30N and 60N slightly stabilizes the extended state compared to vacuum simulations, which capture the relative stability of the two states of 20N. In a study of TraPPE alkane chains, Ferguson et al. found that solvent did not affect the free energy profiles of chains shorter than 20 units [268]. The authors projected that free energy of longer chains in vacuum and in water would diverge, as demonstrated in Fig. A.2.

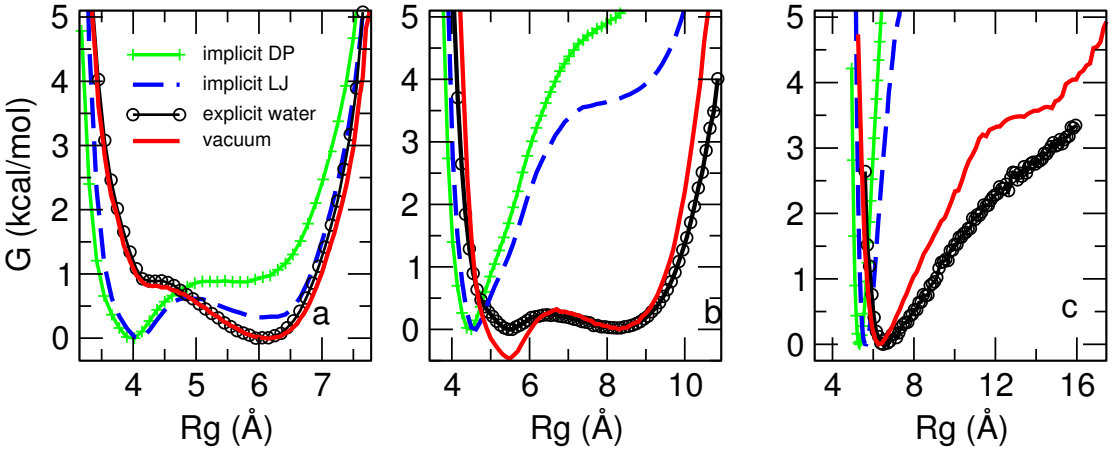

Figure A.2: Free energy of collapse of collapse of N-polymer system under the four different solvent models. Chain lengths of (a) 20, (b) 30, and (c) 60. Lower radius of gyration (R_g) represents a higher degree of polymer collapse.

The desolvation and Lennard-Jones potentials failed to reproduce the explicit water free energy profiles for N polymers in water. As these implicit water

potentials are more hydrophobic than the vacuum model, we expect a shift favoring the collapsed state. For the 20N polymer, both implicit solvent models favor a collapsed state, while the explicit water model favors an uncollapsed state. Still, the two states exist at roughly the same radii of gyration in all models. For 30N, both implicit water models perform miserably at reproducing a balance between collapsed and uncollapsed states, the implicit models being much too collapsed. It is interesting that for all chain lengths, the Lennard-Jones potential does slightly better at reproducing the correct uncollapsed state. Both implicit models correctly exhibit the tendency to collapse as chain length increases, however, they greatly overestimate this effect. It is known that longer chain length favors the collapsed state. As is shown in Fig. A.2 (c), 60N is predominantly collapsed. However, implicit water models exclude extended states, which are present (though rare) in explicit water simulations.

We find that neither the desolvation potential nor its derived LJ potential reproduces a correct distribution of the chain's radius of gyration, even qualitatively.

A.2.2 Methane Polymers

From the previous section, both implicit solvent models are a poor match to our alkane chain in explicit water, while the vacuum potential performs remarkably. This section discusses how these implicit water models fare for a peptide with stronger hydrophobic interactions (poly-M), in which water is expected to play a more significant role.

Fig. A.3 depicts the potential of mean force with respect to radius of gyration for 10-, 20-, 30-, and 60mers of poly-M for each solvation method. In explicit

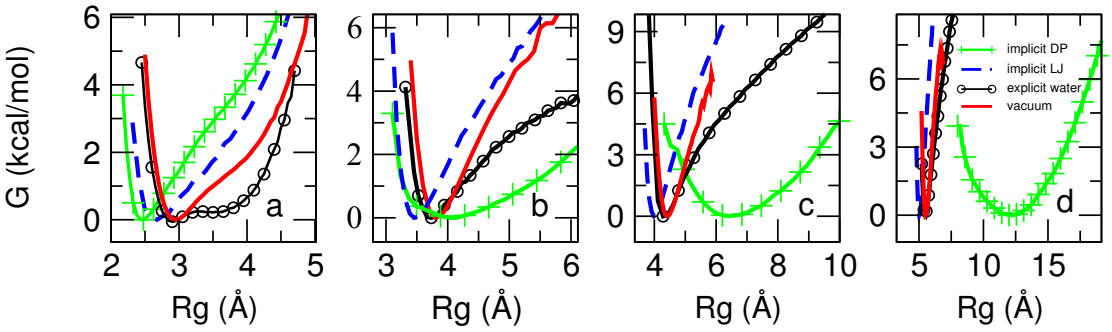

Figure A.3: Free energy of collapse of collapse of N-polymer system under the four different solvent models. Chain lengths of (a) 10, (b) 20, (c) 30, and (d) 60. A smaller radius of gyration (R_g) represents a higher degree of polymer collapse.

solvent, the M-polymer favors a compact state for large chains (a single well is seen for the 20mer, 30mer, and 60mer in Figs. A.3 (b), (c), and (d), black curve), but populates both extended and compact conformations for short chains (as seen by the double well for the 10mer, with the compact state marginally favored by 0.28 kcal/mol, Fig. A.3 (a)). Approximating the explicit solvent by a desolvation potential has a substantial effect on the state of collapse of hydrophobic polymers. The desolvation potential incorrectly predicts that longer polymers exist solely in extended states, without even a metastable compact state (Fig. A.3, green curve). The 10mer, on the other hand, favors extremely compact states, with a single stable state at a radius of gyration more compact than seen for the polymer in mW water.

Interestingly, further coarsening of the desolvation potential into the single-well Lennard-Jones potential restores the qualitative behavior of collapse found in the explicit water model, particularly for the longer chains. For all three polymer lengths, a Lennard-Jones interaction gives a much closer match to explicit water than the desolvation potential does. More strikingly, even with these more hydrophobic polymers, the vacuum model outperforms the implicit water model

at capturing R_g of the collapsed state, though the vacuum model does little to stabilize more extended states. The main difference between LJ and vacuum is the R_g of the collapsed state. However, by horizontally shifting the LJ free energy profile to that of vacuum results the two models overlap.

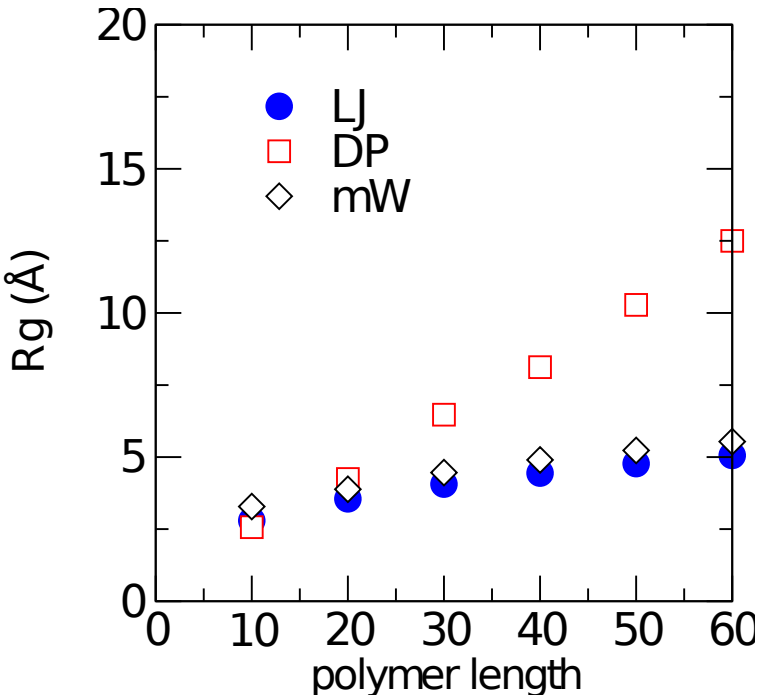

Figure A.4: Dependence of average radius of gyration (for poly-M) with polymer length for all three pair interaction models.

The behavior of the polymer in different solvent models is further highlighted in Fig. A.4, where we show the dependence of the average radius of gyration with chain length. The desolvation potential scales roughly as $R_g \propto N^{0.9}$, which is very nearly the behavior of a perfectly rigid chain ($R_g \propto N$). The explicit water and Lennard-Jones models both exhibit a dependence of roughly $R_g \propto N^{1/3}$, the expected behavior of a polymer in poor solvent.

One might predict that the desolvation potential would fare better than the simple Lennard-Jones potential, as the former captures more of the physical

features seen in the M-M association PMF in explicit water (Fig. A.1). However, as seen in both the PMF and R_g plots, the desolvation potential does poorly for long chain lengths, producing expanded conformations rather than the compact conformations seen in explicit solvent. In the case of the short polymer, the desolvation potential showed greater collapse than the explicit water model. It is also the only system for which the Lennard-Jones model better matched the desolvation potential than it matched the explicit water model.

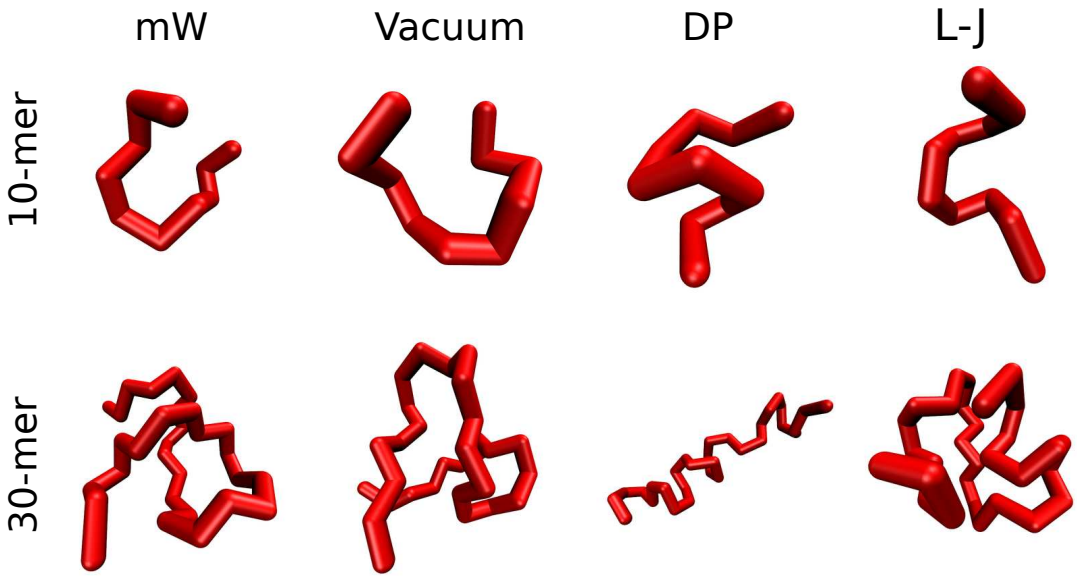

Figure A.5: Typical renders of our methane polymer system, contrasting the polymer states for the three different interactions: coarse-grained explicit water (mW), the polymer in vacuum, a desolvation potential in implicit water (DP), and a Lennard-Jones interaction in implicit water (L-J). The top row is a 10mer, and the bottom row is a 30mer.

This is understood by studying the polymer conformations for the desolvation potential, shown in Fig. A.5. On short length scales, the polymer forms coils, sampling the desolvation potential's primary well. At longer length scales, the entire chain cannot collapse without having pairs in the high energy region

of the desolvation barrier. We see highly positive potential energies for 30mers in the collapsed state, making the collapsed state effectively forbidden under the desolvation potential. Thus the polymer becomes locally collapsed, but globally extended. The Lennard-Jones potential lacks the desolvation barrier, and therefore longer polymers collapse completely. The desolvation barrier exists because a lone pair of hydrophobes can separate to allow a water molecule between them, and this is energetically favorable. However, inside the hydrophobic core of a polymer, there is no water available, making a desolvation barrier unphysical in this region. Our polymers in explicit water are completely collapsed, such that water molecules do not insert between parts of the chain. The desolvation potential, designed to model the thermodynamics of a *pair* of molecules in implicit water, fails when employed to model the thermodynamics of a chain.

The interaction between beads in the explicit solvent model is Lennard-Jones, though the interaction strength is lower than our implicit solvent models by about 60%. The vacuum simulations, therefore, can be thought of as Lennard-Jones interactions in implicit water. Thus, in both the methane and N chain, we found Lennard-Jones models which exhibited similar behavior to the explicit water models they were derived from. We conjecture that, for a given polymer system, one could find some implicit solvent Lennard-Jones model that adequately reproduces the free energy of polymer collapse in explicit water. However, we find no means to select the correct Lennard-Jones parameters without simulating the entire peptide chain in explicit water. We have shown here that deriving implicit water potentials from the free energy of a reduced system (pair of beads) in water will fail for a polymer made of these beads. We also caution that once an optimal set of Lennard-Jones parameters is found, it would be system and temperature specific.

A.3 Summary and Discussion

We have employed coarse-grained molecular dynamics simulations to study the collapse of two homopolymers: poly-methane (poly-M) and a more weakly attractive "neutral" polymer (poly-N). We contrasted their behavior in explicit water to various implicit solvent representations. For explicit water simulations, we used the coarse-grained (1-bead) mW water model, which reproduces the structure of water using a 3-body interaction. Our implicit water simulations used a desolvation potential (DP), a Lennard-Jones potential (LJ) capturing the primary well of DP, and vacuum which is simply the explicit solvent model without water.

The primary result of our work is that the desolvation potential, parameterized to the free energy of separation of two alkanes in explicit water, completely fails to reproduce the correct behavior of polymer collapse, either qualitatively or quantitatively. The desolvation potential has several local minima corresponding an alkane pair separated by n water molecules. This becomes unphysical for $n > 0$ in a collapsed polymer containing no internal water molecules, artificially forcing the polymer into an extended state. This issue is especially pronounced in poly-M, where we have computed the local maximum in the free energy of separation between $n = 0$ and $n = 1$ to be greater than that of infinitely separated methanes. While accurate for a pair of methanes, it fails for a polymer, since in a collapsed polymer, enough pairs of methanes are at a distance corresponding to this free energy maximum as to prohibit the collapsed state in the DP model, despite its prevalence in explicit water.

The Lennard-Jones implicit solvent, which fits to the first minimum of the desolvation potential, captures polymer collapse significantly better. Qualitatively, the states of the polymer under the LJ implicit solvent look very similar

to those of mW explicit water, whereas the polymers under the DP potential are much too extended. Using LJ, the free energy profiles of the radius of gyration are relatively similar to explicit water simulations, although LJ does notably overestimate the degree of polymer collapse. Computing the mean radius of gyration as a function of chain length reveals that both the LJ system and the explicit water system behave as a collapsed chain in poor solvent ($R_g \propto N^{1/3}$), while the DP system acts like an extended rod ($R_g \propto N^{0.9}$). What is most striking is how accurately the free energy profiles of polymer collapse are reproduced by simply removing the water without altering the intra-polymer potentials (vacuum). The radius of gyration of the collapsed state is reproduced almost perfectly, though like the LJ potential, it overestimates the degree of polymer collapse.

Since both the LJ interactions and the vacuum simulations use a single-well Lennard-Jones interaction between the peptides, we conclude that to mimic polymer collapse using implicit solvent, it may be better to keep a Lennard-Jones interaction between the polymer beads (as we did in Chapters 3–6) than to attempt to capture the solvent effect using a multi-well desolvation potential derived from the free energy of separation of a pair of the polymer beads, which introduces spurious unfavorable water interactions when the polymer beads are closely packed.

Bibliography

[1] Bernard R Brooks, Robert E Bruccoleri, Barry D Olafson, David J States, S Swaminathan, and Martin Karplus. Charmm: A program for macromolecular energy, minimization, and dynamics calculations. *Journal of computational chemistry*, 4(2):187–217, 1983.

[2] Wendy D Cornell, Piotr Cieplak, Christopher I Bayly, Ian R Gould, Kenneth M Merz, David M Ferguson, David C Spellmeyer, Thomas Fox, James W Caldwell, and Peter A Kollman. A second generation force field for the simulation of proteins, nucleic acids, and organic molecules. *J. Am. Chem. Soc.*, 117(19):5179–5197, 1995.

[3] William L Jorgensen and Julian Tirado-Rives. The opls [optimized potentials for liquid simulations] potential functions for proteins, energy minimizations for crystals of cyclic peptides and crambin. *J. Am. Chem. Soc.*, 110(6):1657–1666, 1988.

[4] Alex Morriss-Andrews, Joerg Rottler, and Steven S Plotkin. A systematically coarse-grained model for dna and its predictions for persistence length, stacking, twist, and chirality. *J. Chem. Phys.*, 132(3):035105, 2010.

[5] R. Vácha and D. Frenkel. Relation between molecular shape and the mor-

phology of self-assembling aggregates: A simulation study. *Biophys. J.*, 101(6):1432–1439, 2011.

[6] D. Thirumalai, D.K. Klimov, and R.I. Dima. Emerging ideas on the molecular basis of protein and peptide aggregation. *Curr. Opin. Struc. Biol.*, 13(2):146 – 159, 2003.

[7] G. Bellesia and J.-E. Shea. Self-assembly of β-sheet forming peptides into chiral fibrillar aggregates. *J. Chem. Phys.*, 126(24):245104, 2007.

[8] Yanting Wang and Gregory A Voth. Molecular dynamics simulations of polyglutamine aggregation using solvent-free multiscale coarse-grained models. *J. Phys. Chem. B*, 114(26):8735–8743, 2010.

[9] Siewert J Marrink and D Peter Tieleman. Perspective on the martini model. *Chem. Soc. Rev.*, 42(16):6801–6822, 2013.

[10] Claudio Soto. Unfolding the role of protein misfolding in neurodegenerative diseases. *Nat. Rev. Neurosci.*, 4(1):49–60, 2003.

[11] M. Stefani. Protein folding and misfolding on surfaces. *International Journal of Molecular Sciences*, 9(12):2515, 2008.

[12] F. Chiti and C.M. Dobson. Protein misfolding, functional amyloid, and human disease. *Annu. Rev. Biochem.*, 75:333, 2006.

[13] Jeffrey R Brender, Samer Salamekh, and Ayyalusamy Ramamoorthy. Membrane disruption and early events in the aggregation of the diabetes related peptide iapp from a molecular perspective. *Accounts Chem. Res.*, 45(3):454–462, 2011.

[14] Joseph T Jarrett and Peter T Lansbury Jr. Amyloid fibril formation requires a chemically discriminating nucleation event: studies of an amyloidogenic sequence from the bacterial protein osmb. *Biochemistry*, 31(49):12345–12352, 1992.

[15] S.B. Padrick and A.D. Miranker. Islet amyloid: Phase partitioning and secondary nucleation are central to the mechanism of fibrillogenesis. *Biochemistry*, 41(14):4694–4703, 2002.

[16] N. Carulla, M. Zhou, M. Arimon, M. Gairí, E. Giralt, C.V. Robinson, and C.M. Dobson. Experimental characterization of disordered and ordered aggregates populated during the process of amyloid fibril formation. *Proc. Natl. Acad. Sci.*, 106(19):7828, 2009.

[17] A.K. Paravastu, R.D. Leapman, W.M. Yau, and R. Tycko. Molecular structural basis for polymorphism in alzheimer's β-amyloid fibrils. *Proc. Natl. Acad. Sci.*, 105(47):18349, 2008.

[18] G. Reddy, J.E. Straub, and D. Thirumalai. Dynamics of locking of peptides onto growing amyloid fibrils. *Proc. Natl. Acad. Sci.*, 106(29):11948–11953, 2009.

[19] J. Zheng, H. Jang, and R. Nussinov. β2-microglobulin amyloid fragment organization and morphology and its comparison to Aβ suggests that amyloid aggregation pathways are sequence specific. *Biochemistry*, 47(8):2497–2509, 2008.

[20] B. O'Nuallain, A.D. Williams, P. Westermark, and R. Wetzel. Seeding specificity in amyloid growth induced by heterologous fibrils. *J. Biol. Chem.*, 279(17):17490–17499, 2004.

[21] M.R.H. Krebs, L.A. Morozova-Roche, K. Daniel, C.V. Robinson, and C.M. Dobson. Observation of sequence specificity in the seeding of protein amyloid fibrils. *Protein Sci.*, 13(7):1933–1938, 2004.

[22] W. Xu, J. Ping, W. Li, and Y. Mu. Assembly dynamics of two-β sheets revealed by molecular dynamics simulations. *J. Chem. Phys.*, 130:164709, 2009.

[23] C. Wu, M.T. Bowers, and J.-E. Shea. Molecular structures of quiescently grown and brain-derived polymorphic fibrils of the alzheimer amyloid Aβ9-40 peptide: A comparison to agitated fibrils. *PLoS Computational Biology*, 6(3):e1000693, 2010.

[24] Y. Miller, B. Ma, and R. Nussinov. Polymorphism in alzheimer Aβ amyloid organization reflects conformational selection in a rugged energy landscape. *Chemical Reviews*, 2010.

[25] R. Pellarin, P. Schuetz, E. Guarnera, and A. Caflisch. Amyloid fibril polymorphism is under kinetic control. *J. Am. Chem. Soc.*, 2010.

[26] J. Meinhardt, C. Sachse, P. Hortschansky, N. Grigorieff, and M. Fändrich. A β(1-40) fibril polymorphism implies diverse interaction patterns in amyloid fibrils. *J. Mol. Biol.*, 386(3):869–877, 2009.

[27] M. Fändrich, J. Meinhardt, and N. Grigorieff. Structural polymorphism of alzheimer Aβ and other amyloid fibrils. *Prion*, 3(2):89, 2009.

[28] R. Kodali and R. Wetzel. Polymorphism in the intermediates and products of amyloid assembly. *Curr. Opin. Struc. Biol.*, 17(1):48–57, 2007.

[29] A.K. Paravastu, A.T. Petkova, and R. Tycko. Polymorphic fibril formation by residues 10-40 of the Alzheimer's β-amyloid peptide. *Biophys. J.*, 90(12):4618–4629, 2006.

[30] A.T. Petkova, R.D. Leapman, Z. Guo, W.M. Yau, M.P. Mattson, and R. Tycko. Self-propagating, molecular-level polymorphism in alzheimer's β-amyloid fibrils. *Science*, 307(5707):262, 2005.

[31] Claire Goldsbury, Peter Frey, Vesna Olivieri, Ueli Aebi, and Shirley A. Müller. Multiple assembly pathways underlie amyloid-β fibril polymorphisms. *J. Mol. Biol.*, 352(2):282 – 298, 2005.

[32] Y. Miller, B. Ma, and R. Nussinov. Polymorphism of Alzheimer's Aβ17-42 (p3) Oligomers: The Importance of the Turn Location and Its Conformation. *Biophys. J.*, 97(4):1168, 2009.

[33] R. Pellarin, P. Schuetz, E. Guarnera, and A. Caflisch. Amyloid Fibril Polymorphism Is under Kinetic Control. *J. Am. Chem. Soc.*, pages 583–596, 2010.

[34] C. Wu, M.T. Bowers, and J.-E. Shea. Molecular structures of quiescently grown and brain-derived polymorphic fibrils of the alzheimer amyloid Aβ9-40 peptide: A comparison to agitated fibrils. *PLoS Comput Biol*, 6(3):e1000693, 2010.

[35] M. Stefani. Structural features and cytotoxicity of amyloid oligomers: Implications in alzheimer's disease and other diseases with amyloid deposits. *Progress in Neurobiology*, 2012.

[36] G. Anderluh, I. Gutirrez-Aguirre, S. Rabzelj, S. Čeru, N. Kopitar-Jerala,

P. Maček, V. Turk, and E. Žerovnik. Interaction of human stefin b in the prefibrillar oligomeric form with membranes. *FEBS Journal*, 272(12):3042–3051, 2005.

[37] I. Sirangelo, C. Malmo, C. Iannuzzi, A. Mezzogiorno, M.R. Bianco, M. Papa, and G. Irace. Fibrillogenesis and cytotoxic activity of the amyloid-forming apomyoglobin mutant w7fw14f. *J. Biol. Chem.*, 279(13):13183, 2004.

[38] J.P. Cleary, D.M. Walsh, J.J. Hofmeister, G.M. Shankar, M.A. Kuskowski, D.J. Selkoe, and K.H. Ashe. Natural oligomers of the amyloid-β protein specifically disrupt cognitive function. *Nature neuroscience*, 8(1):79–84, 2004.

[39] D.M. Walsh, I. Klyubin, J.V. Fadeeva, W.K. Cullen, R. Anwyl, M.S. Wolfe, M.J. Rowan, and D.J. Selkoe. Naturally secreted oligomers of amyloid β protein potently inhibit hippocampal long-term potentiation in vivo. *Nature*, 416(6880):535–539, 2002.

[40] W.L. Klein, G.A. Krafft, and C.E. Finch. Targeting small a [beta] oligomers: the solution to an alzheimer's disease conundrum? *Trends in neurosciences*, 24(4):219–224, 2001.

[41] V. Vetri, C. Canale, A. Relini, F. Librizzi, V. Militello, A. Gliozzi, and M. Leone. Amyloid fibrils formation and amorphous aggregation in concanavalin a. *Biophysical chemistry*, 125(1):184–190, 2007.

[42] Michael R Sawaya, Shilpa Sambashivan, Rebecca Nelson, Magdalena I Ivanova, Stuart A Sievers, Marcin I Apostol, Michael J Thompson, Melinda Balbirnie, Jed JW Wiltzius, Heather T McFarlane, Anders O Madsen, Chris-

tian Riekel, and David Eisenberg. Atomic structures of amyloid cross-β spines reveal varied steric zippers. *Nature*, 447(7143):453–457, 2007.

[43] Margaret Sunde, Louise C Serpell, Mark Bartlam, Paul E Fraser, Mark B Pepys, and Colin CF Blake. Common core structure of amyloid fibrils by synchrotron x-ray diffraction. *J. Mol. Biol.*, 273(3):729–739, 1997.

[44] Nicholas F. Dupuis, Chun Wu, J.-E. Shea, and M.T. Bowers. Human islet amyloid polypeptide monomers form ordered β-hairpins: A possible direct amyloidogenic precursor. *J. Am. Chem. Soc.*, 191:18283–18292, 2009.

[45] Nicholas F Dupuis, Chun Wu, Joan-Emma Shea, and Michael T Bowers. The Amyloid Formation Mechanism in Human IAPP: Dimers Have β-Strand Monomer–Monomer Interfaces. *J. Am. Chem. Soc.*, 133(19):7240–7243, 2011.

[46] Jun Zhao, Xiang Yu, Guizhao Liang, and Jie Zheng. Structural polymorphism of human islet amyloid polypeptide (hIAPP) oligomers highlights the importance of interfacial residue interactions. *Biomacromolecules*, 12(1):210–220, 2010.

[47] Jun Zhao, Xiang Yu, Guizhao Liang, and Jie Zheng. Heterogeneous triangular structures of human islet amyloid polypeptide (amylin) with internal hydrophobic cavity and external wrapping morphology reveal the polymorphic nature of amyloid fibrils. *Biomacromolecules*, 12(5):1781–1794, 2011.

[48] Chun Wu and Joan-Emma Shea. Coarse-grained models for protein aggregation. *Curr. Opin. Struc. Biol.*, 21(2):209–220, 2011.

[49] R. Sabate and J. Estelrich. Evidence of the existence of micelles in the

fibrillogenesis of β-amyloid peptide. *J. Phys. Chem. B*, 109:11027–11032, 2005.

[50] P. Seubert, C. Vigo-Pelfrey, F. Esch, M. Lee, H. Dovey, D. Davis, S. Sinha, M. Schlossmaker, and J. Whaley. Isolation and quantification of soluble alzheimer's -peptide from biological fluids. *Nature*, 359:325–327, 1992.

[51] C. Aisenbrey, T. Borowik, R. Byström, M. Bokvist, F. Lindström, H. Misiak, M.A. Sani, and G. Gröbner. How is protein aggregation in amyloidogenic diseases modulated by biological membranes? *Eur. Biophys. J.*, 37(3):247–255, 2008.

[52] Jefferson D. Knight and Andrew D. Miranker. Phospholipid catalysis of diabetic amyloid assembly. *J. Mol. Biol.*, 341(5):1175 – 1187, 2004.

[53] Lin-P'ing Choo-Smith, William Garzon-Rodriguez, Charles G. Glabe, and Witold K. Surewicz. Acceleration of amyloid fibril formation by specific binding of a-(1–40) peptide to ganglioside-containing membrane vesicles. *J. Biol. Chem.*, 272(37):22987–22990, 1997.

[54] Galyna P Gorbenko and Paavo KJ Kinnunen. The role of lipid–protein interactions in amyloid-type protein fibril formation. *Chem. Phys. Lipids*, 141(1–2):72 – 82, 2006.

[55] Herschel M Watkins, Alexis Vallee-Belisle, Francesco Ricci, Dmitrii E Makarov, and Kevin W Plaxco. Entropic and electrostatic effects on the folding free energy of a surface-attached biomolecule: an experimental and theoretical study. *J. Am. Chem. Soc.*, 134(4):2120–2126, 2012.

[56] Jie Zheng, Buyong Ma, and Ruth Nussinov. Consensus features in amyloid

fibrils: sheet–sheet recognition via a (polar or nonpolar) zipper structure. *Phys. Biol.*, 3(3):P1, 2006.

[57] G. Bellesia and J.-E. Shea. Effect of β-sheet propensity on peptide aggregation. *J. Chem. Phys.*, 130(14):145103, 2009.

[58] G. Bellesia and J.-E. Shea. Diversity of kinetic pathways in amyloid fibril formation. *J. Chem. Phys.*, 131:111102, 2009.

[59] J.E. Straub and D. Thirumalai. Toward a molecular theory of early and late events in monomer to amyloid fibril formation. *Annu. Rev. Phys. Chem.*, 62:437–463, 2011.

[60] Phuong Nguyen and Philippe Derreumaux. Understanding amyloid fibril nucleation and aβ oligomer/drug interactions from computer simulations. *Accounts Chem. Res.*, 47(2):603–611, 2013.

[61] Y. Sugita and Y. Okamoto. Replica-exchange molecular dynamics method for protein folding. *Chemical Physics Letters*, 314(1-2):141–151, 1999.

[62] Alessandro Barducci, Massimiliano Bonomi, and Michele Parrinello. Metadynamics. *Wiley Interdisciplinary Reviews: Computational Molecular Science*, 1(5):826–843, 2011.

[63] Franklin H Epstein, Jo WM Höppener, Bo Ahrén, and Cornelis JM Lips. Islet amyloid and type 2 diabetes mellitus. *New England Journal of Medicine*, 343(6):411–419, 2000.

[64] Ping Cao, Andisheh Abedini, and Daniel P Raleigh. Aggregation of islet amyloid polypeptide: from physical chemistry to cell biology. *Curr. Opin. Struc. Biol.*, 23(1):82–89, 2013.

[65] Jessica A Williamson and Andrew D Miranker. Direct detection of transient α-helical states in islet amyloid polypeptide. *Protein Sci.*, 16(1):110–117, 2007.

[66] Isaac T Yonemoto, Gerard JA Kroon, H Jane Dyson, William E Balch, and Jeffery W Kelly. Amylin proprotein processing generates progressively more amyloidogenic peptides that initially sample the helical state. *Biochemistry*, 47(37):9900–9910, 2008.

[67] Maximilian N Andrews and Roland Winter. Comparing the structural properties of human and rat islet amyloid polypeptide by md computer simulations. *Biophysical chemistry*, 156(1):43–50, 2011.

[68] Cayla Miller, Gul H Zerze, and Jeetain Mittal. Molecular simulations indicate marked differences in the structure of amylin mutants, correlated with known aggregation propensity. *J. Phys. Chem. B*, 117(50):16066–16075, 2013.

[69] A. Abedini and D.P. Raleigh. A role for helical intermediates in amyloid formation by natively unfolded polypeptides? *Phys. Biol.*, 6:015005, 2009.

[70] Lauren E Buchanan, Emily B Dunkelberger, Huong Q Tran, Pin-Nan Cheng, Chi-Cheng Chiu, Ping Cao, Daniel P Raleigh, Juan J de Pablo, James S Nowick, and Martin T Zanni. Mechanism of iapp amyloid fibril formation involves an intermediate with a transient β-sheet. *Proc. Natl. Acad. Sci.*, 110(48):19285–19290, 2013.

[71] Erika Andreetto, Li-Mei Yan, Andrea Caporale, and Aphrodite Kapurniotu. Dissecting the role of single regions of an iapp mimic and iapp in inhibition of

aβ40 amyloid formation and cytotoxicity. *Chembiochem*, 12(9):1313–1322, 2011.

[72] Sorin Luca, Wai-Ming Yau, Richard Leapman, and Robert Tycko. Peptide conformation and supramolecular organization in amylin fibrils: constraints from solid-state nmr. *Biochemistry*, 46(47):13505–13522, 2007.

[73] Buyong Ma and Ruth Nussinov. Stabilities and conformations of alzheimer's β-amyloid peptide oligomers (aβ16–22, aβ16–35, and aβ10–35): sequence effects. *Proc. Natl. Acad. Sci.*, 99(22):14126–14131, 2002.

[74] Robert Tycko. Molecular structure of amyloid fibrils: insights from solid-state nmr. *Q. Rev. Biophys.*, 39(01):1–55, 2006.

[75] Claire S Goldsbury, Garth JS Cooper, Kenneth N Goldie, Shirley A Müller, Etuate L Saafi, WTM Gruijters, Martin P Misur, Andreas Engel, Ueli Aebi, and Joerg Kistler. Polymorphic fibrillar assembly of human amylin. *Journal of structural biology*, 119(1):17–27, 1997.

[76] Sahar Bedrood, Yiyu Li, J Mario Isas, Balachandra G Hegde, Ulrich Baxa, Ian S Haworth, and Ralf Langen. Fibril structure of human islet amyloid polypeptide. *J. Biol. Chem.*, 287(8):5235–5241, 2012.

[77] Nathan A Bernhardt, Workalemahu M Berhanu, and Ulrich HE Hansmann. Mutations and seeding of amylin fibril-like oligomers. *J. Phys. Chem. B*, 117(50):16076–16085, 2013.

[78] Weixin Xu, Haibin Su, John ZH Zhang, and Yuguang Mu. Molecular dynamics simulation study on the molecular structures of the amylin fibril models. *J. Phys. Chem. B*, 116(48):13991–13999, 2012.

[79] Michele McDonald, Hayden Box, Wen Bian, Amy Kendall, Robert Tycko, and Gerald Stubbs. Fiber diffraction data indicate a hollow core for the alzheimer's aβ 3-fold symmetric fibril. *J. Mol. Biol.*, 423(3):454–461, 2012.

[80] N.V. Buchete, R. Tycko, and G. Hummer. Molecular Dynamics Simulations of Alzheimer's β-Amyloid Protofilaments. *J. Mol. Biol.*, 353(4):804–821, 2005.

[81] Chun Wu, Michael T Bowers, and Joan-Emma Shea. On the origin of the stronger binding of pib over thioflavin t to protofibrils of the alzheimer amyloid-β peptide: A molecular dynamics study. *Biophys. J.*, 100(5):1316–1324, 2011.

[82] J. Zhang and M. Muthukumar. Simulations of nucleation and elongation of amyloid fibrils. *J. Chem. Phys.*, 130:035102, 2009.

[83] S. Auer, F. Meersman, C.M. Dobson, and M. Vendruscolo. A generic mechanism of emergence of amyloid protofilaments from disordered oligomeric aggregates. *PLoS Computational Biology*, 4(11):e1000222, 2008.

[84] S. Auer, C.M. Dobson, M. Vendruscolo, and A. Maritan. Self-templated nucleation in peptide and protein aggregation. *Phys. Rev. Lett.*, 101(25):258101, 2008.

[85] Anders Irbäck, Sigurdur Ægir Jónsson, Niels Linnemann, Björn Linse, and Stefan Wallin. Aggregate geometry in amyloid fibril nucleation. *Phys. Rev. Lett.*, 110(5):058101, 2013.

[86] M.S. Li, N.T. Co, G. Reddy, C.K. Hu, J.E. Straub, and D. Thirumalai.

Factors Governing Fibrillogenesis of Polypeptide Chains Revealed by Lattice Models. *Phys. Rev. Lett.*, 105(21):218101, 2010.

[87] M.S. Li, D.K. Klimov, J.E. Straub, and D. Thirumalai. Probing the mechanisms of fibril formation using lattice models. *J. Chem. Phys.*, 129:175101, 2008.

[88] Ran Ni, Sanne Abeln, Marieke Schor, Martien A Cohen Stuart, and Peter G Bolhuis. Interplay between folding and assembly of fibril-forming polypeptides. *Phys. Rev. Lett.*, 111(5):058101, 2013.

[89] Sanne Abeln, Michele Vendruscolo, Christopher M Dobson, and Daan Frenkel. A simple lattice model that captures protein folding, aggregation and amyloid formation. *PloS one*, 9(1):e85185, 2014.

[90] R. Pellarin and A. Caflisch. Interpreting the aggregation kinetics of amyloid peptides. *J. Mol. Biol.*, 360(4):882–892, 2006.

[91] R. Pellarin, E. Guarnera, and A. Caflisch. Pathways and intermediates of amyloid fibril formation. *J. Mol. Biol.*, 374(4):917–924, 2007.

[92] Scott P Carmichael and M Scott Shell. A new multiscale algorithm and its application to coarse-grained peptide models for self-assembly. *J. Phys. Chem. B*, 116(29):8383–8393, 2012.

[93] M Scott Shell. The relative entropy is fundamental to multiscale and inverse thermodynamic problems. *J. Chem. Phys*, 129(144):108, 2008.

[94] Sergei Izvekov and Gregory A Voth. A multiscale coarse-graining method for biomolecular systems. *J. Phys. Chem. B*, 109(7):2469–2473, 2005.

[95] Dirk Reith, Mathias Pütz, and Florian Müller-Plathe. Deriving effective mesoscale potentials from atomistic simulations. *Journal of computational chemistry*, 24(13):1624–1636, 2003.

[96] Luca Monticelli, Senthil K Kandasamy, Xavier Periole, Ronald G Larson, D Peter Tieleman, and Siewert-Jan Marrink. The martini coarse-grained force field: extension to proteins. *J. Chem. Theory Comput.*, 4(5):819–834, 2008.

[97] Yassmine Chebaro, Samuela Pasquali, and Philippe Derreumaux. The coarse-grained opep force field for non-amyloid and amyloid proteins. *J. Phys. Chem. B*, 116(30):8741–8752, 2012.

[98] M. Cheon, I. Chang, and C.K. Hall. Extending the prime model for protein aggregation to all 20 amino acids. *Proteins*, 78(14):2950–2960, 2010.

[99] One-Sun Lee, Vince Cho, and George C Schatz. Modeling the self-assembly of peptide amphiphiles into fibers using coarse-grained molecular dynamics. *Nano Letters*, 12(9):4907–4913, 2012.

[100] Pim WJM Frederix, Rein V Ulijn, Neil T Hunt, and Tell Tuttle. Virtual screening for dipeptide aggregation: toward predictive tools for peptide self-assembly. *J. Phys. Chem. Lett.*, 2(19):2380–2384, 2011.

[101] Stefan Auer, Christopher M Dobson, and Michele Vendruscolo. Characterization of the nucleation barriers for protein aggregation and amyloid formation. *HFSP journal*, 1(2):137–146, 2007.

[102] Dimo Kashchiev and Stefan Auer. Nucleation of amyloid fibrils. *J. Chem. Phys.*, 132(21):215101, 2010.

[103] Raffaela Cabriolu and Stefan Auer. Amyloid fibrillation kinetics: insight from atomistic nucleation theory. *J. Mol. Biol.*, 411(1):275–285, 2011.

[104] Noah S Bieler, Tuomas PJ Knowles, Daan Frenkel, and Robert Vácha. Connecting macroscopic observables and microscopic assembly events in amyloid formation using coarse grained simulations. *PLoS computational biology*, 8(10):e1002692, 2012.

[105] Tricia R Serio, Anil G Cashikar, Anthony S Kowal, George J Sawicki, Jahan J Moslehi, Louise Serpell, Morton F Arnsdorf, and Susan L Lindquist. Nucleated conformational conversion and the replication of conformational information by a prion determinant. *Science*, 289(5483):1317–1321, 2000.

[106] Natalia Carulla, Min Zhou, Ernest Giralt, Carol V Robinson, and Christopher M Dobson. Structure and intermolecular dynamics of aggregates populated during amyloid fibril formation studied by hydrogen/deuterium exchange. *Accounts Chem. Res.*, 43(8):1072–1079, 2010.

[107] Satoko Matsumura, Keiko Shinoda, Mayumi Yamada, Satoshi Yokojima, Masafumi Inoue, Takayuki Ohnishi, Tetsuya Shimada, Kazuya Kikuchi, Dai Masui, Shigeki Hashimoto, et al. Two distinct amyloid β-protein (aβ) assembly pathways leading to oligomers and fibrils identified by combined fluorescence correlation spectroscopy, morphology, and toxicity analyses. *J. Biol. Chem.*, 286(13):11555–11562, 2011.

[108] Hikari Itoh-Watanabe, Miya Kamihira-Ishijima, Izuru Kawamura, Masashi Kondoh, Masamichi Nakakoshi, Michio Sato, and Akira Naito. Characterization of the spherical intermediates and fibril formation of hct in hepes

solution using solid-state 13 c-nmr and transmission electron microscopy. *Physical Chemistry Chemical Physics*, 15(39):16956–16964, 2013.

[109] Hung D Nguyen and Carol K Hall. Spontaneous fibril formation by polyalanines; discontinuous molecular dynamics simulations. *J. Am. Chem. Soc.*, 128(6):1890–1901, 2006.

[110] P.H. Nguyen, M.S. Li, G. Stock, J.E. Straub, and D. Thirumalai. Monomer adds to preformed structured oligomers of aβ-peptides by a two-stage dock-lock mechanism. *Proc. Natl. Acad. Sci.*, 104(1):111–116, 2007.

[111] J.E. Straub and D. Thirumalai. Principles governing oligomer formation in amyloidogenic peptides. *Curr. Opin. Struc. Biol.*, 20(2):187–195, 2010.

[112] W.P. Esler, E.R. Stimson, J.M. Jennings, H.V. Vinters, J.R. Ghilardi, J.P. Lee, P.W. Mantyh, and J.E. Maggio. Alzheimer's disease amyloid propagation by a template-dependent dock-lock mechanism. *Biochemistry*, 39(21):6288–6295, 2000.

[113] Tadato Ban, Masaru Hoshino, Satoshi Takahashi, Daizo Hamada, Kazuhiro Hasegawa, Hironobu Naiki, and Yuji Goto. Direct observation of aβ amyloid fibril growth and inhibition. *J. Mol. Biol.*, 344(3):757–767, 2004.

[114] Takahiro Yamaguchi, Katsumi Matsuzaki, and Masaru Hoshino. Interaction between soluble aβ-(1–40) monomer and aβ-(1–42) fibrils probed by paramagnetic relaxation enhancement. *FEBS letters*, 587(6):620–624, 2013.

[115] Rita Carrotta, Mauro Manno, Donatella Bulone, Vincenzo Martorana, and Pier Luigi San Biagio. Protofibril formation of amyloid β-protein at low ph

via a non-cooperative elongation mechanism. *J. Biol. Chem.*, 280(34):30001–30008, 2005.

[116] Mookyung Cheon, Iksoo Chang, and Carol K Hall. Spontaneous formation of twisted aβ(16–22) fibrils in large-scale molecular-dynamics simulations. *Biophys. J.*, 101(10):2493–2501, 2011.

[117] Mookyung Cheon, Iksoo Chang, and Carol K Hall. Influence of temperature on formation of perfect tau fragment fibrils using prime20/dmd simulations. *Protein Sci.*, 21(10):1514–1527, 2012.

[118] Jesper Sørensen, Xavier Periole, Katrine K Skeby, Siewert-J Marrink, and Birgit Schiøtt. Protofibrillar assembly toward the formation of amyloid fibrils. *J. Phys. Chem. Lett.*, 2(19):2385–2390, 2011.

[119] Raffaella Paparcone, Steven W Cranford, and Markus J Buehler. Self-folding and aggregation of amyloid nanofibrils. *Nanoscale*, 3(4):1748–1755, 2011.

[120] Gwonchan Yoon, Jinhak Kwak, Jae In Kim, Sungsoo Na, and Kilho Eom. Mechanical characterization of amyloid fibrils using coarse-grained normal mode analysis. *Advanced Functional Materials*, 21(18):3454–3463, 2011.

[121] Torleif Härd. Amyloid fibrils: Formation, polymorphism and inhibition. *J. Phys. Chem. Lett.*, 5(3):607–614, 2014.

[122] Samuel IA Cohen, Sara Linse, Leila M Luheshi, Erik Hellstrand, Duncan A White, Luke Rajah, Daniel E Otzen, Michele Vendruscolo, Christopher M Dobson, and Tuomas PJ Knowles. Proliferation of amyloid-β42 aggregates occurs through a secondary nucleation mechanism. *Proc. Natl. Acad. Sci.*, 110(24):9758–9763, 2013.

[123] Samuel IA Cohen, Michele Vendruscolo, Mark E Welland, Christopher M Dobson, Eugene M Terentjev, and Tuomas PJ Knowles. Nucleated polymerization with secondary pathways. i. time evolution of the principal moments. *J. Chem. Phys.*, 135(6):065105, 2011.

[124] Tuomas PJ Knowles, Christopher A Waudby, Glyn L Devlin, Samuel IA Cohen, Adriano Aguzzi, Michele Vendruscolo, Eugene M Terentjev, Mark E Welland, and Christopher M Dobson. An analytical solution to the kinetics of breakable filament assembly. *Science*, 326(5959):1533–1537, 2009.

[125] Monica Bucciantini, Stefania Rigacci, and Massimo Stefani. Amyloid aggregation: Role of biological membranes and the aggregate-membrane system. *J. Phys. Chem. Lett.*, 5(2):517–527, 2014.

[126] Mijo Simunovic, Carsten Mim, Thomas C Marlovits, Guenter Resch, Vinzenz M Unger, and Gregory A Voth. Protein-mediated transformation of lipid vesicles into tubular networks. *Biophys. J.*, 105(3):711–719, 2013.

[127] Andrew Hung and Irene Yarovsky. Inhibition of peptide aggregation by lipids: insights from coarse-grained molecular simulations. *Journal of Molecular Graphics and Modelling*, 29(5):597–607, 2011.

[128] Ran Friedman and Amedeo Caflisch. Surfactant effects on amyloid aggregation kinetics. *J. Mol. Biol.*, 414(2):303–312, 2011.

[129] Mijo Simunovic, Anand Srivastava, and Gregory A Voth. Linear aggregation of proteins on the membrane as a prelude to membrane remodeling. *Proc. Natl. Acad. Sci.*, 110(51):20396–20401, 2013.

[130] Martina Pannuzzo, Antonio Raudino, Danilo Milardi, Carmelo La Rosa, and

Mikko Karttunen. α-helical structures drive early stages of self-assembly of amyloidogenic amyloid polypeptide aggregate formation in membranes. *Scientific reports*, 3, 2013.

[131] Hualin Li and Alemayehu A Gorfe. Aggregation of lipid-anchored full-length h-ras in lipid bilayers: Simulations with the martini force field. *PloS one*, 8(7):e71018, 2013.

[132] Robert Vácha and Daan Frenkel. Simulations suggest possible novel membrane pore structure. *Langmuir*, 30(5):1304–1310, 2014.

[133] Daniel L Parton, Jochen W Klingelhoefer, and Mark SP Sansom. Aggregation of model membrane proteins, modulated by hydrophobic mismatch, membrane curvature, and protein class. *Biophys. J.*, 101(3):691–699, 2011.

[134] G. Brannigan, P.F. Philips, and F.L.H. Brown. Flexible lipid bilayers in implicit solvent. *Phys. Rev. E*, 72(1):011915, 2005.

[135] Michele FM Sciacca, Samuel A Kotler, Jeffrey R Brender, Jennifer Chen, Dong-kuk Lee, and Ayyalusamy Ramamoorthy. Two-step mechanism of membrane disruption by aβ through membrane fragmentation and pore formation. *Biophys. J.*, 103(4):702–710, 2012.

[136] Maarten FM Engel, Lucie Khemtémourian, Cécile C Kleijer, Hans JD Meeldijk, Jet Jacobs, Arie J Verkleij, Ben de Kruijff, J Antoinette Killian, and Jo WM Höppener. Membrane damage by human islet amyloid polypeptide through fibril growth at the membrane. *Proc. Natl. Acad. Sci.*, 105(16):6033–6038, 2008.

[137] Ping Cao, Andisheh Abedini, Hui Wang, Ling-Hsien Tu, Xiaoxue Zhang,

Ann Marie Schmidt, and Daniel P Raleigh. Islet amyloid polypeptide toxicity and membrane interactions. *Proc. Natl. Acad. Sci.*, 110(48):19279–19284, 2013.

[138] Jun Zhao, Yin Luo, Hyunbum Jang, Xiang Yu, Guanghong Wei, Ruth Nussinov, and Jie Zheng. Probing ion channel activity of human islet amyloid polypeptide (amylin). *Biochimica et Biophysica Acta (BBA)-Biomembranes*, 1818(12):3121–3130, 2012.

[139] Chetan Poojari, Dequan Xiao, Victor S Batista, and Birgit Strodel. Membrane permeation induced by aggregates of human islet amyloid polypeptides. *Biophys. J.*, 105(10):2323–2332, 2013.

[140] Yan Jia, Zhenyu Qian, Yun Zhang, and Guanghong Wei. Adsorption and orientation of human islet amyloid polypeptide (hiapp) monomer at anionic lipid bilayers: Implications for membrane-mediated aggregation. *International journal of molecular sciences*, 14(3):6241–6258, 2013.

[141] Mojie Duan, Jue Fan, and Shuanghong Huo. Conformations of islet amyloid polypeptide monomers in a membrane environment: Implications for fibril formation. *PloS one*, 7(11):e47150, 2012.

[142] Ravi Prakash Reddy Nanga, Jeffrey R Brender, Subramanian Vivekanandan, and Ayyalusamy Ramamoorthy. Structure and membrane orientation of iapp in its natively amidated form at physiological ph in a membrane environment. *Biochimica et Biophysica Acta (BBA)-Biomembranes*, 1808(10):2337–2342, 2011.

[143] Ravi Prakash Reddy Nanga, Jeffrey R Brender, Jiadi Xu, Kevin Hartman, Vivekanandan Subramanian, and Ayyalusamy Ramamoorthy. Three-

dimensional structure and orientation of rat islet amyloid polypeptide protein in a membrane environment by solution nmr spectroscopy. *J. Am. Chem. Soc.*, 131(23):8252–8261, 2009.

[144] A Morriss-Andrews, FLH Brown, and J-E Shea. Mempep paper. 2014.

[145] A. Morriss-Andrews, G. Bellesia, and J.E. Shea. β-sheet propensity controls the kinetic pathways and morphologies of seeded peptide aggregation. *J. Chem. Phys.*, 137:145104, 2012.

[146] A. Morriss-Andrews and J.E. Shea. Kinetic pathways to peptide aggregation on surfaces: The effects of β-sheet propensity and surface attraction. *J. Chem. Phys.*, 136:065103, 2012.

[147] A. Morriss-Andrews, G. Bellesia, and J.-E. Shea. Effects of surface interactions on peptide aggregate morphology. *J. Chem. Phys.*, 135(085102), 2011.

[148] M.C. Watson, E.S. Penev, P.M. Welch, and F.L.H. Brown. Thermal fluctuations in shape, thickness, and molecular orientation in lipid bilayers. *J. Chem. Phys.*, 135(24):244701–244701, 2011.

[149] Max C Watson, Alex Morriss-Andrews, Paul M Welch, and Frank LH Brown. Thermal fluctuations in shape, thickness, and molecular orientation in lipid bilayers. ii. finite surface tensions. *J. Chem. Phys.*, 139(8):084706, 2013.

[150] Max C Watson, Erik G Brandt, Paul M Welch, and Frank LH Brown. Determining biomembrane bending rigidities from simulations of modest size. *Phys. Rev. Lett.*, 109(2):028102, 2012.

[151] G. Brannigan and F.L.H. Brown. Contributions of gaussian curvature and nonconstant lipid volume to protein deformation of lipid bilayers. *Biophys. J.*, 92(3):864–876, 2007.

[152] G. Brannigan and F.L.H. Brown. A consistent model for thermal fluctuations and protein-induced deformations in lipid bilayers. *Biophys. J.*, 90(5):1501–1520, 2006.

[153] John E Straub and D Thirumalai. Membrane–protein interactions are key to understanding amyloid formation. *J. Phys. Chem. Lett.*, 5(3):633–635, 2014.

[154] Elisa Evangelisti, Cristina Cecchi, Roberta Cascella, Caterina Sgromo, Matteo Becatti, Christopher M. Dobson, Fabrizio Chiti, and Massimo Stefani. Membrane lipid composition and its physicochemical properties define cell vulnerability to aberrant protein oligomers. *J. Cell Sci.*, 125(10):2416–2427, 2012.

[155] Henning Mueller, Hans-Jürgen Butt, and Ernst Bamberg. Adsorption of membrane-associated proteins to lipid bilayers studied with an atomic force microscope: myelin basic protein and cytochrome c. *J. Phys. Chem. B*, 104(18):4552–4559, 2000.

[156] William L Jorgensen, Jayaraman Chandrasekhar, Jeffry D Madura, Roger W Impey, and Michael L Klein. Comparison of simple potential functions for simulating liquid water. *J. Chem. Phys.*, 79(2):926–935, 1983.

[157] HJC Berendsen, JR Grigera, and TP Straatsma. The missing term in effective pair potentials. *J. Phys. Chem.*, 91(24):6269–6271, 1987.

[158] I. Brovchenko, G. Singh, and R. Winter. Aggregation of Amyloidogenic Peptides near Hydrophobic and Hydrophilic Surfaces. *Langmuir*, 25(14):8111–8116, 2009.

[159] V. Castells, S. Yang, and P.R. Van Tassel. Surface-induced conformational changes in lattice model proteins by Monte Carlo simulation. *Phys. Rev. E*, 65(3):31912, 2002.

[160] C.E. Giacomelli and W. Norde. Conformational Changes of the Amyloid β-Peptide (1–40) Adsorbed on Solid Surfaces. *Macromolecular bioscience*, 5(5):401–407, 2005.

[161] J.J. Gray. The interaction of proteins with solid surfaces. *Curr. Opin. Struc. Biol.*, 14(1):110–115, 2004.

[162] D. Horinek, A. Serr, M. Geisler, T. Pirzer, U. Slotta, S.Q. Lud, J.A. Garrido, T. Scheibel, T. Hugel, and R.R. Netz. Peptide adsorption on a hydrophobic surface results from an interplay of solvation, surface, and intrapeptide forces. *Proc. Natl. Acad. Sci.*, 105(8):2842, 2008.

[163] S. Linse, C. Cabaleiro-Lago, W.F. Xue, I. Lynch, S. Lindman, E. Thulin, S.E. Radford, and K.A. Dawson. Nucleation of protein fibrillation by nanoparticles. *Proc. Natl. Acad. Sci.*, 104(21):8691, 2007.

[164] M.J. McMasters, R.P. Hammer, and R.L. McCarley. Surface-induced aggregation of β amyloid peptide by ω-substituted alkanethiol monolayers supported on gold. *Langmuir*, 21(10):4464–4470, 2005.

[165] A.A. Mungikar and D. Forciniti. Conformational changes of peptides

at solid/liquid interfaces: A Monte Carlo study. *Biomacromolecules*, 5(6):2147–2159, 2004.

[166] D. Pellenc, O. Gallet, and H. Berry. Adsorption-induced conformational changes in protein diffusion-aggregation surface assemblies. *Phys. Rev. E*, 72(5):51904, 2005.

[167] C. Whitehouse, J. Fang, A. Aggeli, M. Bell, R. Brydson, C.W.G. Fishwick, J.R. Henderson, C.M. Knobler, R.W. Owens, N.H. Thomson, et al. Adsorption and Self-Assembly of Peptides on Mica Substrates. *Angewandte Chemie*, 117(13):2001–2004, 2005.

[168] S. Sharma, B.J. Berne, and S.K. Kumar. Thermal and Structural Stability of Adsorbed Proteins. *Biophys. J.*, 99(4):1157–1165, 2010.

[169] Z. Zhuang, A.I. Jewett, S. Kuttimalai, G. Bellesia, S. Gnanakaran, and J.-E. Shea. Assisted peptide folding by surface pattern recognition. *Biophys. J.*, 100(5):1306–1315, 2011.

[170] M. Stefani. Generic cell dysfunction in neurodegenerative disorders: role of surfaces in early protein misfolding, aggregation, and aggregate cytotoxicity. *Neuroscientist*, 13(5):519, 2007.

[171] M. Bucciantini, E. Giannoni, F. Chiti, F. Baroni, L. Formigli, J. Zurdo, N. Taddei, G. Ramponi, C.M. Dobson, and M. Stefani. Inherent toxicity of aggregates implies a common mechanism for protein misfolding diseases. *Nature*, 416(6880):507–511, 2002.

[172] S. Auer, A. Trovato, and M. Vendruscolo. A condensation-ordering mech-

anism in nanoparticle-catalyzed peptide aggregation. *PLoS Computational Biology*, 5(8):e1000458, 2009.

[173] S. Boateng, S.S. Lateef, C. Crot, D. Motlagh, T. Desai, A.M. Samarel, B. Russell, and L. Hanley. Peptides bound to silicone membranes and 3D microfabrication for cardiac cell culture. *Advanced materials*, 14(6):461–463, 2002.

[174] S. Zhang. Fabrication of novel biomaterials through molecular self-assembly. *Nature Biotechnology*, 21(10):1171–1178, 2003.

[175] S. Zhang, D.M. Marini, W. Hwang, and S. Santoso. Design of nanostructured biological materials through self-assembly of peptides and proteins. *Current Opinion in Chemical Biology*, 6(6):865–871, 2002.

[176] R.A. Latour. Biomaterials: Protein-surface interactions. *Encyclopedia of Biomaterials and Biomedical Engineering*, pages 1–15, 2005.

[177] K.C. Dee, D.A. Puleo, and R. Bizios. *An introduction to tissue-biomaterial interactions*. LibreDigital, 2002.

[178] P. Asuri, S.S. Bale, S.S. Karajanagi, and R.S. Kane. The protein-nanomaterial interface. *Current Opinion in Biotechnology*, 17(6):562–568, 2006.

[179] N.C. Seeman and A.M. Belcher. Emulating biology: building nanostructures from the bottom up. *Proc. Natl. Acad. Sci.*, 99(Suppl 2):6451, 2002.

[180] M. Cecchini, F. Rao, M. Seeber, and A. Caflisch. Replica exchange molecular dynamics simulations of amyloid peptide aggregation. *J. Chem. Phys.*, 121:10748, 2004.

[181] Tomasz Kowalewski and David M. Holtzman. In situ atomic force microscopy study of alzheimer's β-amyloid peptide on different substrates: New insights into mechanism of β-sheet formation. *Proc. Natl. Acad. Sci.*, 96(7):3688–3693, 1999.

[182] Adrian Keller, Monika Fritzsche, Ye-Ping Yu, Qian Liu, Yan-Mei Li, Mingdong Dong, and Flemming Besenbacher. Influence of hydrophobicity on the surface-catalyzed assembly of the islet amyloid polypeptide. *ACS Nano*, 5(4):2770–2778, 2011.

[183] Dusan Losic, Lisandra L. Martin, Marie-Isabel Aguilar, and David H. Small. β-amyloid fibril formation is promoted by step edges of highly oriented pyrolytic graphite. *Peptide Science*, 84(5):519–526, 2006.

[184] M. Zhu, P.O. Souillac, C. Ionescu-Zanetti, S.A. Carter, and A.L. Fink. Surface-catalyzed amyloid fibril formation. *J. Biol. Chem.*, 277(52):50914, 2002.

[185] Chanki Ha and Chan Beum Park. Ex situ atomic force microscopy analysis of β-amyloid self-assembly and deposition on a synthetic template. *Langmuir*, 22(16):6977–6985, 2006.

[186] Chanki Ha and Chan Beum Park. Template-directed self-assembly and growth of insulin amyloid fibrils. *Biotechnology and Bioengineering*, 90(7):848–855, 2005.

[187] C.H. Davis and M.L. Berkowitz. Interaction between amyloid-beta(1-42) peptide and phospholipid bilayers: A molecular dynamics study. *Biophys. J.*, 96(3):785–797, 2009.

[188] Charles H. Davis and Max L. Berkowitz. Structure of the amyloid-β (142) monomer absorbed to model phospholipid bilayers: A molecular dynamics study. *J. Phys. Chem. B*, 113(43):14480–14486, 2009.

[189] Jean-Marc Crowet, Laurence Lins, Ingrid Dupiereux, Benaïssa Elmoualija, Aurélien Lorin, Benoit Charloteaux, Vincent Stroobant, Ernst Heinen, and Robert Brasseur. Tilted properties of the 67–78 fragment of α-synuclein are responsible for membrane destabilization and neurotoxicity. *Proteins*, 68(4):936–947, 2007.

[190] H. Jang, J. Zheng, and R. Nussinov. Models of β-amyloid ion channels in the membrane suggest that channel formation in the bilayer is a dynamic process. *Biophys. J.*, 93(6):1938–1949, 2007.

[191] V. Knecht. β-hairpin folding by a model amyloid peptide in solution and at an interface. *J. Phys. Chem. B*, 112(31):9476–9483, 2008.

[192] J.A. Lemkul and D.R. Bevan. Perturbation of membranes by the amyloid β-peptide–a molecular dynamics study. *Febs Journal*, 276(11):3060–3075, 2009.

[193] N. Miyashita, J.E. Straub, and D. Thirumalai. Structures of β-amyloid peptide 1-40, 1-42, and 1-55 the 672-726 fragment of app in a membrane environment with implications for interactions with γ-secretase. *J. Am. Chem. Soc.*, 131(49):17843–17852, 2009.

[194] D.L. Mobley, D.L. Cox, R.R.P. Singh, M.W. Maddox, and M.L. Longo. Modeling amyloid β-peptide insertion into lipid bilayers. *Biophys. J.*, 86(6):3585–3597, 2004.

[195] Y. Xu, J. Shen, X. Luo, W. Zhu, K. Chen, J. Ma, and H. Jiang. Conformational transition of amyloid β-peptide. *Proc. Natl. Acad. Sci.*, 102(15):5403, 2005.

[196] A. Nikolic, S. Baud, S. Rauscher, and R. Pomès. Molecular mechanism of β-sheet self-organization at water-hydrophobic interfaces. *Proteins*, 79(1):1–22, 2011.

[197] S. Auer and D. Kashchiev. Phase diagram of α-helical and β-sheet forming peptides. *Phys. Rev. Lett.*, 104(16):168105, 2010.

[198] R. Friedman, R. Pellarin, and A. Caflisch. Amyloid aggregation on lipid bilayers and its impact on membrane permeability. *J. Mol. Biol.*, 387(2):407–415, 2009.

[199] Kris Pauwels, Thomas L. Williams, Kyle L. Morris, Wim Jonckheere, Annelies Vandersteen, Geoff Kelly, Joost Schymkowitz, Frederic Rousseau, Annalisa Pastore, Louise C. Serpell, and Kerensa Broersen. Structural basis for increased toxicity of pathological Aβ42: Aβ40 ratios in alzheimer disease. *J. Biol. Chem.*, 287(8):5650–5660, 2012.

[200] C. Wasmer, A. Zimmer, R. Sabaté, A. Soragni, S.J. Saupe, C. Ritter, and B.H. Meier. Structural similarity between the prion domain of het-s and a homologue can explain amyloid cross-seeding in spite of limited sequence identity. *J. Mol. Biol.*, 402(2):311–325, 2010.

[201] Y. Furukawa, K. Kaneko, G. Matsumoto, M. Kurosawa, and N. Nukina. Cross-seeding fibrillation of q/n-rich proteins offers new pathomechanism of polyglutamine diseases. *Journal of Neuroscience*, 29(16):5153–5162, 2009.

[202] S. Schilling, T. Lauber, M. Schaupp, S. Manhart, E. Scheel, G. Böhm, and H.U. Demuth. On the seeding and oligomerization of pglu-amyloid peptides (in vitro). *Biochemistry*, 45(41):12393–12399, 2006.

[203] Melanie R. Nilsson, Miles Driscoll, and Daniel P. Raleigh. Low levels of asparagine deamidation can have a dramatic effect on aggregation of amyloidogenic peptides: Implications for the study of amyloid formation. *Protein Sci.*, 11(2):342–349, 2002.

[204] J.D. Harper and P.T. Lansbury Jr. Models of amyloid seeding in Alzheimer's disease and scrapie: mechanistic truths and physiological consequences of the time-dependent solubility of amyloid proteins. *Annu. Rev. Biochem.*, 66(1):385–407, 1997.

[205] I. Kuperstein, K. Broersen, I. Benilova, J. Rozenski, W. Jonckheere, M. Debulpaep, A. Vandersteen, I. Segers-Nolten, K. Van Der Werf, V. Subramaniam, Dries Braeken, Geert Callewaert, Carmen Bartic, Rudi D'Hooge, Ivo Cristiano Martins, Frederic Rousseau, Joost Schymkowitz, and Bart De Strooper. Neurotoxicity of alzheimer's disease Aβ peptides is induced by small changes in the Aβ42 to Aβ40 ratio. *EMBO journal*, 29(19):3408–3420, 2010.

[206] Y. Yoshiike, D.H. Chui, T. Akagi, N. Tanaka, and A. Takashima. Specific compositions of amyloid-β peptides as the determinant of toxic β-aggregation. *J. Biol. Chem.*, 278(26):23648–23655, 2003.

[207] C.E. MacPhee and C.M. Dobson. Formation of mixed fibrils demonstrates the generic nature and potential utility of amyloid nanostructures. *J. Am. Chem. Soc.*, 122(51):12707–12713, 2000.

[208] A.H. DePace and J.S. Weissman. Origins and kinetic consequences of diversity in Sup35 yeast prion fibers. *Nature Structural & Molecular Biology*, 9(5):389–396, 2002.

[209] F. Massi and J.E. Straub. Energy landscape theory for alzheimer's amyloid β-peptide fibril elongation. *Proteins*, 42(2):217–229, 2001.

[210] H.D. Nguyen and C.K. Hall. Molecular dynamics simulations of spontaneous fibril formation by random-coil peptides. *Proc. Natl. Acad. Sci.*, 101(46):16180–16185, 2004.

[211] D.P. Hong and A.L. Fink. Independent heterologous fibrillation of insulin and its b-chain peptide. *Biochemistry*, 44(50):16701–16709, 2005.

[212] M.R. Nilsson. Techniques to study amyloid fibril formation in vitro. *Methods*, 34(1):151–160, 2004.

[213] S. Chen, V. Berthelier, J.B. Hamilton, Brian O'Nuallain, and R. Wetzel. Amyloid-like features of polyglutamine aggregates and their assembly kinetics. *Biochemistry*, 41(23):7391–7399, 2002.

[214] H. Han, P.H. Weinreb, and P.T. Lansbury. The core alzheimer's peptide nac forms amyloid fibrils which seed and are seeded by β-amyloid: is nac a common trigger or target in neurodegenerative disease? *Chem. Biol.*, 2(3):163–169, 1995.

[215] J.T. Jarrett, E.P. Berger, and P.T. Lansbury Jr. The carboxy terminus of the. beta. amyloid protein is critical for the seeding of amyloid formation: Implications for the pathogenesis of alzheimer's disease. *Biochemistry*, 32(18):4693–4697, 1993.

[216] T. Scheibel, J. Bloom, and S.L. Lindquist. The elongation of yeast prion fibers involves separable steps of association and conversion. *Proc. Natl. Acad. Sci.*, 101(8):2287, 2004.

[217] D. Matthes, V. Gapsys, V. Daebel, and B.L. de Groot. Mapping the conformational dynamics and pathways of spontaneous steric zipper peptide oligomerization. *PloS one*, 6(5):e19129, 2011.

[218] S.A. Petty and S.M. Decatur. Intersheet rearrangement of polypeptides during nucleation of β-sheet aggregates. *Proc. Natl. Acad. Sci.*, 102(40):14272, 2005.

[219] A. Magno, R. Pellarin, and A. Caflisch. Mechanisms and kinetics of amyloid aggregation investigated by a phenomenological coarse-grained model. *Computational Modeling of Biological Systems*, pages 191–214, 2012.

[220] Carla E. Giacomelli and Willem Norde. Influence of hydrophobic teflon particles on the structure of amyloid β-peptide. *Biomacromolecules*, 4(6):1719–1726, 2003.

[221] Kenji Sasahara, Kenichi Morigaki, and Kyoko Shinya. Effects of membrane interaction and aggregation of amyloid β-peptide on lipid mobility and membrane domain structure. *Phys. Chem. Chem. Phys.*, 15(23):8929–8939, 2013.

[222] Janine Seeliger, Florian Evers, Christoph Jeworrek, Shobhna Kapoor, Katrin Weise, Erika Andreetto, Metin Tolan, Aphrodite Kapurniotu, and Roland Winter. Cross-amyloid interaction of aβ and iapp at lipid membranes. *Angew. Chem. Int. Edit.*, 51(3):679–683, 2012.

[223] Lei Shen, Takuji Adachi, David Vanden Bout, and X-Y Zhu. A mobile

precursor determines amyloid-β peptide fibril formation at interfaces. *J. Am. Chem. Soc.*, 134(34):14172–14178, 2012.

[224] Lan Zhang, Jian Zhong, Lixin Huang, Lijun Wang, Yuankai Hong, and Yinlin Sha. Parallel-oriented fibrogenesis of a β-sheet forming peptide on supported lipid bilayers. *J. Phys. Chem. B*, 112(30):8950–8954, 2008.

[225] John J Kremer and Regina M Murphy. Kinetics of adsorption of β-amyloid peptide aβ (1–40) to lipid bilayers. *J. Biochem. Bioph. Meth.*, 57(2):159–169, 2003.

[226] John J Kremer, Monica M Pallitto, Daniel J Sklansky, and Regina M Murphy. Correlation of β-amyloid aggregate size and hydrophobicity with decreased bilayer fluidity of model membranes. *Biochemistry*, 39(33):10309–10318, 2000.

[227] D.H.J. Lopes, A. Meister, A. Gohlke, A. Hauser, A. Blume, and R. Winter. Mechanism of islet amyloid polypeptide fibrillation at lipid interfaces studied by infrared reflection absorption spectroscopy. *Biophys. J.*, 93(9):3132 – 3141, 2007.

[228] Himanshu Khandelia, John H. Ipsen, and Ole G. Mouritsen. The impact of peptides on lipid membranes. *BBA-Biomembranes*, 1778(7–8):1528 – 1536, 2008. Protein Modulation of Membrane Structure.

[229] SaraM. Butterfield and HilalA. Lashuel. Amyloidogenic protein–membrane interactions: Mechanistic insight from model systems. *Angew. Chem. Int. Edit.*, 49(33):5628–5654, 2010.

[230] Hilal A. Lashuel and Peter T. Lansbury. Are amyloid diseases caused by protein aggregates that mimic bacterial pore-forming toxins? *Q. Rev. Biophys.*, 39:167–201, 5 2006.

[231] Anna Kastorna, Valeriya Trusova, Galyna Gorbenko, and Paavo Kinnunen. Membrane effects of lysozyme amyloid fibrils. *Chem. Phys. Lipids*, 165(3):331 – 337, 2012.

[232] Lilia Milanesi, Tania Sheynis, Wei-Feng Xue, Elena V Orlova, Andrew L Hellewell, Raz Jelinek, Eric W Hewitt, Sheena E Radford, and Helen R Saibil. Direct three-dimensional visualization of membrane disruption by amyloid fibrils. *Proc. Natl. Acad. Sci.*, 109(50):20455–20460, 2012.

[233] Kathleen A. Burke, Elizabeth A. Yates, and Justin Legleiter. Amyloid-forming proteins alter the local mechanical properties of lipid membranes. *Biochemistry*, 52(5):808–817, 2013.

[234] Michael K Lee, Wanda Stirling, Yanqun Xu, Xueying Xu, Dike Qui, Allen S Mandir, Ted M Dawson, Neal G Copeland, Nancy A Jenkins, and Don L Price. Human α-synuclein-harboring familial parkinson's disease-linked ala-53 thr mutation causes neurodegenerative disease with α-synuclein aggregation in transgenic mice. *Proc. Natl. Acad. Sci.*, 99(13):8968–8973, 2002.

[235] Seongwon Kim and Dmitri K Klimov. Binding to the lipid monolayer induces conformational transition in aβ monomer. *J. Mol. Model.*, 19(2):737–750, 2013.

[236] Xiang Yu, Qiuming Wang, Qingfen Pan, Feimeng Zhou, and Jie Zheng. Molecular interactions of alzheimer amyloid-β oligomers with neutral and

negatively charged lipid bilayers. *Phys. Chem. Chem. Phys.*, 15(23):8878–8889, 2013.

[237] Xiang Yu and Jie Zheng. Cholesterol promotes the interaction of alzheimer β-amyloid monomer with lipid bilayer. *J. Mol. Biol.*, 421(4):561–571, 2012.

[238] Justin A Lemkul and David R Bevan. Lipid composition influences the release of alzheimer's amyloid β-peptide from membranes. *Protein Sci.*, 20(9):1530–1545, 2011.

[239] Kshitij Gupta, Hyunbum Jang, Kevin Harlen, Anu Puri, Ruth Nussinov, Joel P Schneider, and Robert Blumenthal. Mechanism of membrane permeation induced by synthetic β-hairpin peptides. *Biophys. J.*, 105(9):2093–2103, 2013.

[240] Fernando Terán Arce, Hyunbum Jang, Srinivasan Ramachandran, Preston B Landon, Ruth Nussinov, and Ratnesh Lal. Polymorphism of amyloid β peptide in different environments: implications for membrane insertion and pore formation. *Soft Matter*, 7(11):5267–5273, 2011.

[241] Birgit Strodel, Jason WL Lee, Christopher S Whittleston, and David J Wales. Transmembrane structures for alzheimer's aβ1- 42 oligomers. *J. Am. Chem. Soc.*, 132(38):13300–13312, 2010.

[242] Afra Panahi and Michael Feig. Dynamic heterogeneous dielectric generalized born (dhdgb): An implicit membrane model with a dynamically varying bilayer thickness. *J. Chem. Theory Comput.*, 9(3):1709–1719, 2013.

[243] Benjamin A Hall, Alan P Chetwynd, and Mark SP Sansom. Exploring

peptide-membrane interactions with coarse-grained md simulations. *Biophys. J.*, 100(8):1940–1948, 2011.

[244] Luca Monticelli, D Peter Tieleman, and Patrick FJ Fuchs. Interpretation of ^{2}h-nmr experiments on the orientation of the transmembrane helix walp23 by computer simulations. *Biophys. J.*, 99(5):1455–1464, 2010.

[245] Daniel A Holdbrook, Yuk Ming Leung, Thomas J Piggot, Phedra Marius, Philip TF Williamson, and Syma Khalid. Stability and membrane orientation of the fukutin transmembrane domain: a combined multiscale molecular dynamics and circular dichroism study. *Biochemistry*, 49(51):10796–10802, 2010.

[246] Chetan Poojari, Andreas Kukol, and Birgit Strodel. How the amyloid-peptide and membranes affect each other: An extensive simulation study. *BBA-Biomembranes*, 1828(2):327 – 339, 2013.

[247] Gregoria Illya and Markus Deserno. Coarse-grained simulation studies of peptide-induced pore formation. *Biophys. J.*, 95(9):4163–4173, 2008.

[248] Yun Zhang, Yin Luo, Yonghua Deng, Yuguang Mu, and Guanghong Wei. Lipid interaction and membrane perturbation of human islet amyloid polypeptide monomer and dimer by molecular dynamics simulations. *PloS one*, 7(5):e38191, 2012.

[249] Li Na Zhao, See-Wing Chiu, Jérôme Benoit, Lock Yue Chew, and Yuguang Mu. Amyloid β peptides aggregation in a mixed membrane bilayer: a molecular dynamics study. *J. Phys. Chem. B*, 115(42):12247–12256, 2011.

[250] Charles H Davis and Max L Berkowitz. A molecular dynamics study of the

early stages of amyloid-β (1–42) oligomerization: The role of lipid membranes. *Proteins*, 78(11):2533–2545, 2010.

[251] Erin M Phelps and Carol K Hall. Structural transitions and oligomerization along polyalanine fibril formation pathways from computer simulations. *Proteins*, 80(6):1582–1597, 2012.

[252] Yaakov Levy and José N Onuchic. Mechanisms of protein assembly: lessons from minimalist models. *Accounts Chem. Res.*, 39(2):135–142, 2006.

[253] Siewert J Marrink, Alex H de Vries, and Alan E Mark. Coarse grained model for semiquantitative lipid simulations. *J. Phys. Chem. B*, 108(2):750–760, 2004.

[254] Scott E Feller and Richard W Pastor. Constant surface tension simulations of lipid bilayers: the sensitivity of surface areas and compressibilities. *J. Chem. Phys.*, 111(3):1281–1287, 1999.

[255] S. A. Safran. *Statistical Thermodynamics of Surfaces, Interfaces and Membranes*. Westview Press, Boulder, CO, 1994.

[256] F. L. H. Brown. Continuum simulations of biomembrane dynamics and the importance of hydrodynamic effects. *Q. Rev. Biophys.*, 44:391–432, 2011.

[257] Roland R Netz and P Pincus. Inhomogeneous fluid membranes: segregation, ordering, and effective rigidity. *Phys. Rev. E*, 52(4):4114, 1995.

[258] J. K. Sigurdsson, F. L. H. Brown, and P. J. Atzberger. Hybrid continuum-particle method for fluctuating lipid bilayer membranes with diffusing protein inclusions. *J. Comp. Phys.*, 252:65–85, 2013.

[259] George Khelashvili, Benjamin Kollmitzer, Peter Heftberger, Georg Pabst, and Daniel Harries. Calculating the bending modulus for multicomponent lipid membranes in different thermodynamic phases. *J. Chem. Theory Comput.*, 9(9):3866–3871, 2013.

[260] Galyna Gorbenko and Valeriya Trusova. Protein aggregation in a membrane environment. volume 84 of *Adv. Protein Chem. Struc. Biol.*, pages 113 – 142. Academic Press, 2011.

[261] He-Jin Lee, Chan Choi, and Seung-Jae Lee. Membrane-bound -synuclein has a high aggregation propensity and the ability to seed the aggregation of the cytosolic form. *J. Biol. Chem.*, 277(1):671–678, 2002.

[262] K. Matsuzaki and C. Horikiri. Interactions of amyloid β-peptide (1– 40) with ganglioside-containing membranes. *Biochemistry*, 38:4137–4142, 1999.

[263] Yi-Jiong Zhang, Jing-Ming Shi, Cai-Juan Bai, Han Wang, Hai-Yun Li, Yi Wu, and Shang-Rong Ji. Intra-membrane oligomerization and extra-membrane oligomerization of amyloid-β peptide are competing processes as a result of distinct patterns of motif interplay. *J. Biol. Chem.*, 287(1):748–756, 2012.

[264] Zhirong Liu and Hue Sun Chan. Solvation and desolvation effects in protein folding: Native flexibility, kinetic cooperativity and enthalpic barriers under isostability conditions. *Phys. Biol.*, 2(4):S75, 2005.

[265] Marcus G Martin and J Ilja Siepmann. Transferable potentials for phase equilibria. 1. united-atom description of n-alkanes. *J. Phys. Chem. B*, 102(14):2569–2577, 1998.

[266] Valeria Molinero and Emily B Moore. Water modeled as an intermediate element between carbon and silicon. *J. Phys. Chem. B*, 113(13):4008–4016, 2008.

[267] Bin Song and Valeria Molinero. Thermodynamic and structural signatures of water-driven methane-methane attraction in coarse-grained mw water. *J. Chem. Phys.*, 139(5):054511, 2013.

[268] Andrew L Ferguson, Pablo G Debenedetti, and Athanassios Z Panagiotopoulos. Solubility and molecular conformations of n-alkane chains in water. *J. Phys. Chem. B*, 113(18):6405–6414, 2009.